GRAIN REFINEMENT IN CAST TITANIUM 6-ALUMINIUM 4-VANADIUM BY HYDROGENATION, DEFORMATION AND RECRYSTALLISATION

Velile Nicholine Vilane

A dissertation submitted to the Faculty of Engineering and the Built Environment

in fulfillment of the requirements for the degree of

Master of Science in Engineering

January 2013

DECLARATION

1. I know the meaning of plagiarism and declare that all of the work in the dissertation, save for that which is properly acknowledged, is my own.

2. I hereby grant the University of Cape Town free licence to reproduce for the purpose of research either the whole or any portion of the contents in any manner whatsoever of the above dissertation.

Signature:…… Date:……

ACKNOWLEDGEMENTS

I would like to thank the National Research Foundation for financially supporting this project and the following people:

- My supervisor, Prof R. Knutsen for his guidance and support.
- Prof CI Lang for her continued support.
- Prof Trevor Sewell and Miranda Waldron for granting me after-hours access to the UCT Electron Microscope Unit in order to use the Nanosem 230 for EBSD analysis.
- Glenn Newins and the UCT Mechanical Engineering workshop team for machining samples.
- Dianne Steele for her friendship and expertise in referencing
- Nuroo Davids for her friendship and expertise in thesis formatting.
- Family members and friends and for their continued encouragement, patience and prayers.
- Penny Park-Ross for ensuring that the lab environment is safe and stocked with supplies.
- Aunty Elizabeth for keeping the laboratory clean and the kitchen stocked up with coffee.
- Students at the Centre for Materials Engineering for laughter and a conducive working environment.

DEDICATION

To my beloved parents:

Mr Nicholas S. & Mrs Elizabeth Z. Vilane

Thank you for your material, emotional and spiritual support

Most importantly for your unconditional love.

Vilane

Khota,

Mkhulandle,

Wena masisa libalele njengenkhosi!

Wena mbevandvuna!

Wena sitsebe lesihle sekudlela inyama lemanukunuku!

ABSTRACT

Wrought Ti6Al4V has attractive mechanical properties but its usage is limited to high-end aerospace applications because it is costly to machine components from wrought stock. Investment casting is an alternative component manufacturing route but cast components have inferior mechanical properties to their wrought counterparts. Therefore, microstructure refinement is required in order to optimize these mechanical properties. The aim of this work is to refine the as-cast Ti6Al4V microstructure by reducing its prior beta grain sizes and changing its Widmanstätten morphology. Refinement was achieved through combining thermohydrogen processing (THP) and hot deformation.

Ti6Al4V disks of 10mm diameter and 12mm length were alloyed with 20±3 at.% hydrogen. The hydrogenated specimens were deformed and air quenched in the Gleeble 3800. The deformation temperature range was 500°C to 1000°C at strains of 0.2, 0.5, 0.8 and strain rate of $10s^{-1}$. Deformed samples were recrystallized, metastable phase decomposed and dehydrogenated.

Alloying with 20±3 at.% H lowered the beta transus and stabilised more bcc phase at lower temperatures. This enhanced low temperature deformability. The low temperature deformation limit was reduced from 900°C to 550°C. Deforming at 550°C reduced the minimum temperature required to recrystallise grains from 1100°C to 800°C. Deforming and recrystallising at lower temperatures resulted in refined equiaxed bcc grains. The recrystallised and quenched microstructure has needle hcp laths and equiaxed beta grains. Hydrogen stabilised the beta phase at room temperature as a metastable beta phase. Metastable beta decomposed at the metastable phase decomposition step to form needle hcp and presumably hydride phase. However, the latter was poorly indexed by EBSD. Dehydrogenation removed the hydrogen and decomposed hydrides. The nucleation and growth associated with metastable phase and hydride decomposition formed ultrafine grains. The grain sizes were successfully refined from grain diameter ranges of 2mm-3mm (as cast) to 0.1 µm-3µm (refined).

SYMBOLS

at.% H	Atomic percent hydrogen concentration
α_H	Hydrogen saturated alpha phase
α'	Hexagonal martensite
α''	Orthorhombic martensite
β_H	Hydrogen saturated beta phase
δ	Hydride phase
wt.% H	Weight percent hydrogen concentration
X'_α	The volume fraction of hexagonal martensite
X''_α	The volume fraction of orthorhombic martensite
BCC	Body centered cubic
DDW	Dense dislocation walls
ERDA	Elastic recoil detection analysis
Gbα	Grain boundary alpha
GBS	Grain boundary sliding
GNB	Geometrically necessary cell boundaries
GSL	Gleeble script file
HAB	High angle boundaries
HCP	Hexagonal close packed
HPN	Hydrogen phase naklep
IDB	Incidental dislocation boundaries
LB	Lamellar dislocation boundaries
MB	Microbands
M_s	Martensite start temperature
SEM	Scanning electron microscope
TEM	Transmission electron microscope
THP-BD	Thermohydrogen processing – beta decomposition
THP-ED	Thermohydrogen processing – eutectoid decomposition
THP-MD	Thermohydrogen processing – metastable phase decomposition

TABLE OF CONTENTS

LIST OF FIGURES

LIST OF TABLES

1. INTRODUCTION

1.1 Subject of thesis

The subject of the thesis is to investigate the extent of refinement which can be achieved through hydrogen alloying and hot forging. Thermohydrogen processing (THP) has been used to refine the cast Ti6Al4V morphology. This research aims to refine cast Ti6Al4V prior beta grain sizes and the cast Ti6Al4V Widmanstätten morphology.

1.2 Background to thesis

Investment casting is an alternative route to manufacture titanium products instead of powder metallurgy or machining from wrought stock. Casting near net shape components, requires little or no machining. Limiting machining reduces material waste and lowers aircraft manufacturing costs by 60%. [1] **Figure 1.1** shows the typical complex shapes that can be made by investment casting.

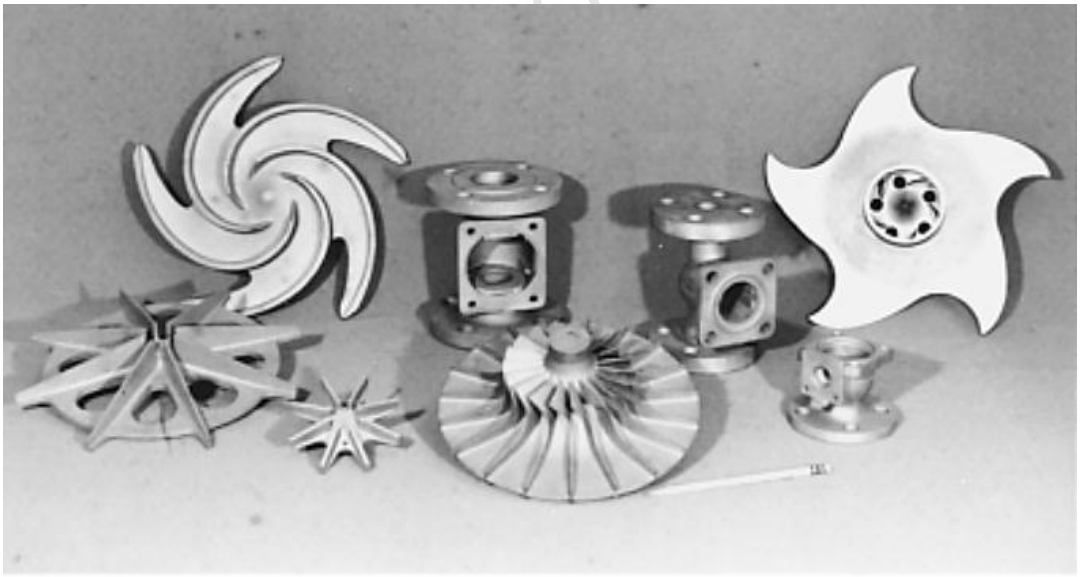

Figure 1.1: *Examples of complex investment cast Ti6Al4V components.* [1]

The disadvantage of casting is its resultant cast microstructure. This has inferior mechanical properties when compared to the wrought microstructure. The cast microstructure needs to be refined in order to optimise its properties.

1.3 Objectives of thesis

i. Use thermohydrogen processing (THP) and forging to refine the grain size and the morphology of the as cast Ti6Al4V microstructure.

ii. Study the microstructure refining mechanisms of THP and forging and understand the evolution of the as cast microstructure to its refined condition.

1.4 Scope of thesis

The material used in this project is investment cast Ti6Al4V, this was hydrogenated and the assessment of the absorbed hydrogen was limited to mass gain measurements. The Gleeble 3800 was used to hot deform samples and the deformation window was limited to:

- Temperature range of 500 °C-1000 °C.
- Strains of 20% (0.2), 50% (0.5) and 80% (0.8).
- Strain rate of $10s^{-1}$.

Microstructure and phase analysis was limited to:

- Optical microscopy (OM).
- Scanning electron microscopy (SEM).
- Electron backscatter diffraction (EBSD).
- X-ray diffraction (XRD).

1.5 Plan of development

Chapter 2 begins with a review of Ti6Al4V metallurgy and the as cast Ti6Al4V microstructure. This is followed by a detailed discussion of the effects of THP and deformation on the microstructure. The experimental design and the testing equipment are described in chapter 3. Results and the discussion are presented in chapter 4. These lead to conclusions in chapter 5 and future work in chapter 6.

2. LITERATURE REVIEW

This chapter begins with a brief introduction to titanium. It then looks at the common Ti6Al4V microstructure morphologies and their mechanical properties. These differences in mechanical properties highlight the importance of microstructure refinement. Thermohydrogen processing (THP) and hot forging are then reviewed. In addition, the major historical discoveries which led to the discovery of THP and hot deformation will be stated. This chapter concludes by stating the hypotheses and research questions that arise from the review of literature.

2.1 Introduction to titanium

Titanium alloys have a high strength to weight ratio and excellent corrosion resistance. **Figure 2.1 a)** shows the densities of selected light and heavy metals. **Figure 2.1 b)** shows the high temperature strength to weight ratios of selected materials.

In **Figures 2.1 a)**, **b)**, titanium alloys are lighter in density and they have a larger strength to weight ratio when compared to steel and superalloys. In comparison, aluminium is lighter than titanium, but its alloys have significantly lower high temperature strength. Titanium`s high temperature oxidation behavior limits its high temperature applications.[2] This is because the diffusion of oxygen into titanium forms a hard and brittle surface layer.[1] This brittle layer is detrimental to the mechanical properties of titanium alloys in service.[1]

Their high strength to weight ratio and good corrosion resistance gives titanium alloys attractive properties that are applied in several industries namely:

- Aerospace.
- Medical.
- Petrochemical.

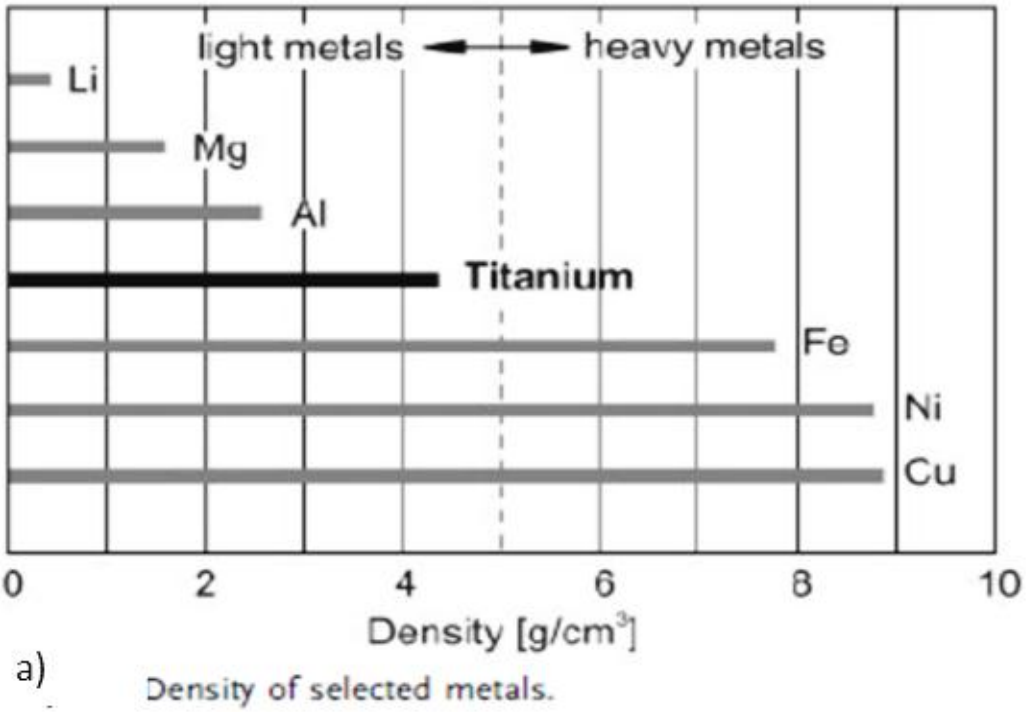

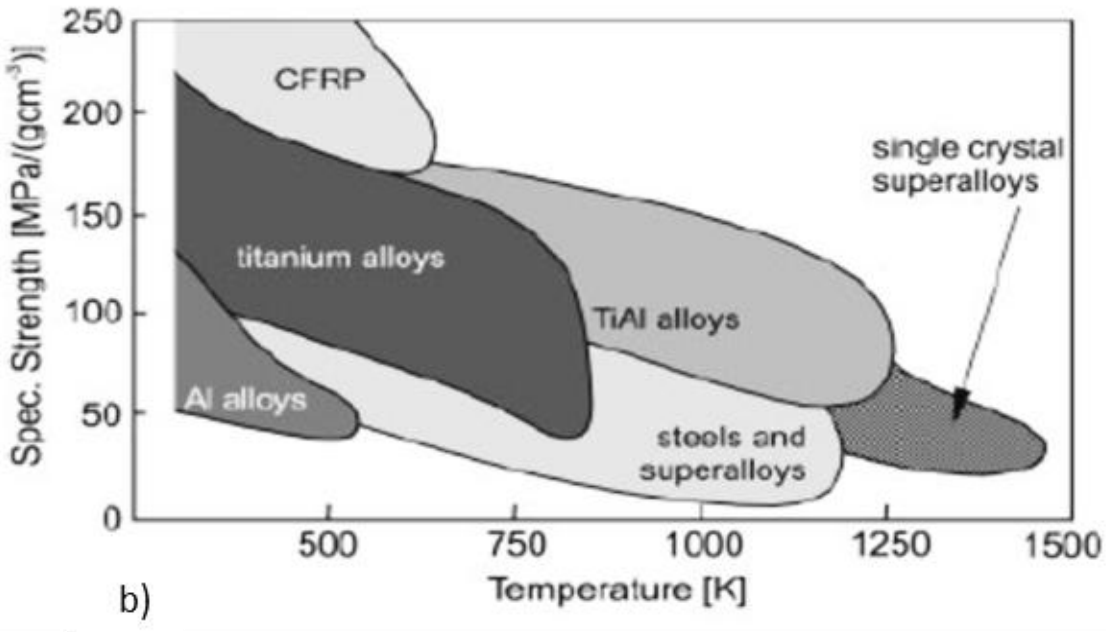

Figure 2.1: *A comparison of the a) density and b) high temperature strength of titanium to other metals.*[2]

2.2 Metallurgy

Ti6Al4V has two allotropes namely α (hcp) and β (bcc) phases which are shown in **Figure 2.2**. Alpha is stable at room temperature, whilst beta is stable above the beta transus. Vanadium is a beta stabiliser and it stabilises some of the beta phase at room temperature. **Figure 2.2** shows the hcp and bcc crystal structures.

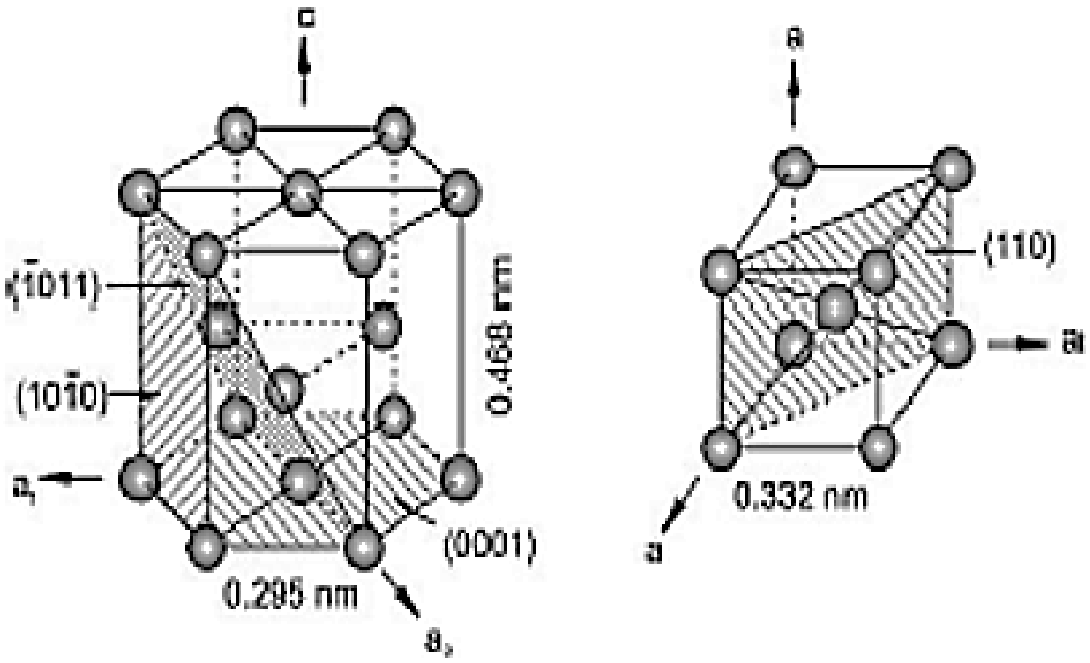

Figure 2.2: *The crystal structures of alpha (hcp) and beta (bcc) phases.*[2]

The crystal structures in **Figure 2.2** are responsible for the varying mechanical properties of alpha and beta phases. The beta phase is softer and more plastically deformable when compared to the alpha phase. This is because the bcc crystal has 12 slip systems that have a high density of atoms. These make them more energetically favorable to plastically deform because dislocations glide easier where there are densely packed atoms. In comparison, the hcp crystal structure has 3 slip systems and is thus less easily deformable.

2.3 The as cast microstructure

The cast Ti6Al4V microstructure has large prior beta grain sizes, thick grain boundary alpha and Widmanstätten morphology. **Figure 2.3** shows the evolution of the as cast Ti6Al4V microstructure during casting.

In **Figures 2.3 a), b)** beta grains nucleate below the Ti6Al4V melting temperature (1668°C).[3] Slow cooling to temperatures below the beta transus temperature nucleates alpha along prior beta grain boundaries, forming grain boundary alpha (Gbα).[3,4] Widmanstätten alpha grows into the prior beta grain along a specific orientation on (110) planes of the beta phase.[5]

Widmanstätten growth continues until it becomes more energy efficient to nucleate more alpha lamellae than grow the existing Widmanstätten lamellae. Therefore, more alpha nucleates at various orientations. These orientation variations are caused by the fact that beta unit cell has 6 close packed planes and 2 close packed directions. This gives 12 possible orientation variations of alpha in the beta grain.[5] Multiple repetitions of these 12 possible alpha orientations forms a basketweave pattern.

Quenching from the beta region causes a diffusionless beta to martensite transformation. Slower cooling rates form thicker alpha lamellae, grain boundary alpha and larger colony sizes. This forms the coarse Widmanstätten microstructure in **Figure 2.3 c)** that has inferior mechanical properties.

Section 2.4 explains how microstructure refinement through thermohydrogen processing (THP) and forging evolved. It further discusses the microstructure refinement methods used in the 20th century and their effects on the microstructure and properties.

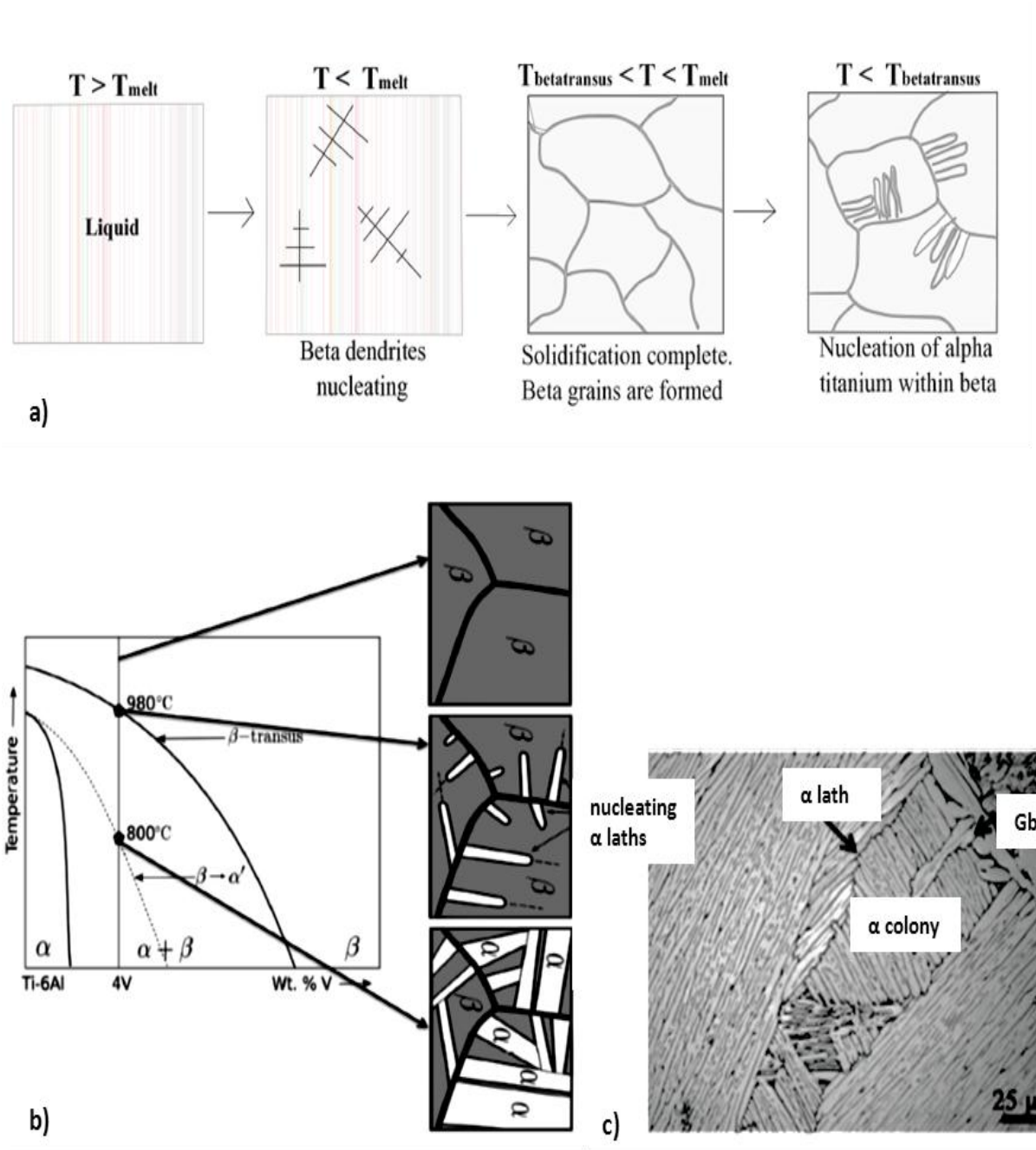

Figure 2.3: *The evolution (a-b) of the as cast Ti6Al4V microstructure shown in (c).*[3]

2.4 Evolution of cast microstructure refinement

Metalworking is the oldest and most mature method of improving material properties and it dates back to B.C. 8000.[6] Early practice of metalworking was limited to simple hammering of metal [6] to desired shapes. After $4000_{B.C.}$[6] it was discovered that hammered metal had improved strength. Interests in metallurgy shifted towards improving material strength and metal alloying was discovered. The discovery of metal alloying led to the bronze age in $1300_{B.C.}$[6] where efficient heating methods were invented. These inventions better equipped metal workers for the discovery and hot working of steel in the later 1200.[6] By the end of the 18th century, the industrial revolution increased the demand for steel products. This lead to the invention of steam powered hydraulic presses.

Material deformability had to be improved in order to reduce material failure during hydraulic pressing. Scientists started researching on ways of increasing material plasticity during pressing (forging). Schleicher and Zwicker[7] were the first scientists to publish on hydrogen induced plasticity of titanium alloys in 1960. They argued that hydrogen lowers the beta transus and stabilises the softer (more deformable) beta phase at lower temperatures.

Scientists generally overlooked this concept because hydrogen was considered a harmful element to materials. This was due to the hydrogen induced industrial catastrophe`s that were prominent at the time. These included laboratory explosions, hydrogen corrosion in petrochemical industries and airplane crashes due to titanium alloy embrittlement. Scientific information in the 1960`s[7] focused on the limitations of hydrogen in materials. Hydrogen embrittlement was studied as a preventative measure to limit titanium alloy component failure in service.

In the early 1970`s[7] scientists started using hydrogen for microstructure refinement and this process was called hydrogen phase naklep (HPN). In HPN, hydrogen was temporary alloyed to a metal to form hydrides. The hydride was decomposed to promote grain refinement and improve material strength. This was particularly done in titanium and aluminium alloys.[7] HPN treatment was also useful in strengthening materials that did not exhibit polymorphism.

2.4.1 Ti6Al4V microstructure refinement in the 20th century

In the 20th century, the Widmanstätten morphology is refined to optimize strength and ductility. Industry designed heat treatment protocols that form fine Widmanstätten, equiaxed and bimodal morphologies as shown in **Figures 2.4-2.5**.

Industry solution treats and furnace cools as cast Ti6Al4V which has coarse microstructures to form fine Widmanstätten microstructures **(Figure 2.4 a)**. Beta stabilisers are used to decrease the beta transus temperature in order to enable solution treating at lower temperatures. This reduces the coarsening caused by the high grain growth rates at high solution treating temperatures. The cooling rates are also controlled, faster cooling rates reduce coarsening time and therefore result in finer Widmanstätten microstructures.

Figure 2.4 b) shows the industrial mill annealing treatment performed on prior deformed specimens to form equiaxed morphology. Mill annealing of deformed microstructures globularises the deformed alpha lamellae forming equiaxed alpha **(Figures 2.5 a, b, e)**. Increased annealing time coarsens the equiaxed morphology as shown in **Figure 2.5 b)**.

Figure 2.4 c) shows the industrial beta solution treating and overaging (BSTOA) protocol which forms the bimodal Ti6Al4V morphology. The bimodal morphology has Widmanstätten and equiaxed alpha colonies **(Figures 2.5 c, d)**. These form after deforming, recrystallizing (plus quenching) and aging in the α+β region. Recrystallisation annealing of the deformed microstructure nucleates equiaxed alpha and beta grains.[8] Subsequent quenching after recrystallization forms martensite, this decomposes to alpha and beta when aged at 600°C. Air cooling from aging temperature (600°C) causes a Widmanstätten beta to alpha transformation. As a result equiaxed and Widmanstätten alpha morphologies coexist in the microstructure forming the bimodal morphology. Refining the Widmanstätten morphology to equiaxed or bimodal morphologies has been shown to improve shear, tensile and fracture properties. [8,9] The effect of refining the Widmanstätten morphology on tensile strength, ductility and crack propagation is explained in **Section 2.4.2**.

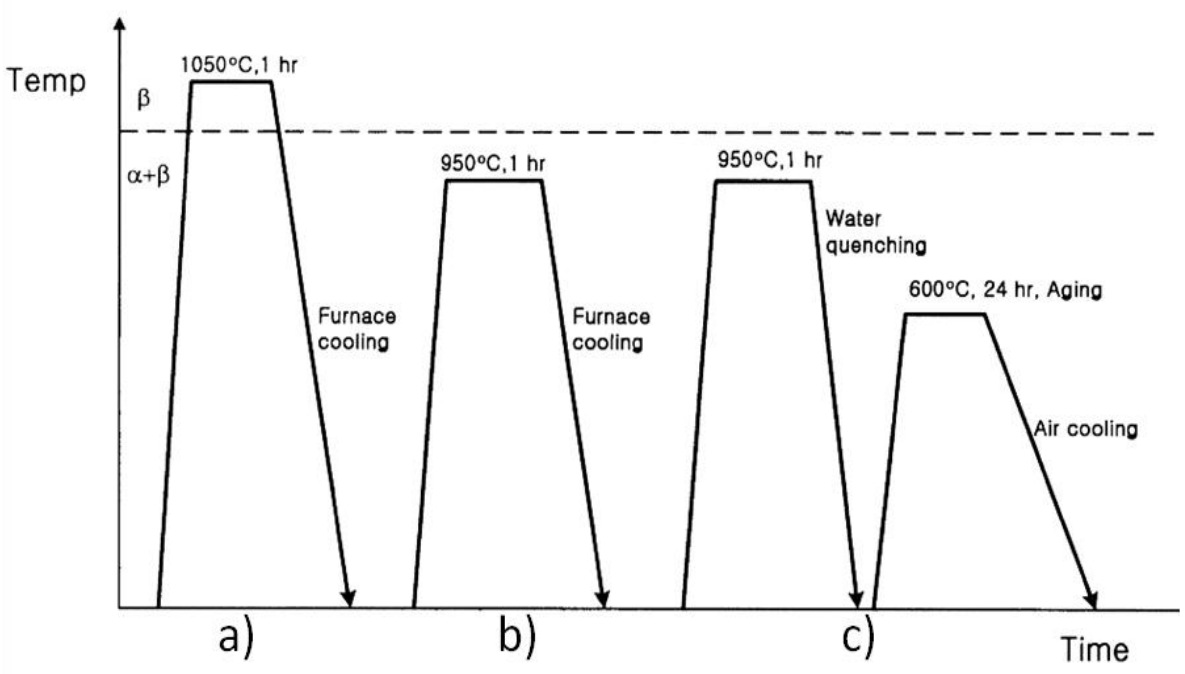

Figure 2.4: *Shows a schematic of a) solution b) mill anneal and c) BSTOA heat treatments*[8]

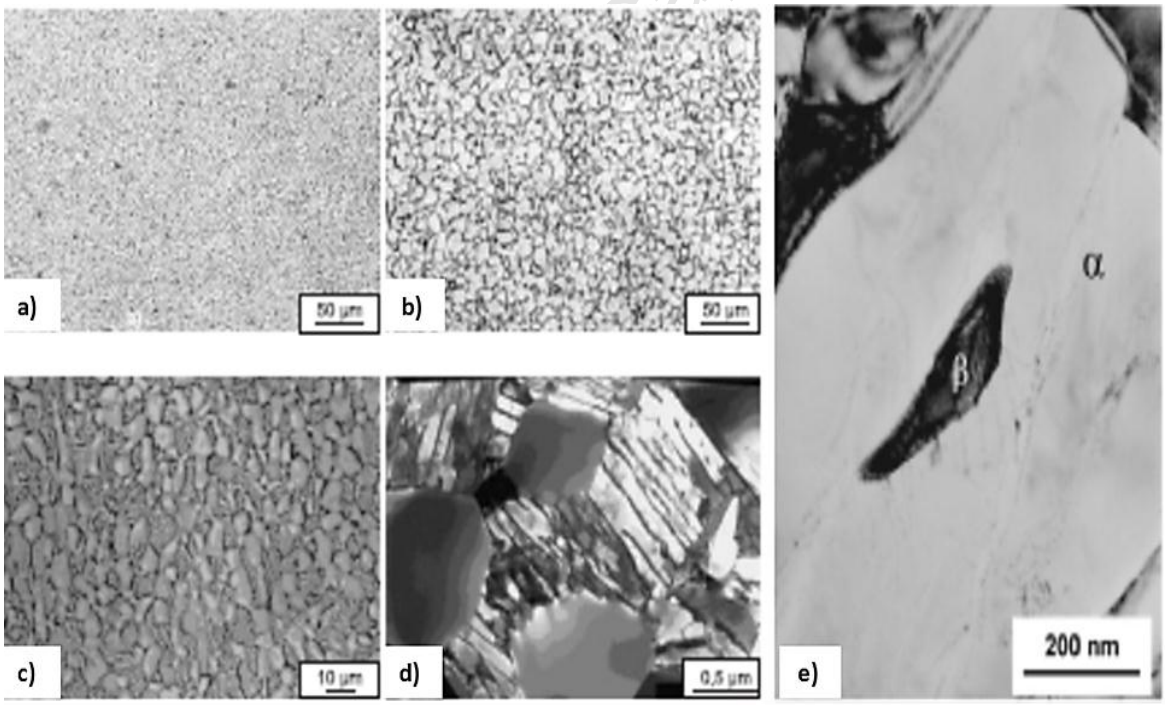

Figure 2.5: *Shows micrographs of equiaxed (a, b, e) and bimodal microstructures(c, d).* [2, 5, 8, 10]

2.4.2 Effect of refinement on tensile properties

Table 1.1 shows that the bimodal and equiaxed microstructures have better tensile properties when compared to the Widmanstätten microstructure. In **Table 1.1**, the Widmanstätten microstructure has the least strength and ductility properties. In comparison, the bimodal microstructure has optimum strength but poor ductility and the equiaxed microstructure has the best combination of strength and ductility.

Table 1.1: *Tensile results of the Widmanstätten, equiaxed and bimodal microstructures* [8]

Microstructure	YS (MPa)	UTS (MPa)	Elongation (Pct.)
Widmanstätten	829	897	12.7
Equiaxed	872	959	15.1
Bimodal	1070	1134	10.7

Pct. - percent

Benedetti[9] also showed that the Widmanstätten microstructure had poor fracture toughness when compared to the bimodal microstructure. Crack propagation was much faster in Widmanstätten microstructures when compared to bimodal microstructures. This was because Widmanstätten (lamellar) microstructures provide longer crack path lengths when compared fine equiaxed microstructures.

This work aims to refine the cast Ti6Al4V prior beta grain sizes and the Widmanstätten morphology. This will be done by using thermohydrogen processing (THP) and forging. **Sections 2.5** and **2.6** look at the individual effects of THP and forging on the microstructure and its refinement.

2.5 Forging and microstructure refinement

Three main deformation variables affect the deformed microstructure. These are namely deformation temperature, strain and strain rate. **Section 2.5.1** reviews the effects of processing temperature (excluding deformation) on the phase constituents of the microstructure. The combined effects of deformation and temperature on the microstructure are discussed in **Section 2.5.2**.

2.5.1 Effect of forging temperature on the phase composition

The processing temperature determines the amount of primary alpha, secondary alpha and martensite that forms in the microstructure.

2.5.1.1 Primary and secondary alpha

A microstructure that has primary and secondary alpha forms at temperatures between 850°C to 950°C. In **Figures 2.6 a)-c)** the amount of retained alpha (primary alpha) decreases with increasing annealing temperature. At high annealing temperatures, some of the primary alpha transforms to beta. If slow cooled, the beta transforms to secondary alpha (newly formed alpha phase).

2.5.1.2 Primary alpha and acicular martensite

Primary alpha and acicular martensite forms when quenching at temperatures close to the beta transus (1000°C). At this temperature, some of the primary alpha has transformed to beta. During quenching, the beta transforms to martensite. As a result, the final microstructure consists of acicular martensite and primary alpha **(Figure 2.6 d)**.

2.5.1.3 Fully martensitic microstructure

Quenching from temperatures above the beta transus, (1050°C) forms a fully martensitic microstructure **(Figure 2.6 e)**. Significant microstructure variations occur when the Widmanstätten microstructure **(Figure 2.6 f)** is deformed in the α+β or β regions. The effect of deformation strain on the microstructure is discussed in **Sections 2.52-2.53**.

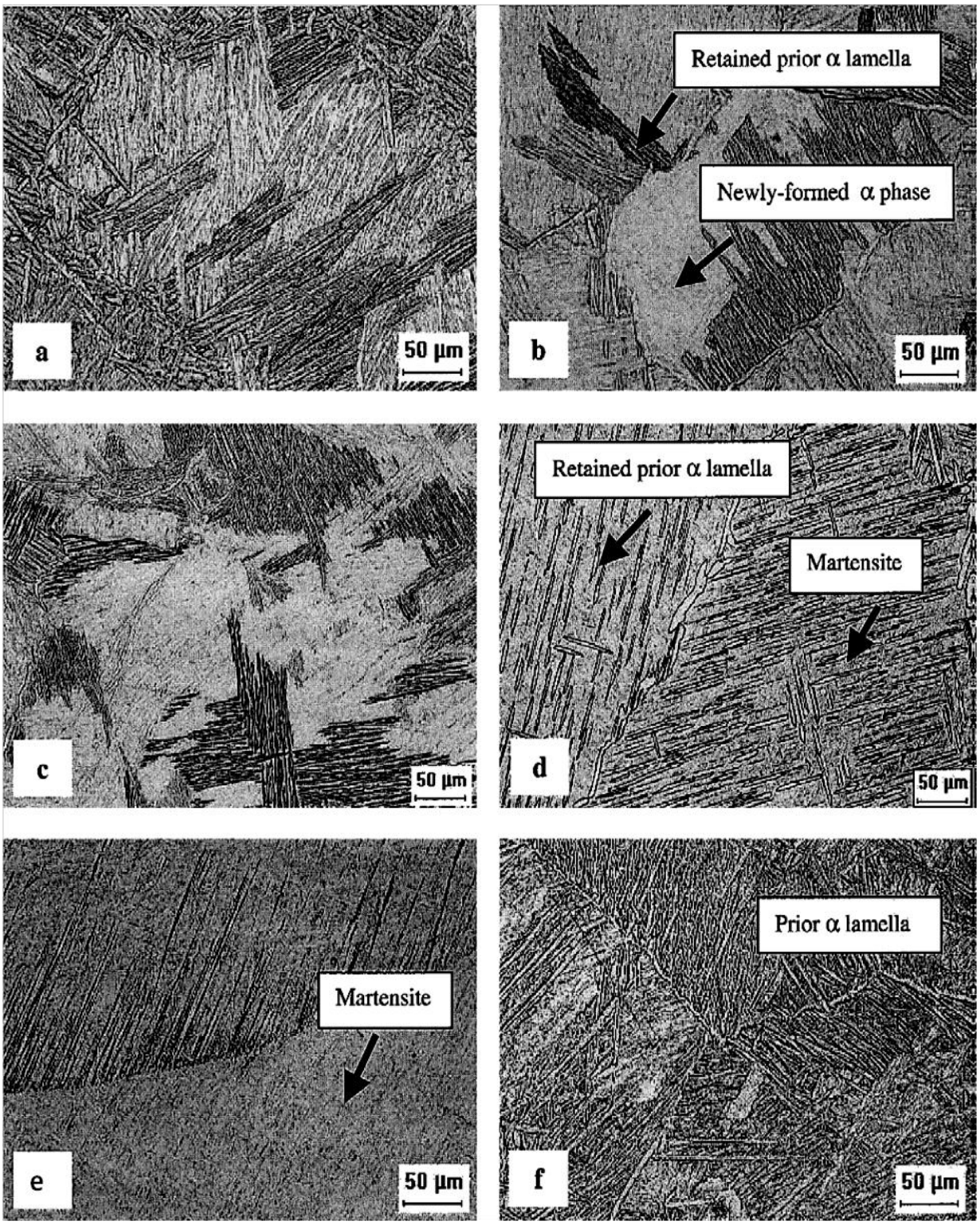

Figure 2.6: *Effect of processing temperature and cooling rate on f) as cast Ti6Al4V. Microstructures a)-c) were heated to a) 850°C, b) 900°C, c) 950°C and furnace cooled. Microstructures d)-e) were heated to d) 1000°C, e) 1050°C and quenched.* [11]

2.5.2 Effect of forging strain and subsequent diffusion on the morphology

In **Figures 2.7 a)-c)**, forging in the α+β region distorts and eventually 'breaks up' alpha forming discontinuous alpha. Diffusion spherodises the discontinuous alpha to form globular (diffused) alpha.

2.5.2.1 Discontinuous (break up) alpha

Distorted and discontinuous alpha (break up alpha) lamellae form after deforming in the α+β region. Distorted and discontinuous (break up) alpha **(Figures 2.7 a, c)** forms through two mechanims namely:[11]

- The formation of high angle boundaries (HAB`s) across alpha plates.
- Shearing of alpha lamellae during deformation.

The first mechanism proposes that deformation forms high angle boundaries (HAB) across alpha plates. These can have misorientation angles up to 30 degrees.[11] The high angle boundaries break up the alpha plate into smaller grains. The beta phase then penetrates into the alpha plate along these new high angle boundaries. This causes the alpha plate to partially or fully separate depending on its lamellar width and the beta penetration distance.

The second mechanism proposes that during hot forging, alpha lamellae break up due to localised shear and rotation. The misorientation across this shear band can be up to 20 degrees.[11] The beta phase then penetrates into the sheared alpha platelets along the shear bands separating them to segments. The penetration rate on both mechanisms depends on the rate of diffusion of alloying elements Al, V, along the interfaces.

2.5.2.2 Globular (diffused) alpha

In **Figure 2.7 b)**, diffusion globularises the discontinuous lamellae in **Figure 2.7 a)** to form a globular or diffused alpha phase. Lamellae globularisation is driven by the quest to minimize surface area and attain thermodynamic stability.[12, 13] Globularisation of alpha lamellae is dominant at processing temperatures where diffusion is most prominent. [12, 13]

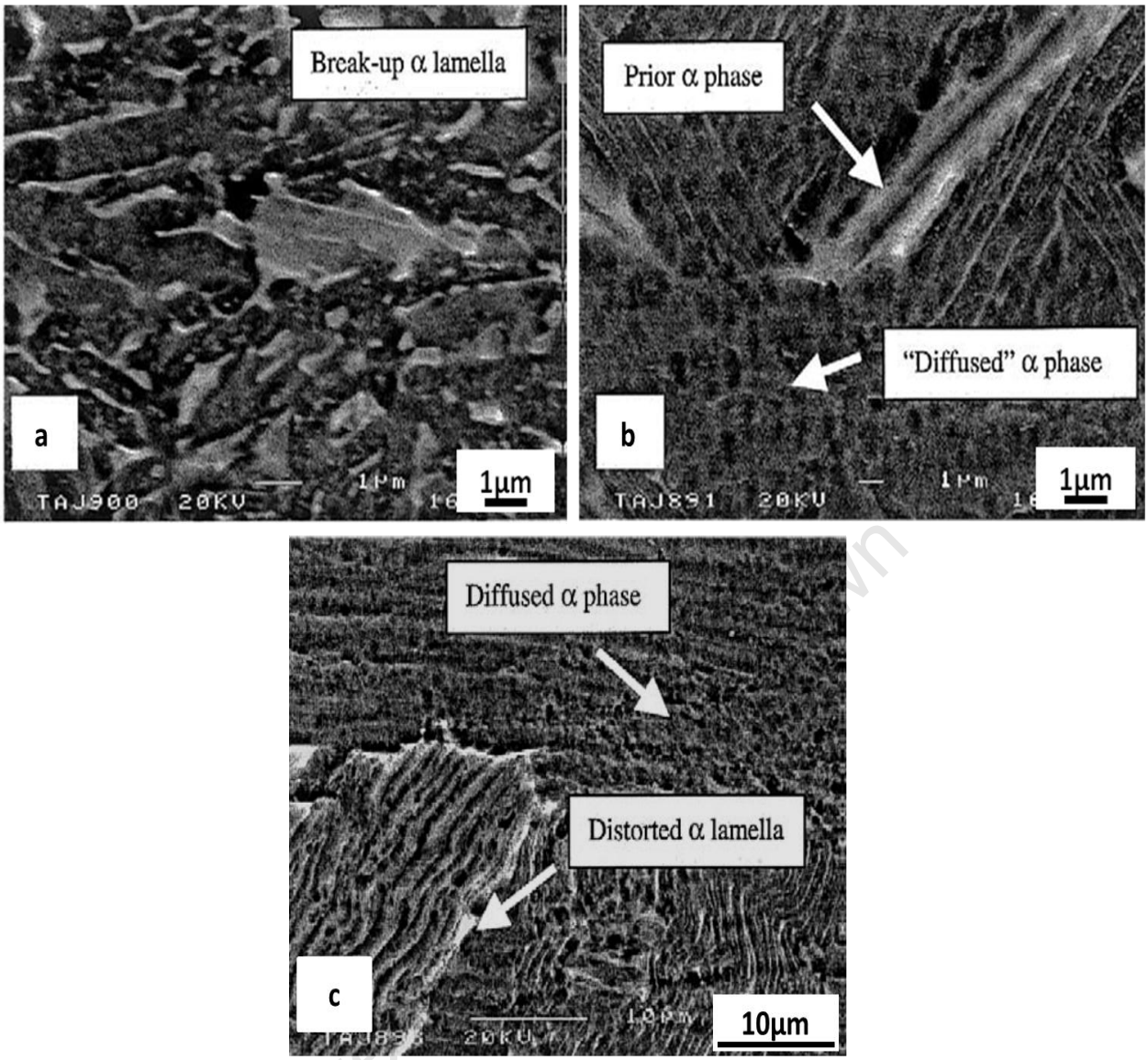

Figure 2.7: *Shows a) discontinuous, b) globular alpha and a low magnification view of c) distorted and diffused alpha.* [11]

2.5.3 Recrystallisation and stored deformation energy

The recrystallised grain size depends on the recrystallisation temperature. The minimum temperature required to recrystallize grains (minimum recrystallisation temperature) depends on the amount of stored energy in the material. Energy is stored in materials in the form of vacancies, grain boundaries and surface energies. During forging, deformation energy is stored in the material in the form of dislocations. Releasing the stored energy acts as a driving force for recovery, recrystallisation and grain growth.

Stored energy can be increased by deforming at lower temperatures, high strain and high strain rates. Increasing the deformation strain or strain rate has been reported to decrease the recrystallised grain size. [11] In **Figures 2.8 a), b)**, the recrystallised prior beta grain size decreased with increasing strain rate from a) 0.5 s^{-1} to b) 1 s^{-1}.

The grain orientation subdivisions that occur on deformed microstructures are discussed in Doherty et al. [14] At low deformation strain **(Figures 2.9 a, b)**, the microstructure has low angle boundary cell blocks referred to as incidental dislocation boundaries (IDB).[14] These can be single walled dense dislocation walls (DDW) or double walled micro bands (MB).[14]

At high deformation strain **(Figures 2.9 c, d)**, the microstructure has high angle boundary regions that are surrounded by geometrically necessary cell boundaries (GNB).[14] These high angle boundary regions are misoriented at more than 15-20 degrees.[11] They are elongated in the deformation direction and are surrounded by lamellar dislocation boundaries (LB).[14]

It is evident that to increase stored deformation energy and decrease the recrystallised grain size, deformation must be performed at high strain, strain rates and low temperatures. However, deforming at these optimum deformation parameters is not always ideal because it can lead to formation of microstructure defects as explained in **Section 2.5.4**.

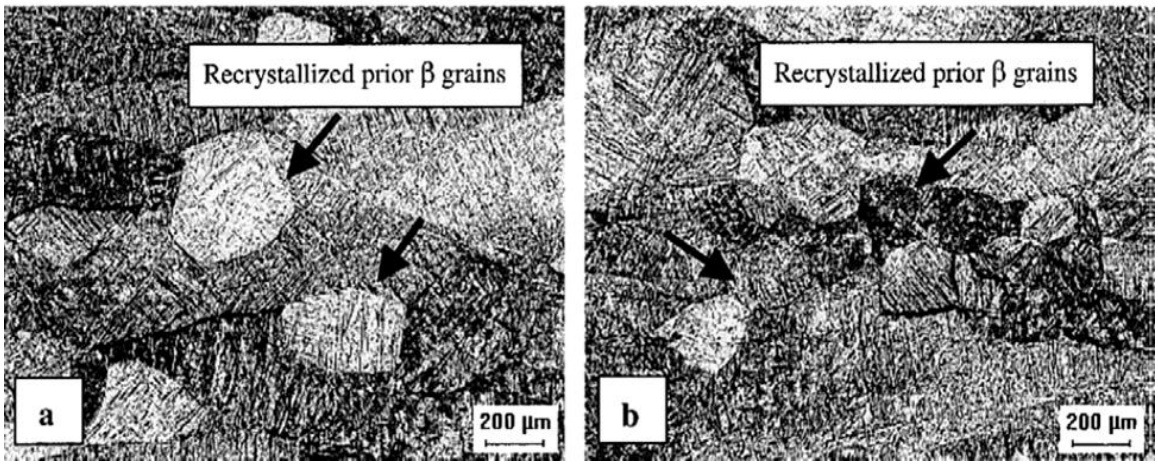

Figure 2.8: *The effect of strain rate on grain size. The strain rate was a) 0.5 s^{-1} and b) 1 s^{-1}.* [11]

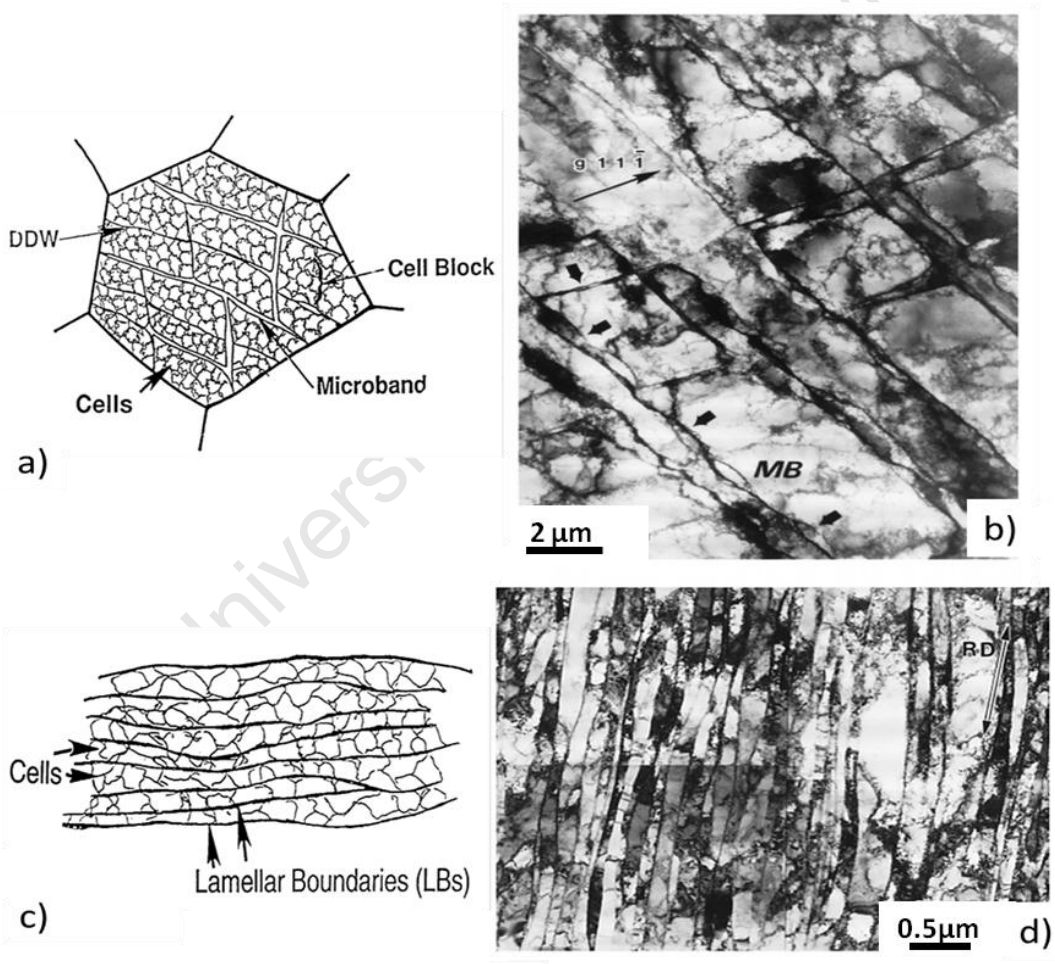

Figure 2.9: *Schematic and TEM micrographs of grain subdivision at a)-b) small and c) d) large strain.*[14]

2.5.4 Microstructure defects caused by forging above deformation limits

Deforming the lamellar microstructure **(Figure 2.10 a)** outside the allowable deformation limits causes microstructure defects. The microstructure defects and the allowable deformation limits are shown in **Figures 2.10-2.11** respectively. To avoid microstructure defects deformation can either be done at high temperatures (at strains below $1s^{-1}$) or in the globularisation region **(Figure 2.11)** to form the globular microstructure in **Figure 2.10 b)**.

2.5.4.1 Prior beta boundary cracks

Prior beta boundary cracks **(Figure 2.10 c)** [12, 15] normally occur at deformation temperatures below 900°C. They nucleate at thin beta layers between grain boundary alpha, colony alpha and beta. They are caused by grain boundary sliding and the incompatible deformation behaviors of alpha and beta phases.[12] Grain boundary sliding causes lattice mismatches and stress concentrations [12, 13, 15, 16] at triple junctions of the thin beta layer. If this stress is not relieved, voids nucleate, grow and coalesce into propagating cracks. [13] Prior beta boundary cracks are not visible on the surface of a hot worked billet.

2.5.4.2 Adiabatic shear bands

Shear bands **(Figure 2.10 d)** nucleate [12, 15] at thin β layers between alpha and beta. At high strain rates, the low thermal conductivity of titanium limits adiabatic heat dissipation. This causes adjacent regions to have varying deformation compatibilities [12, 13, 16] or localized flow **(Figure 2.10 e)**. The localized flow regions have material instability which forms adiabatic shear bands. Shear bands are the favored macro crack nucleation sites [12, 15] and they normally occur at deformation temperatures below 900°C. Deforming above 1000°C can result in recrystallisation of new prior beta grains **(Figure 2.10 g)**. However, this can also form beta instabilities if deformation is performed at strain rates greater than $1s^{-1}$ **(Figure 2.10 h)**.

2.5.4.3 Lamellar kinking

At strain rates greater than 10^{-2} s^{-1}, lamellar kinking is more prominent than globularisation. [17] The varying deformation compatibilities of the alpha and beta phases cause shearing of lamellae, this forms kinked lamellae **(Figure 2.10 f)**.

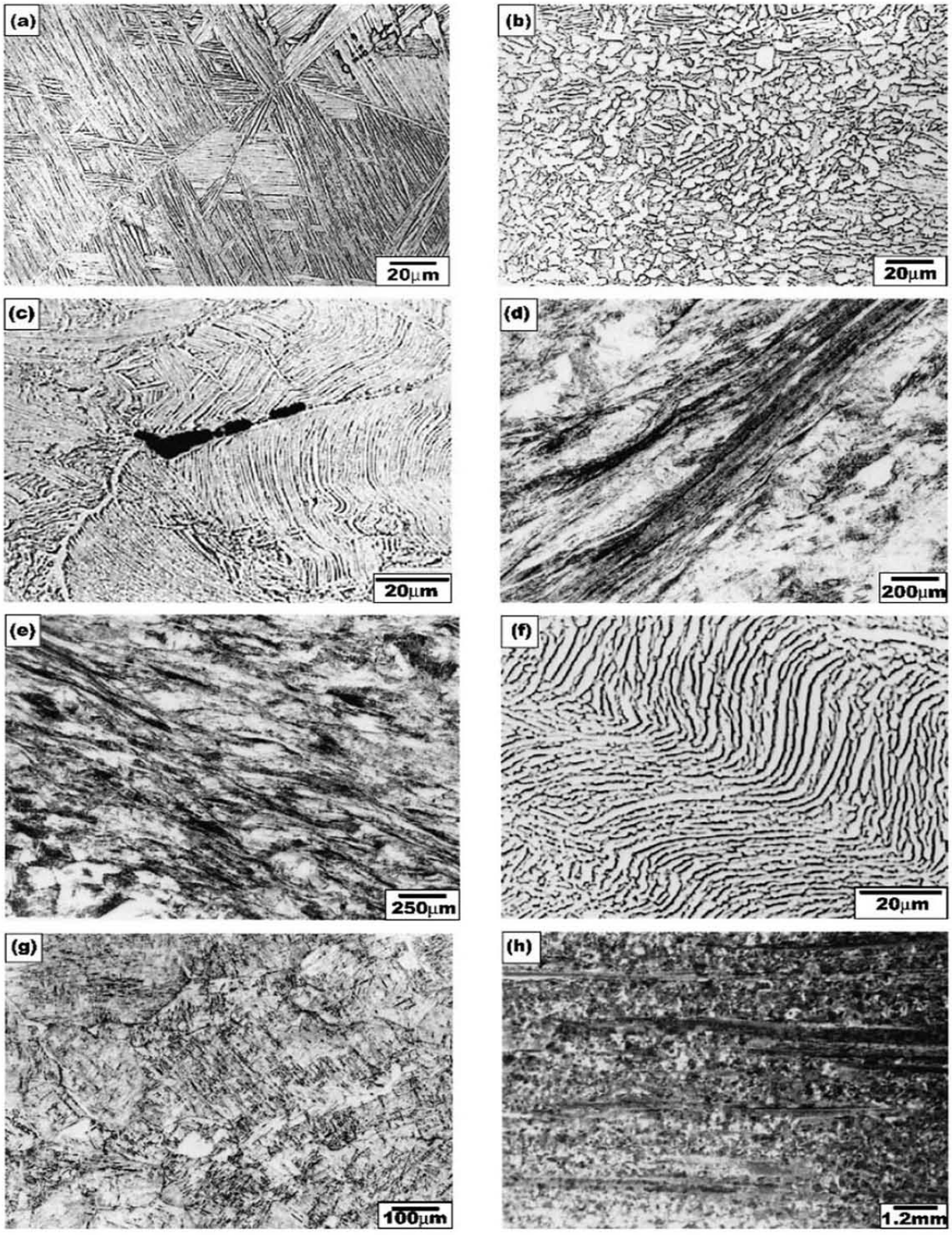

Figure 2.10: *Ti6Al4V micrographs showing a) lamellar microstructure, b) globularisation, c) prior β boundary cracking d) adiabatic shear banding e) flow localization, f) lamellae-kinking, g) DRX and h) beta instability.*[12]

2.5.5 A processing map approach to avert forged microstructure defects

A processing map approach to optimizing hot forging has been established as a useful tool. [12, 17, 18] Several authors [19-23] have characterized deformation and hot working behavior of Ti6Al4V using empirically based computational models. From these models a series of processing maps showing stable and unstable deformation regions were produced. Front [24] and Raj [25] proposed processing maps which show microstructure defects as function of temperature and strain rate. **Figure 2.11** shows that to avoid microstructure defects, deformation must be done in the globularisation or dynamic recrystallization regions.

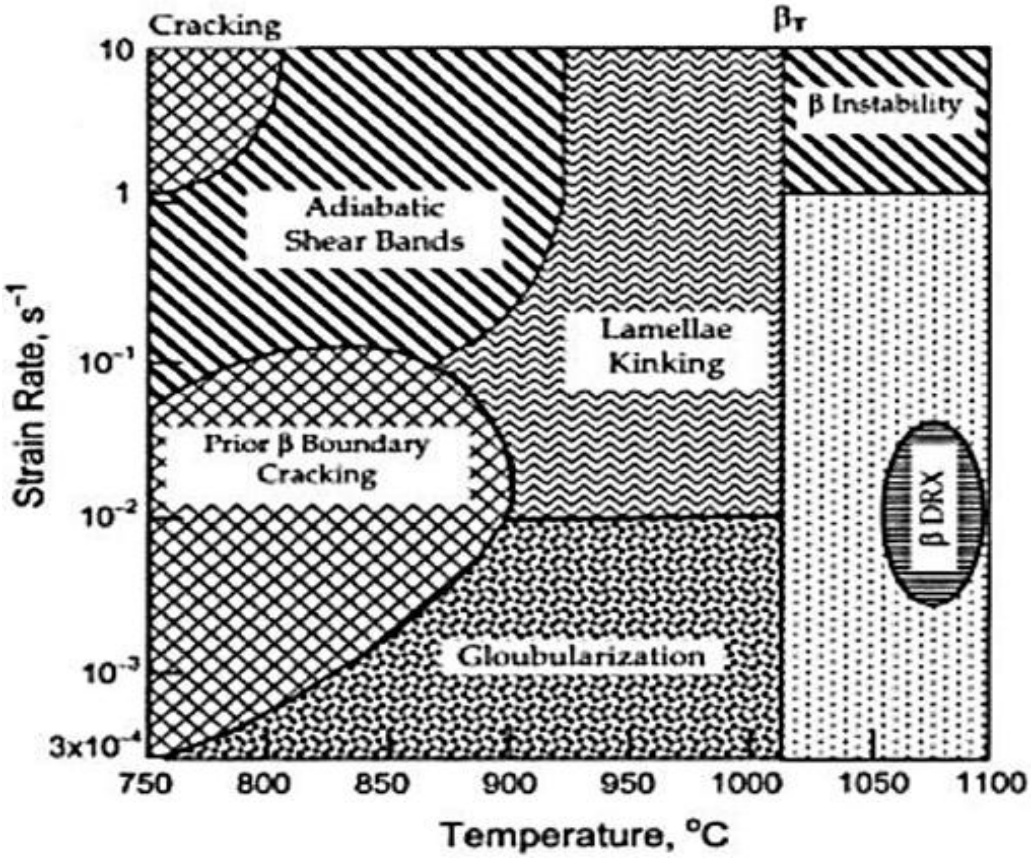

Figure 2.11: *Processing map for Ti6Al4V with a lamellar starting microstructure.* [12]

In **Figure 2.11**, deforming at temperatures below 900°C or strain rates greater than 10^{-2} s^{-1} is likely to cause microstructure defects. Alloying Ti6Al4V with hydrogen can improve this deformation limit by stabilising the softer, deformable beta phase at lower temperatures. This is explained under thermohydrogen processing in **Section 2.6**.

2.6 Thermohydrogen processing (THP)

THP is a technique where hydrogen is used as a temporary alloying element in titanium alloys to enhance deformability and modify the microstructure morphology. [26-28]

2.6.1 Absorption of hydrogen by Ti6Al4V

Absorbed hydrogen occupies tetrahedral [29] sites in Ti6Al4V. The beta phase has a bcc lattice which has 12 tetrahedral and 6 octahedral sites. In comparison, [29] the alpha phase has an hcp lattice which has 4 tetrahedral and 2 octahedral sites. Therefore, the beta phase dissolves more hydrogen than the alpha phase.

In 1953, Wasilewski [27, 30] proposed that the extent of hydrogen absorption depends on the hydrogenation temperature and hydrogen concentration. This means that if Ti6Al4V is heated in a hydrogen atmosphere, hydrogen diffuses into the alloy, until it reaches a saturation point. This saturation point varies with hydrogenation time, temperature and hydrogen pressure. Wasilewski [27, 30] further stated that hydrogen absorption increases at 500°C and that the presence of an oxide layer impedes absorption at high temperatures.

In 2003, elastic recoil detection analysis (ERDA) measurements on hydrogenated Ti6Al4V confirmed the relationship between hydrogenation temperature and hydrogen diffusion. López et al. [31] showed that hydrogen is not absorbed until a threshold hydrogenation temperature of 500°C is reached.

Figure 2.12 [32] shows atomic percent hydrogen absorption when compared to hydrogenation time, temperature and hydrogen gas concentration. In **Figure 2.12**, a greater amount of hydrogen was absorbed at a hydrogenation temperature of 650°C than at 850°C. Matthews[32] argued that an oxide layer decreases hydrogen absorption at higher hydrogenation temperatures. The amount of absorbed hydrogen increased when the hydrogen gas concentration increased from 5 vol.% H to 15 vol.% H. Peak hydrogen absorption was reached after 3 hours in 15 vol.% H. The effect of hydrogen absorption on the phase composition of Ti6Al4V is discussed in **Section 2.6.2**.

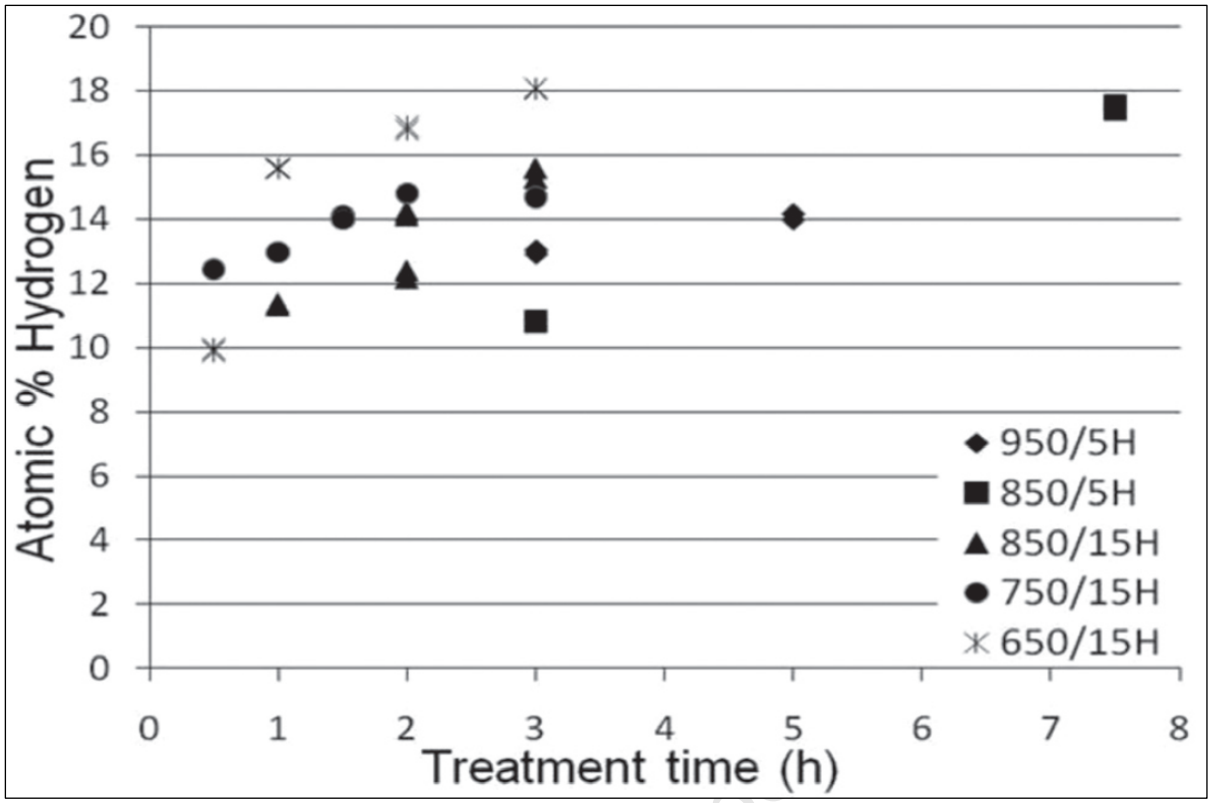

Figure 2.12: *The effect of THP parameters on hydrogen absorption.* [32]

2.6.2 Phase boundaries in the Ti6Al4VxH system

William Kerr [33] was one of the earliest reported authors to have worked on the phase composition of the Ti6Al4VxH system in the 1980`s. Years later, results from Ilyin et al. [34] and Qazi et al. [35] show similar phases to Kerr. All the authors [33-35] agree that alloying Ti6Al4V with 30 at.% H reduces the beta transus from about 1050°C to about 800°C. However, these authors have contradicting views on the location of the phase boundaries.

In 1985, Kerr`s XRD analysis [33] showed that hydrides form at hydrogen concentrations greater than 15 at.% H. In addition, Kerr [33] showed that the hydrides are stable at temperatures of up to 800°C **(Figure 2.13 a)**. [33] In 1993, Ilyin et al. [34] contradicted Kerr`s findings by arguing that hydrides can only form at temperatures below 250°C **(Figure 2.13 b)**. In 2001, Qazi et al.`s [35] TEM analysis supported Kerr`s [33] findings by showing that hydrides are stable at temperatures of up to 900°C. In addition to Kerr`s [33] original findings, Qazi et al.`s [35] work shows that a beta and hydride region exists above 15 at.% H between 800°C and 900°C **(Figure 2.13 c)**.

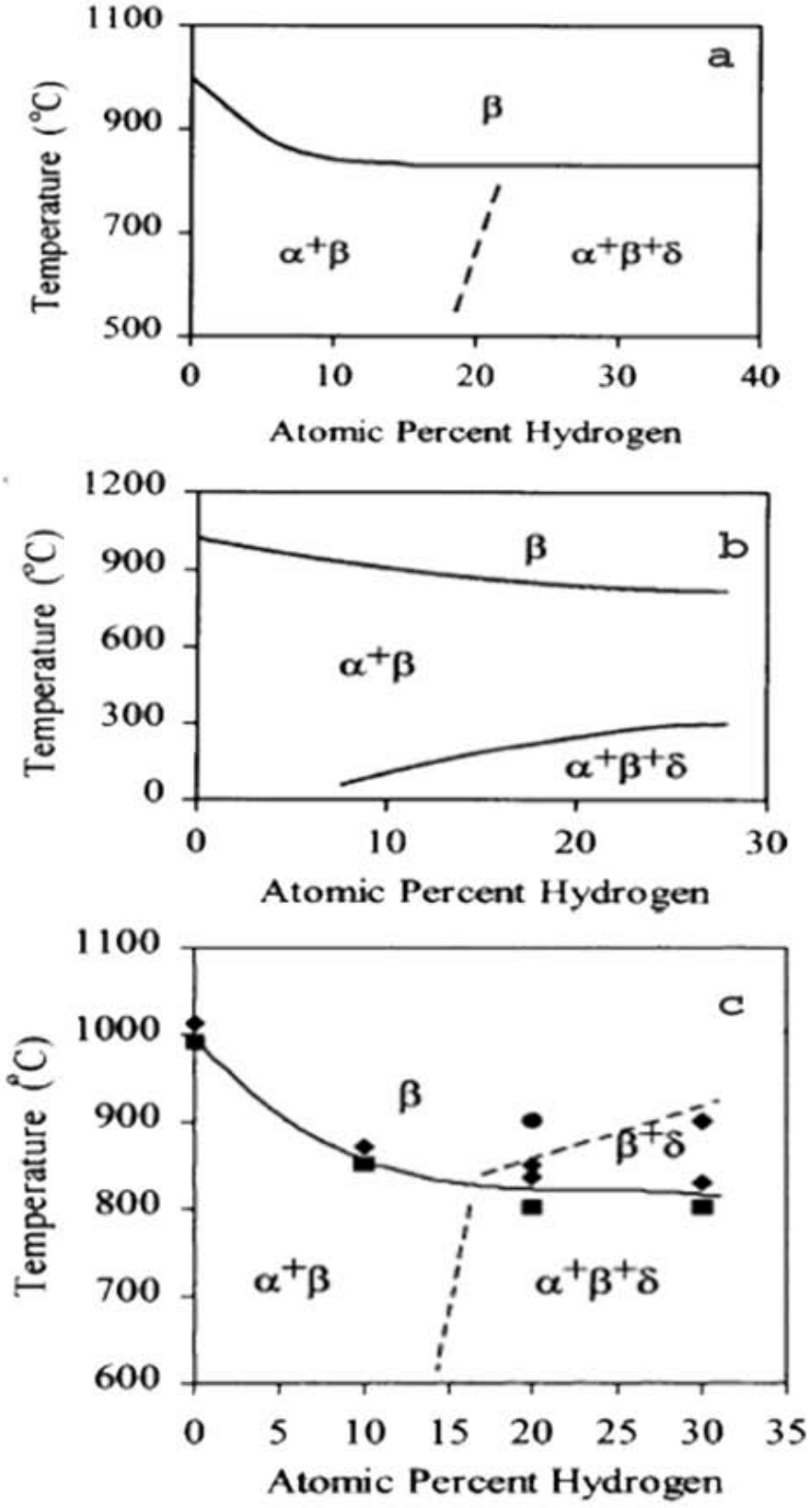

Figure 2.13: *Ti6Al4VxH phase boundaries according to a) Kerr, b) Ilyin and c) Qazi.* [33-35]

2.6.3 Commonly used THP processing routes

Thermohydrogen proscessing (THP) consists of heat treatments that enhance microstructure refinement by decomposing hydrogen induced phases. The most common THP treatments promote metastable phase, eutectoid and hydride decomposition.

Figures 2.14 a), b) show two commonly used microstructure refining THP methods. These are namely eutectoid decomposition (THP-ED) and martensite decomposition (THP-MD). The THP treatments start with a solution treatment step in the single phase beta region. In THP-ED, samples are isothermally annealed at the eutectoid temperature after slow cooling from solution temperature. In THP-MD samples are quenched (from solution temperature to room temperature), reheated to aging temperature and aged. Both THP methods have a dehydrogenation step which is performed to remove hydrogen and decompose hydrides. The microstructure refining mechanisms of THP treatments are discussed in **Sections 2.6.4-2.6.5**.

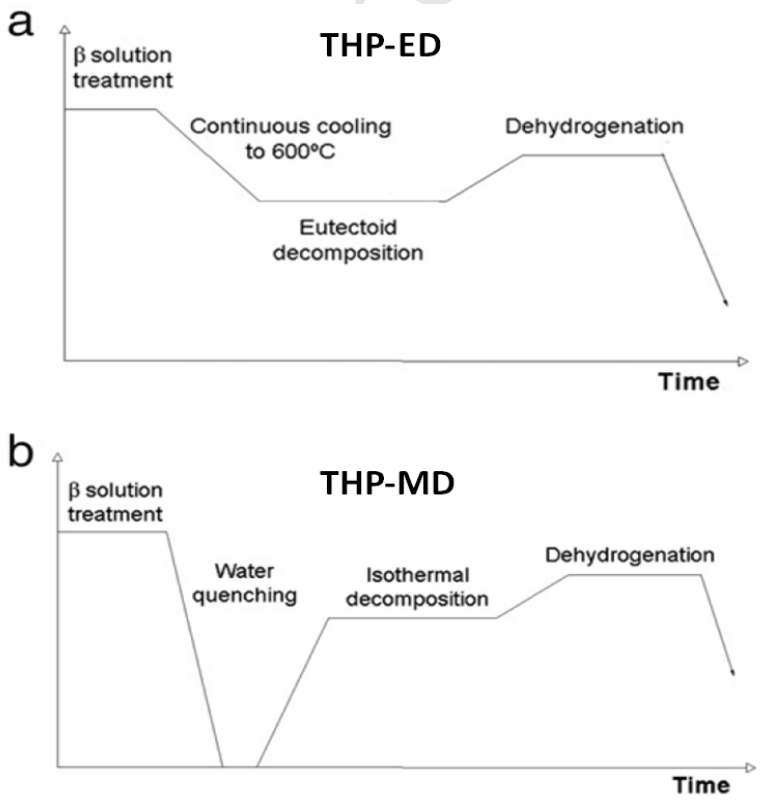

Figure 2.14: *THP treatments for a) eutectoid and b) martensite decomposition.* [10, 36, 37]

2.6.4 THP mechanisms of refinement

Microstructure refinement [10, 36-38] is caused by lower solution treatment temperatures and a series of hydrogen induced phase transformations. These hydrogen induced phase transformations are summarized in **Table 2.1**.

2.6.4.1 Eutectoid decomposition

Hydrogen occupies interstitial sites of the alpha and beta phases forming saturated alpha (α_H) and beta (β_H) phases. It then stabilises the beta transus at lower temperatures and this reduces the temperature required to solution treat THP specimens.

At the solution temperature, saturated alpha has fully transformed to saturated beta **(Figure 2.15 a)**. Furnace cooling from the solution temperature to temperatures below the beta transus temperature causes a beta to alpha transformation **(Equation 2.1)**. Alpha precipitates on prior beta grain boundaries as grain boundary alpha **(Figures 2.15 b, c)**.

$$\beta_H \rightarrow \alpha_H \quad [39\text{-}41] \qquad (2.1)$$

At the eutectoid temperature (600°C), [10] residual saturated beta (β_H) transforms to saturated alpha (α_H) and hydride (δ) **(see Equation 2.2)**. Beta does not fully decompose to alpha and hydride, because vanadium and hydrogen stabilise the beta phase at room temperature.

$$\beta_H \rightarrow \alpha_H + \delta + \beta_H \quad [39\text{-}41] \qquad (2.2)$$

Below the eutectoid temperature, saturated beta further transforms to saturated alpha. Shan et al. [40] stated that alpha absorbs 8 at.% H whilst beta can absorb up to 40 at.% H. Therefore, as more beta transforms to alpha, hydrogen distorts the alpha lattice.

To eliminate lattice distortion, saturated alpha phase separates into hydrogen rich and hydrogen lean regions **(Figures 2.15 d, e)**. The hydrogen rich regions form hydrides whilst the hydrogen lean regions form eutectoid alpha **(Equation 2.3)**. The driving force for hydride precipitation is to eliminate the lattice distortion caused by solid solution of hydrogen in the alpha phase.

$$\alpha_H \rightarrow \alpha_H + \delta \text{ [39-41]} \quad (2.3)$$

Hydride precipitation causes a volume misfit. [40] This causes strain between the hydride and the surrounding matrix which is accommodated elastically or plastically by:

- Plastic deformation of the adjacent matrix.
- Twinning of the hydride.
- Strain induced beta to martensite transformation.

The martensite transformation **(Equation 2.4)** is also enhanced by the fact that hydrogen lowers the critical cooling rates for martensite formation **(Figure 2.15 f)**. The martensite transformation can either form hexagonal (α') or orthorhombic (α'') martensite depending on the amount of alloyed hydrogen.

$$\beta_H \rightarrow \text{Martensite } (\alpha' / \alpha'') \text{ [39-41]} \quad (2.4)$$

The eutectoid decomposition forms hydrides which decompose during dehydrogenation to form an ultrafine microstructure. The formation and decomposition of hydrides is reported as the main cause of microstructure refinement in THP. [38, 39, 42] The microstructure refining phase transformations that occur during dehydrogenation are shown by **Equations 2.5-2.7** in **Section 2.6.4.2**.

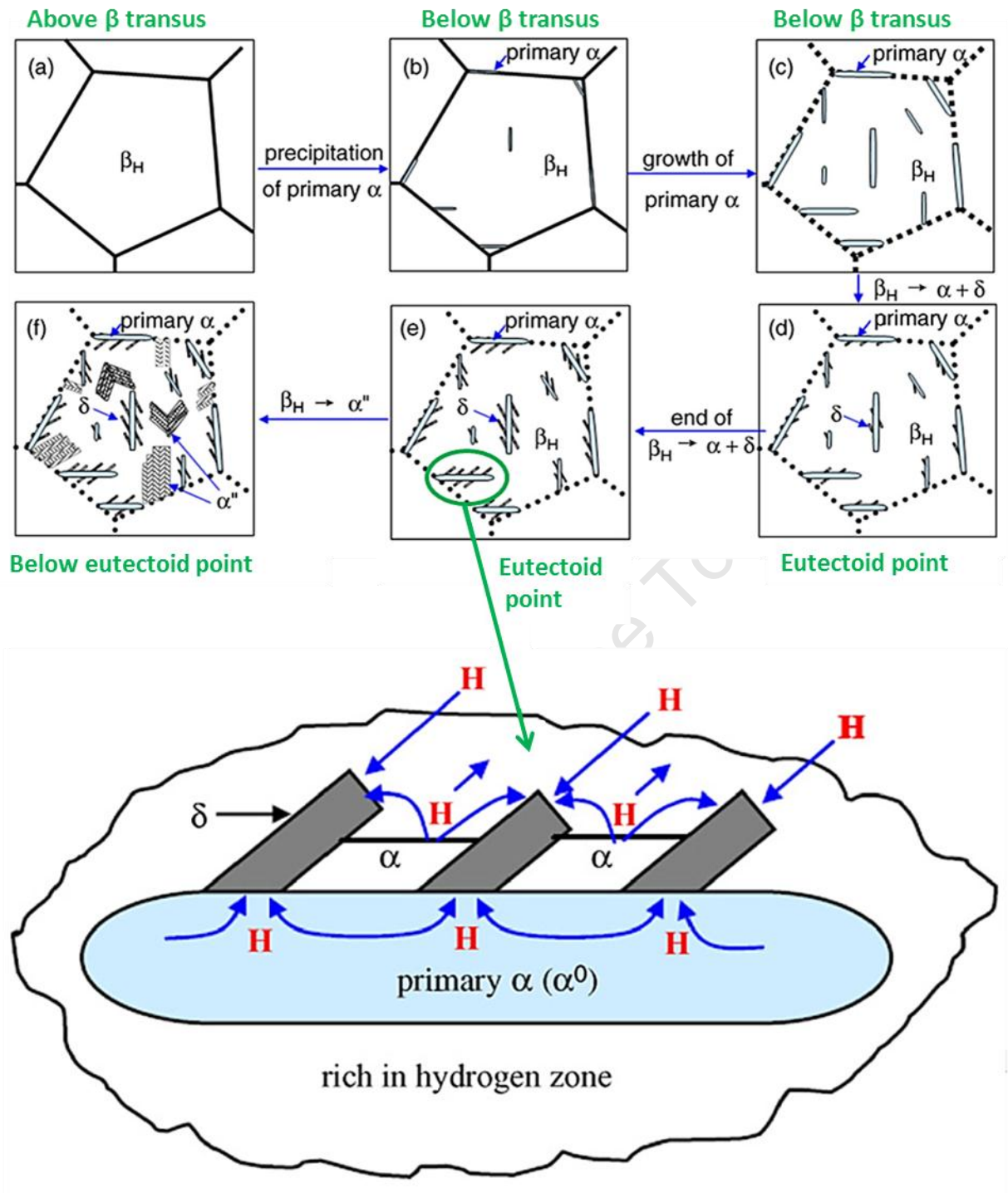

Figure 2.15: *Microstructure evolution during solution treatment and subsequent cooling to enhance beta decomposition in hydrogenated Ti6Al4V.*[39]

2.6.4.2 Decomposition of hydrides

The series of phase transformations in **Figure 2.15** lead to a uniform distribution of hydrides in the sample matrix. Dehydrogenation decomposes the hydrides to form equilibrium alpha **(Equation 2.5)**. Hydrogen diffuses out of saturated alpha and beta phases to form alpha and beta **(Equations 2.6-2.7)**.

$$\delta \rightarrow \alpha + H \uparrow \quad (2.5)$$

$$\alpha_H \rightarrow \alpha + H \uparrow \quad (2.6)$$

$$\beta_H \rightarrow \alpha + \beta + H \uparrow \quad (2.7)$$

The nucleation and growth associated with the formation and decomposition of hydrides refines the microstructure. These nucleated phases spherodise to reduce free energy and this results in fine equiaxed alpha and beta. In addition to hydride decomposition, metastable phase decomposition also contributes to microstructure refinement [38, 39, 42] as shown in **Section 2.6.4.3**.

2.6.4.3 Metastable phase decomposition

Figure 2.16 shows that the hydrogen concentration determines the amount of hexagonal (α') or orthorhombic (α'') martensite that can form. Authors [33-36, 43, 44] reported on the formation of orthorhombic martensite in hydrogenated Ti6Al4V. Qazi et al. [44] stated that hexagonal martensite forms first and it absorbs a maximum of 5 at.% H. The extra hydrogen escapes and concentrates in the non-transformed regions of the matrix. Orthorhombic martensite then forms in these non-transformed regions when their hydrogen content reaches 36 at.% H. [44]

Hexagonal (α') martensite forms when quenching non-hydrogenated Ti6Al4V. Hexagonal martensite needles are orientated at 0°, 30°, 60°, 90° [44] whereas orthorhombic martensite needles prefer 60° and 90° [44] needle orientations. Orthorhombic (α'') martensite forms in titanium alloys that have a large amount of beta stabilizing elements [44] (hydrogen). Hexagonal and orthorhombic martensite phases have different morphologies because of their different crystal structures. Hexagonal martensite has thin needle shaped laths whilst orthorhombic martensite has wider twinned needles. [44]

Orthorhombic and hexagonal martensite can coexist in a microstructure matrix. **Figure 2.16** shows the volume fraction of hexagonal (X'_α) and orthorhombic (X''_α) martensite that can form below 40 at.% H. These volume factions are explained by **Equations 2.8-2.9**.

$$X'_\alpha = (C'' - C_H)/(C'' - C') \quad 2.8 \text{ [44]}$$

$$X''_\alpha = (C_H - C')/(C'' - C') \quad 2.9 \text{ [44]}$$

Where:

C_H -Hydrogen concentration in Ti6Al4V.

C' -Maximum solubility of hydrogen in hexagonal martensite (5 at.% H).

C''-Minimum hydrogen concentration required to form orthorhombic martensite (36 at.% H).

In **Figure 2.16**, regions **a)-c)** show the volume fractions of hexagonal and orthorhombic martensite that form below 40 at.% H. In region a), only hexagonal martensite forms at hydrogen concentrations that are less than 5 at.% H. Region b) shows that orthorhombic and hexagonal martensite phases coexist at hydrogen concentrations that are between 5 at.% H to 35 at.% H. The volume fraction of orthorhombic martensite increases with increasing hydrogen content. This is shown in region c) where only orthorhombic martensite forms at hydrogen concentrations that are above 35 at.% H.

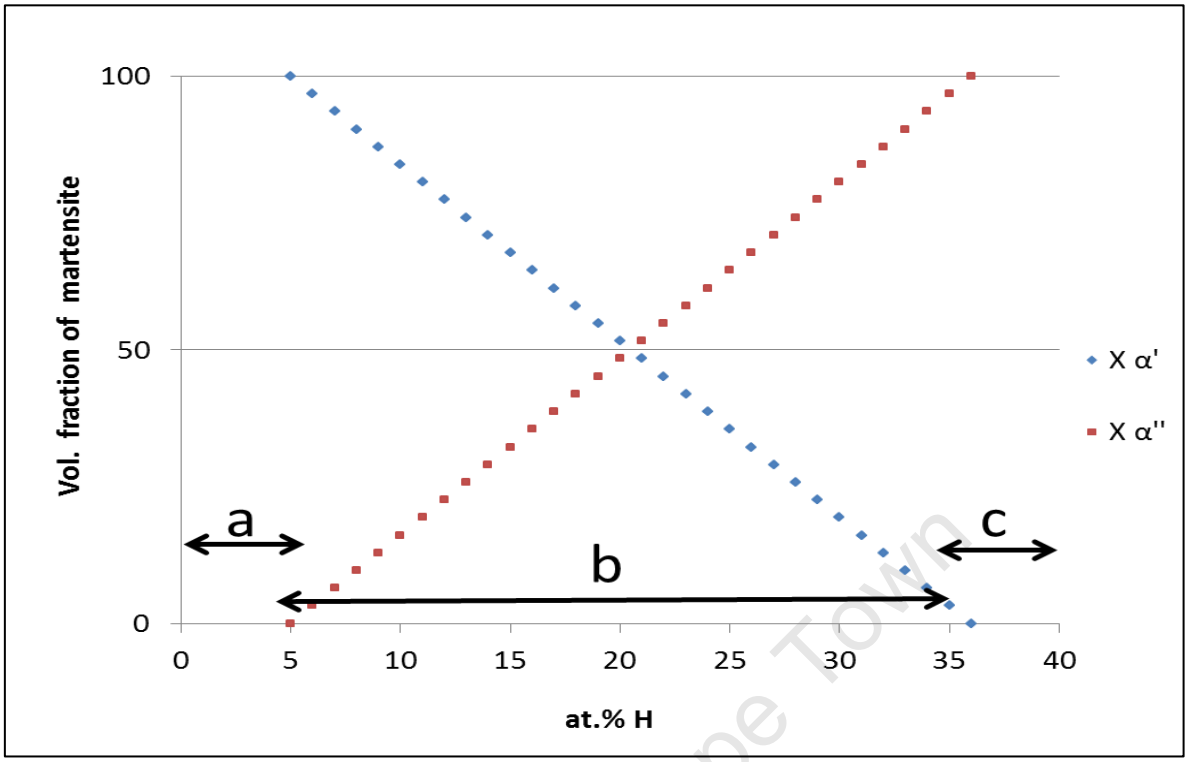

Figure 2.16: a)-c) *shows the volume fractions of hexagonal and orthorhombic martensite that form below 40 at.% H (calculated from equations 2.8-2.9).*

Figure 2.16 is supported by the microstructures in **Figure 2.17**. In **Figure 2.17 a)**, the non-hydrogenated microstructure shows only hexagonal martensite needles. The hydrogenated microstructures in **Figures 2.17 b)-d)** have both hexagonal and orthorhombic martensite needles. The amount of orthorhombic martensite increases with increasing hydrogen content.[44]

In **Figures 2.17 e)-h)**, martensite decomposes to form equilibrium alpha and beta phases. However, after 100 hours of aging the needle morphology is still visible in the microstructure. When martensite is aged above the martensite start temperature, it transforms to metastable beta. [44] The metastable beta transforms to equilibrium alpha and beta phases during aging. If the samples are quenched after aging, the residual metastable beta can transform to form martensite needles. [44] In addition, martensite can also form at slower cooling rates if the Ti6Al4VxH alloy has high hydrogen content.

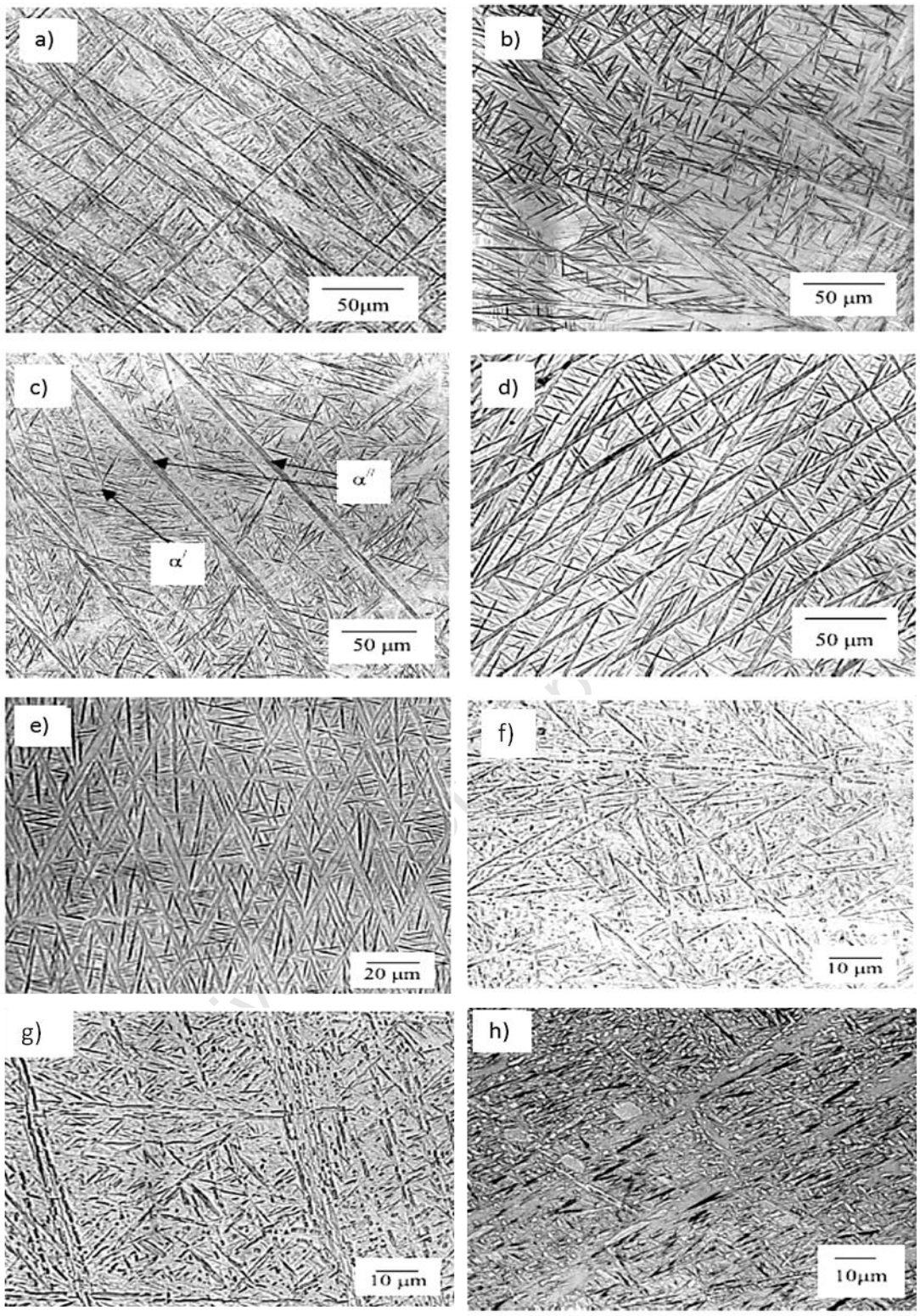

Figure 2.17: *Quenched microstructures of samples containing a) 0, b) 10, c) 20, d) 30 at.%H. Sample (c) was then aged for e) 2, f) 4, g) 60 and h) 100 hours.*[44]

Table 2.1: *A summary of the THP microstructure refining phase transformations*

THP Step	Phase Transformations	Microstructure
HG	$\alpha \rightarrow \alpha_H$ [10, 42] $\beta \rightarrow \beta_H$ [10, 42]	Discontinuous alpha and beta lamellae form upon cooling saturated alpha and beta phases from solution temperature. [38]
Quenching hydrogenated Ti6Al4V	$\beta_H \rightarrow \alpha'/\alpha''$ [10, 35, 36, 41, 44]	Needle morphology oriented at 30°, 60° and 90° depicting hexagonal $\alpha'$and orthorhombic α''needles. Hydrogen decreases the critical cooling rate to the extent that hexagonal and orthorhombic martensite can form at cooling rates of 5°C/min. [10, 35, 44]
MD	$\alpha' / \alpha'' \rightarrow \alpha_H + \beta_H + \delta$ [10, 36, 38, 39, 42]	The bimodal microstructure forms from decomposing martensite to equilibrium alpha and beta. Alpha dissolves less hydrogen, non-dissolved hydrogen forms hydrides.
ED	$\beta_H \rightarrow \alpha_H + \delta + \beta_H$ [10, 36, 38, 39, 41, 42]	Some of the beta decomposes to form saturated alpha and hydride. Residual beta remains embedded in $\alpha + \delta$ matrix [10] because vanadium and hydrogen are beta stabilisers.
Below eutectoid temperature	$\alpha_H \rightarrow \alpha + \delta$ [10]	More alpha which dissolves less hydrogen is stable at lower temperatures. To reduce hydrogen lattice distortion, saturated alpha phase separates to hydrogen rich and hydrogen lean regions. Hydrogen rich regions further transform to form hydrides.
DH	$\delta \rightarrow \alpha + H \uparrow$ [10, 42]	Hydrides decompose to form ultrafine equiaxed equilibrium α and β.

HG - hydrogenation **MD** – martensite / metastable phase decomposition **ED** - eutectoid decomposition **DH** - dehydrogenation

2.7 Effect of hydrogen on hot deformation

Qazi et al. [35, 44, 45] showed that alloying with 30 at.% hydrogen lowers the beta transus temperature from 1000°C to 800°C. This stabilises the softer, more deformable beta phase at lower temperatures (800°C) thus improving low temperature deformation. Alloying Ti6Al4V with hydrogen can also cause embrittlement, [32] therefore hydrogen softening is temperature dependent. [40, 46] **Figure 2.18** shows the effect of hydrogen content and deformation temperature on the flow stress of the Ti6Al4V alloy.

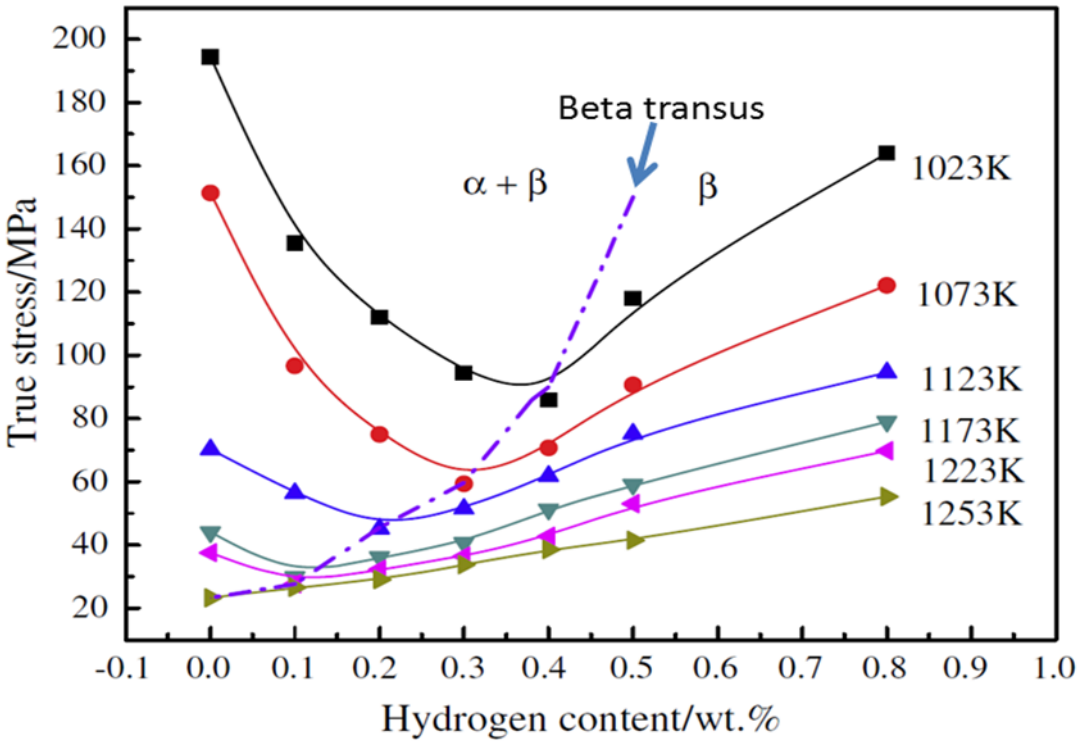

Figure 2.18: *The dependence of hydrogen softening on temperature.* [40]

In **Figure 2.18**, an increase in hydrogen content lowered the beta transus temperature. This is shown by the dotted line shifting from 1253K (980°C) to approximately 1023K (750°C) between 0-0.4 wt.% H (0-15 at.% H). Greater hydrogen softening occurred below the β transus temperature because hydrogen solution strengthening is more prominent above the beta transus. This is because the amount of beta phase increases above the beta transus. Beta phase dissolves more hydrogen when compared to the alpha phase. [26, 40] This increases hydrogen solution strengthening, reduces deformability and thus increases the flow stress.

2.8 Literature summary, hypotheses and research questions

i. From the literature, it has been established that:

- Deformation and recrystallisation refines the prior beta grain size.
- THP refines the morphology by decomposing hydrogen-induced phases.
- Alloying Ti6Al4V with hydrogen reduces its beta transus temperature and this improves low temperature deformability (hydrogen softening).
- Hydrogen softening is temperature dependent.

ii. Therefore, it is hypothesized that:

- Hydrogenation, deformation, recrystallisation and decomposition of hydrogen-induced phases will refine the prior beta grain sizes and the Widmanstätten morphology.
- Deforming at low temperatures will increase the stored deformation energy. This will reduce the minimum temperature required to recrystallise grains and the grain size will decrease with decreasing recrystallisation temperature.

iii. From the objectives and hypotheses, these research questions are formulated:

- What is the nature and extent of hydrogen absorption by as cast Ti6Al4V?
- To what extent can THP refine the microstructure? What are the refinement mechanisms of THP?
- What is the lowest temperature at which as cast Ti6Al4V alloy can be successfully deformed? To what extent can hydrogen alloying improve this deformation limit?
- What is the effect of deforming at lower temperatures on the minimum recrystallisation temperature and the resultant grain sizes?
- What series of post recrystallisation treatments enhance morphology refinement?
- To what extent can the as cast Ti6Al4V microstructure be refined?

3. EXPERIMENTAL PROCEDURE

3.1 Introduction

The experimental procedure in this chapter is designed to provide insight to the research questions outlined in heat treatment and thermomechanical steps i) to iv):

i. Hydrogenation:

- The nature and extent of hydrogen absorption in cast Ti6Al4V.
- The effects of hydrogen absorption on the phase composition, the microstructure and the hardness of hydrogenated Ti6Al4V.

ii. Thermohydrogen processing:

- The effects of beta phase and metastable phase decomposition on the microstructure and properties.

iii. Hot Deformation:

- The effect of hydrogen on the deformability and flow stress of Ti6Al4V.

iv. Post deformation annealing:

- The relationship between deformation temperature, minimum recrystallisation temperature and the resultant grain size.
- The effect of combining deformation, recrystallisation and hydrogen induced phase decomposition on the grain size and the morphology.

3.2 Materials selection

Ti6Al4V rods of 140mm x 20mm (Length x Diameter) were investment cast by the Council for Scientific and Industrial Research (CSIR) in Pretoria South Africa. Their material composition is shown in **Table 3.1**.

Table 3.1: *Composition of as cast Ti6Al4V*

Elements	Ti	Al	V	Fe	C	H	O	N	H	Y
wt.%	89.1	6.4	4.2	0.03	0.01	0.01	0.19	0.01	0.003	0.005

The 140mm x 20mm diameter rods were machined at the University of Cape Town's Mechanical Engineering workshop. Three sets of samples were machined from the 140mm x 20mm diameter rods as shown in **Table 3.2**.

Table 3.2: *Sample dimensions machined from as received Ti6Al4V rods and their uses*

Sample dimensions (L x D)	**Purpose**
1mm x 18mm	Hydrogenation and THP studies
12mm x 18mm	Hydrogenation, Plane strain compression and THP studies
12mm x 10mm	Hydrogenation, Uniaxial compression and THP studies

These were all hydrogenated to study the effect of hydrogenation temperature, time and sample dimensions on hydrogen absorption. After hydrogenation, 12mm x 18mm and 12mm x 10mm specimens were used for plane strain or uniaxial deformation respectively.

Plane strain compressions were performed in order to understand and isolate the effects of heat treatment cycle on deformed microstructures. Plane strain compression deforms part of a heat treated specimen, leaving a control (non-deformed) region as explained in **Section 3.6.2**. After understanding the effects of the heat treatment cycle on the microstructure, uniaxial compressions were then performed.

3.3 Effect of hydrogen absorption on the microstructure and phase composition

To study the nature and extent of hydrogen absorption, mass gain measurements were recorded to the nearest 0.1 mg before and after hydrogenation. Microscopy and X-ray Diffraction (XRD) was used to analyse the microstructure and phase composition of the hydrogenated samples.

3.3.1 Hydrogenation sample preparation

Before heat treatment, samples were rinsed in detergent to breakdown organic substances at the sample surface that may hinder hydrogen penetration into the sample. Samples were then soaked in ethanol in an ultrasonic bath for 15 minutes. After soaking, samples were dried in hot air. Samples were then held by tweezers and inserted into the horizontal furnace at position (6) in **Figure 3.1**. After insertion, samples were pushed to the center of the furnace (7), heated at 5 ^{o}C/min, held at temperature and cooled at 5 ^{o}C/min.

3.3.2 The vacuum furnace

All hydrogenation and dehydrogenation experiments were performed in the vacuum furnace shown in **Figure 3.1**. [27] Its operating vacuum is approximately 10^{-5} Torr.[47]

During hydrogenation the isolation valve (12) is closed and hydrogen gas flows through 1-10. A continuous flow of hydrogen at 101KPa occurs from the cylinder (1) through the piping system (1)-(4) into vacuum furnace through gauge (5). The hydrogen cylinder is either 5 vol.% H or 15 vol.% H balance argon. The gas pressure within the furnace is kept at a constant pressure of 10 KPa above atmospheric pressure (101KPa). The cracker valve (9) opens at 111KPa enabling the gas to flow out of the furnace through (10). This maintains a constant positive pressure of 10KPa in the furnace system (6-9).

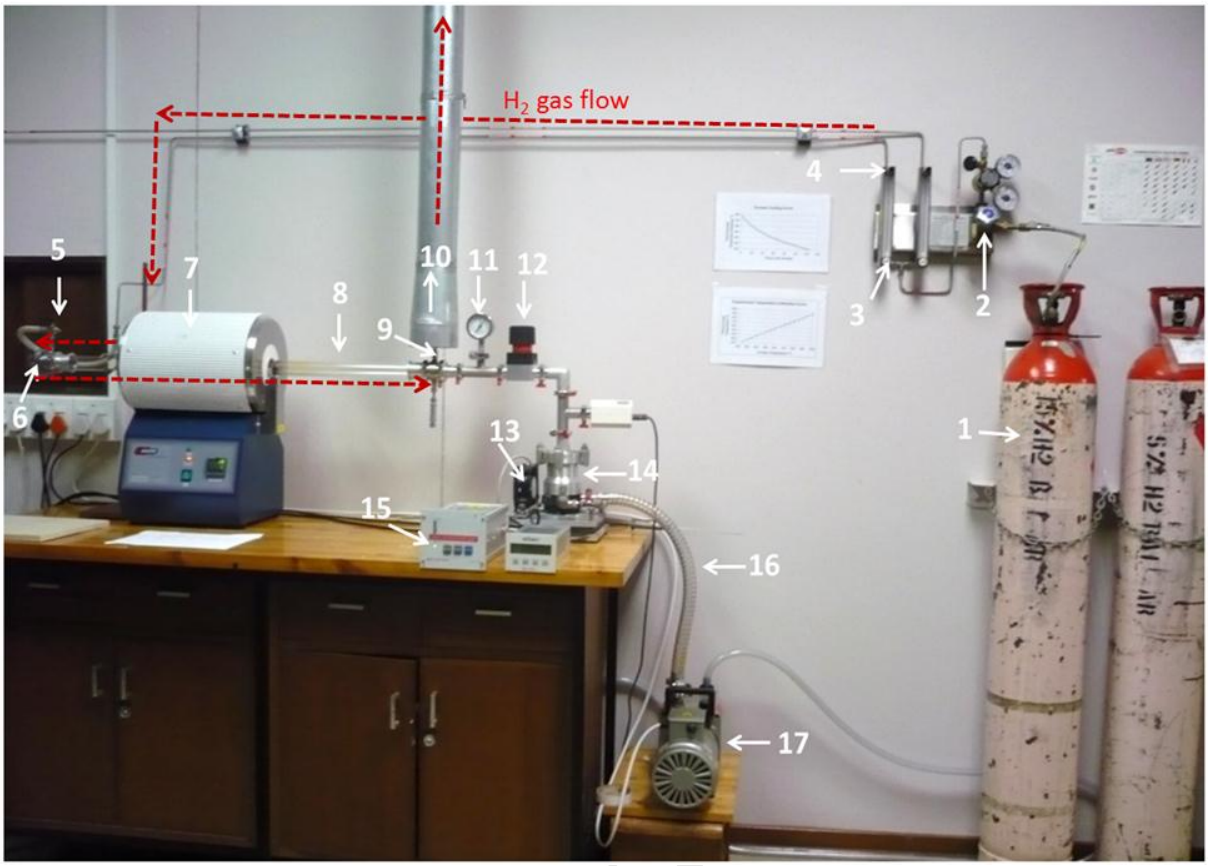

Figure 3.1: *The vacuum furnace that was used for hydrogenation and dehydrogenation.*

1 - 15 vol.% H hydrogen cylinder
2 - Gas regulator
3 - Precision Bore Flowrator FP 1/16-16-G-5/84
4 - Flow rate regulating valve
5 - Controlled 3 way gas inlet valve
6 - End cap
7 - Horizontal Furnace: model TSH 12/50/300-221E (Elite Thermal Systems LTD)
8 - Vacuum chamber (quartz tube)
9 - Crack Valve
10 - Gas extractor
11 - Pressure gauge
12 - Vacuum isolation valve (Speedi valve)
13 - Air cooling system
14 - Turbomolecular pump
15 - Turbo pump controller
16 - Soft vacuum tubing
17 - Rotary backing pump

The partial pressure of hydrogen in the furnace system can be obtained from the ideal gas equation, $PV = nRT$ where R, T and V are constants.

If system (6-9) is 10KPa above atmospheric pressure (101KPa), its constant pressure is

10KPa + 101 KPa

111KPa

5 vol.% hydrogen balance argon:

Partial pressure of 5 vol.% H

P_{H_2} = 5/100 x 111KPa

P_{H_2} = 6KPa

Partial pressure of 95 vol.% argon

P_{Ar} = 95/100 x 111KPa

P_{Ar} = 105KPa

15 vol.% hydrogen balance argon:

Partial pressure of 15 vol.% H

P_{H_2} = 15/100 x 111

P_{H_2} = 17KPa

Partial pressure of 85 vol.% argon

P_{Ar} = 85/100 x 111

P_{Ar} = 94KPa

The vacuum and the gas flow component of the furnace are separated by the isolation valve (12). The vacuum system which enables dehydrogenation is shown in 13-17. During dehydrogenation valves (2, 4 and 5) are closed to prevent gas inlet into the system and the vacuum isolation valve (12) is opened. The backing pump (17) and the turbomolecular pump (14) are used to obtain a vacuum of up to 10^{-5} Torr on the system (6-17).

3.3.3 Hydrogenation heat treatment protocol

Hydrogenation and dehydrogenation heating and cooling rates were kept constant at 5 °C/min. The hydrogenation protocol is shown in **Table 3.3**.

Four hydrogenation parameters were varied, namely:

- Hydrogen gas atmosphere concentration - 5 vol.% H or 15 vol.% H.
- Hydrogenation temperature range - 550°C to 950°C.
- Hydrogenation time - 3 or 8 hours.
- Sample size dimensions (L x D)-1mm x 18mm, 12mm x 18mm, 12mm x 10mm.

In **Table 3.3**, a row of ticks (✓) (from the left to the right) represents a combination of a sample`s hydrogenation variables. Multiple samples were hydrogenated at each variable combination to ensure reproducibility of results.

For example, in **Table 3.3** row 1, multiple 1 mm x 18 mm diameter samples were hydrogenated for 3 hours at 950°C in 5 vol.% H atmosphere.

After understanding the nature and extent of hydrogen absorption, it was important to determine the effects of the absorbed hydrogen on phase transformations and resultant microstructures. Two widely used thermohydrogen processing routes (THP) were studied. These encourage beta decomposition (THP-BD) and metastable phase decomposition (THP-MD) as described in **Section 3.4**.

Table 3.3: *Hydrogenation processing window*

H_2 gas vol.%		Hydrogenation Temperature °C								Soak time hours		Sample dimensions L (mm) x D (mm)		
5	15	950	900	850	800	750	700	650	550	3	8	1 x 18	12 X 18	12 x 10
✓		✓								✓		✓		
✓			✓							✓		✓		
✓				✓						✓		✓		
✓					✓					✓		✓		
✓						✓				✓		✓		
✓							✓			✓		✓		
✓								✓		✓		✓		
✓									✓	✓		✓		
	✓	✓								✓		✓		
	✓		✓							✓		✓		
	✓			✓						✓		✓		
	✓				✓					✓		✓		
	✓					✓				✓		✓		
	✓						✓			✓		✓		
	✓							✓		✓		✓		
	✓								✓	✓		✓		
	✓							✓			✓	✓		
	✓			✓						✓			✓	
	✓					✓				✓			✓	
	✓							✓		✓			✓	
	✓							✓			✓		✓	
	✓							✓		✓				✓
	✓							✓			✓			✓

3.4 Effect of hydrogen induced phase decomposition on the microstructure

Section 3.4 excludes deformation, it is aimed at studying the solitary effects of thermohydrogen processing (THP) on the microstructure. THP procedures in **Figures 3.3-3.4** were performed on non-deformed 1mm x 18mm diameter samples. This was done to study the effect of beta decomposition (THP-BD) and metastable phase decomposition (THP-MD) on the microstructure.

The samples used in THP-BD were prior hydrogenated to 20±3 at.% H. The samples used in THP-MD studies were prior hydrogenated to 20±3 at.% H or 28±3 at.% H. Hydrogenation to 20±3 at.% H was performed in 15 vol.% H at 850°C for 3 hours and hydrogenation to 28±3 at.% H was performed in 15 vol.% H at 650°C for 3 or 8 hours. THP-BD and THP-MD experiments were done in a box furnace supplied by Kiln Contracts Cape Town. All samples annealed in the box furnace were coated in ceramic isomol as shown in **Section 3.4.1**.

3.4.1 Thermohydrogen processing (THP) sample preparation

In **Figure 3.2**, isomol acted as a barrier which prevented high temperature oxidation of Ti6Al4V. In addition isomol prevented the alloyed hydrogen from diffusing out of the samples at high annealing temperatures. The isomol coating was prepared by mixing isomol powder and ethanol at a ratio of 3:1. The ratio of isomol to ethanol determined the thickness of the coating. Each sample was dipped into the coating mixture and dried in hot air. The dipping and drying was repeated until no sample surface was exposed and the coating was completely dry as shown in **Figure 3.2**.

***Figure 3.2**: 1mm x 18mm diameter sample coated in isomol for box furnace annealing.*

3.4.2 THP protocols

To study the effect of beta and metastable phase decomposition on the microstructure, two main THP routes were used as shown in **Figures 3.3-3.4**. The heating rate (5 ^{o}C/min), the solution treating temperature (900^{o}C) and solution treating time (1 hour) were kept constant. Three parameters were varied namely:

- Cooling rates (quenching versus cooling at 5 ^{o}C/min from solution temperature).
- Annealing temperature.
- Annealing time.

Table 3.4: *A summary of variables in THP-MD and THP-BD experiments*

Quenched from 900^{o}C (THP-MD)		**Cooled at 5^{o}C/min from 900^{o}C (THP-BD)**	
Annealing Temp. ^{o}C	Annealing Time (hrs)	Annealing Temp. ^{o}C	Annealing Time (hrs)
580	1.5 to 72	700	1 to 30
		600	1 to 30
		500	1 to 30

hrs - hours

In **Table 3.4**, metastable phase decomposition was only performed at 580^{o}C, at annealing times of up to 72 hours. Beta decomposition was performed at three different temperatures namely 700^{o}C, 600^{o}C and 500^{o}C for up to 30 hours.

In **Figure 3.3**, samples were prior hydrogenated to 20±3 at.% H. These were coated in isomol and solution treated in a non-hydrogen atmosphere at 900^{o}C for an hour. Sample (a) was quenched after solution treatment to ensure that 900^{o}C was a single-phase beta region. Sample (b) was furnace cooled at 5^{o}C/min from solution temperature to room temperature. This was done to investigate the difference between the furnace cooled and the beta decomposed microstructures. A series of samples c)-e) were furnace cooled at 5^{o}C/min to beta decomposition temperatures 700^{o}C, 600^{o}C and 500^{o}C respectively. These were held for up to 30 hours as shown in **Table 3.4**. All samples were quenched at the end of beta decomposition. This was done to eliminate any further phase transformations that may result from slow cooling.

The decision to beta decompose at temperatures 700°C, 600°C and 500°C was informed by the temperature time transformation (TTT) diagram in **Figure 3.3 f)**. The TTT diagram shows that the nose temperature for beta decomposition is at 600°C. Therefore, it would take less annealing time to start beta decomposition at 600°C when compared to 700°C and 500°C. In this way, microstructure evolution at beta decomposition temperatures that are above or below the eutectoid temperature (600°C) can be traced **(Figure 3.3 f)**.

In **Figure 3.4**, samples were prior hydrogenated to 20±3 at.% H or 28±3 at.% H. These were coated in isomol and solution treated in a non-hydrogen atmosphere at 900°C for an hour. After solution treating, all samples were water quenched **(Figure 3.4 a)**. Quenched samples were reheated from room temperature to 580°C at 5°C/min, this was done to decompose metastable phases as shown in **Figure 3.4 b)**.

The decision to decompose metastable phases at 580°C was informed by the temperature time transformation (TTT) diagrams in **Figures 3.4 c), d)**. [44] These were obtained by studying the effect of aging temperature and time on hardness. In this study, hardness increased to a peak value and plateaued with increased annealing (aging) time. [44] The increase and subsequent plateau of hardness values marked the start (t_s) and the completion (t_e) of martensite decomposition respectively.[44] In addition, the annealing (aging) temperature 580 °C had the highest hardness increase at 30 at.% H. [44]

Qazi et al.`s [44] findings show that martensite decomposition is annealing (aging) temperature and time dependant. The TTT diagrams in **Figures 3.4 c)**, **d)** are nose shaped showing that martensite is least stable at certain critical annealing or nose temperatures. In **Figures 3.4 c)** and **d)**, the critical annealing temperature is represented by the symbol T_n and it decreases with an increase in hydrogen concentration from 20 to 30 at.% H. [44] Interestingly, in **Figure 3.4 d)** the completion of martensite decomposition (t_e) at 580°C was clearly marked at 30 at.% H whereas it was not shown at 20 at.% H **(Figure 3.4 c)**. Therefore, the aging temperature 580°C was chosen because it showed the highest hardness increase[44] and its (t_e) was not reported at 20 at.% H.

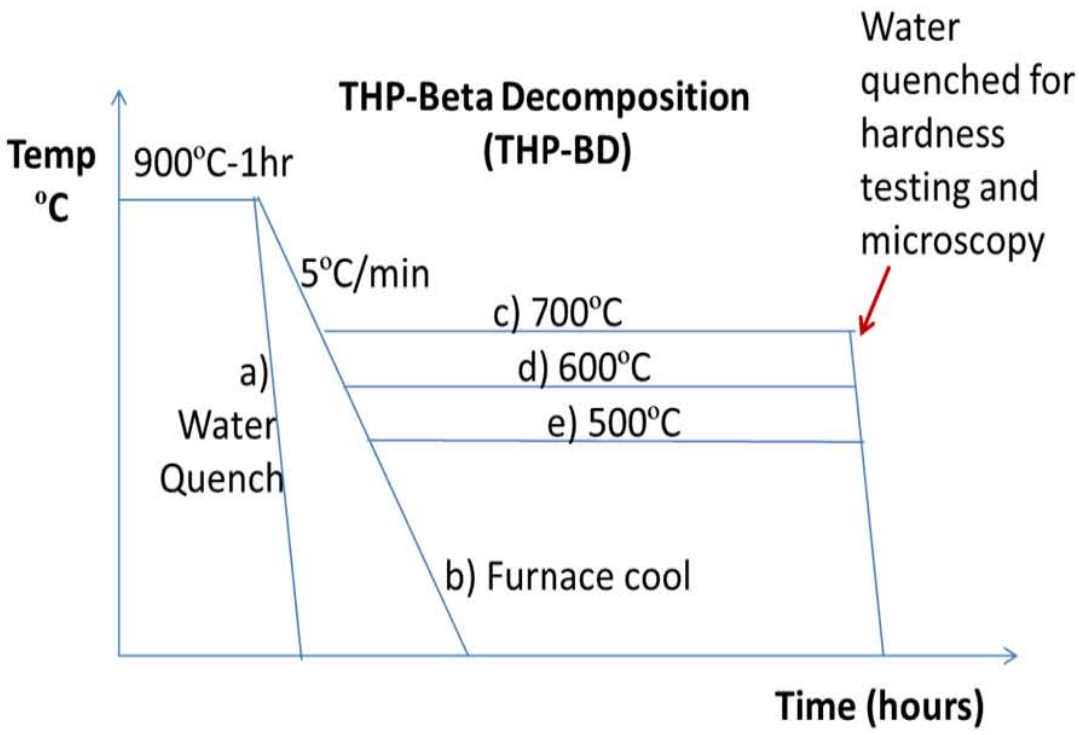

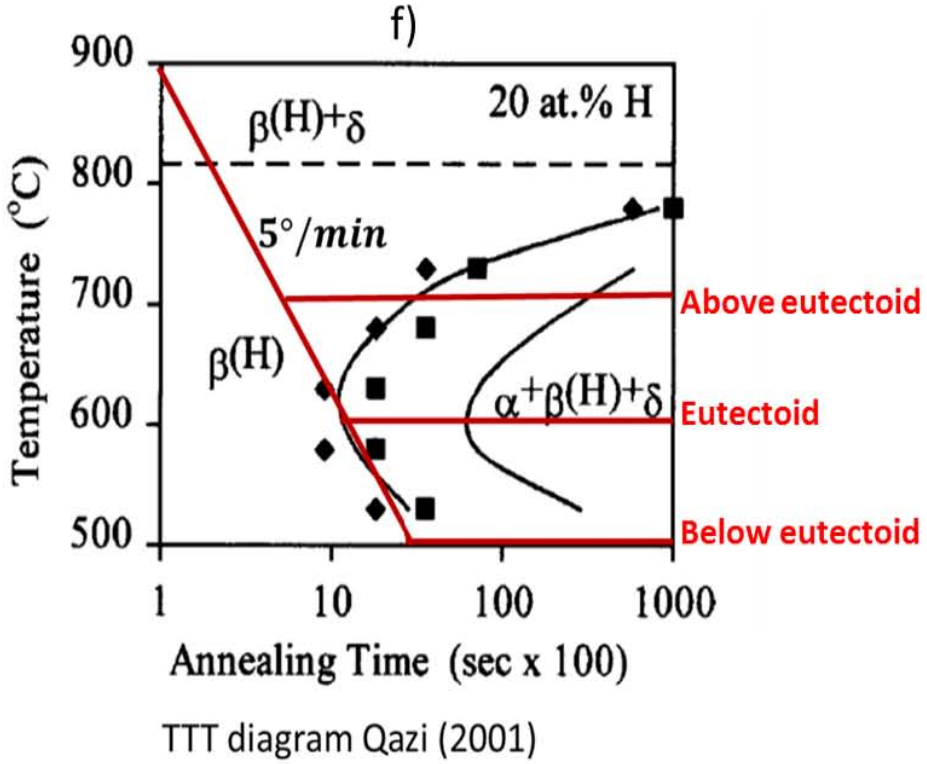

TTT diagram Qazi (2001)

Figure 3.3: *THP-BD protocol (a-e) to study the effect of beta decomposition temperature and time on the microstructure. Specimens were beta decomposed at 700°C, 600°C and 500°C to investigate microstructure evolution at beta decomposition temperatures that are above or below the eutectoid temperature as shown in f).*

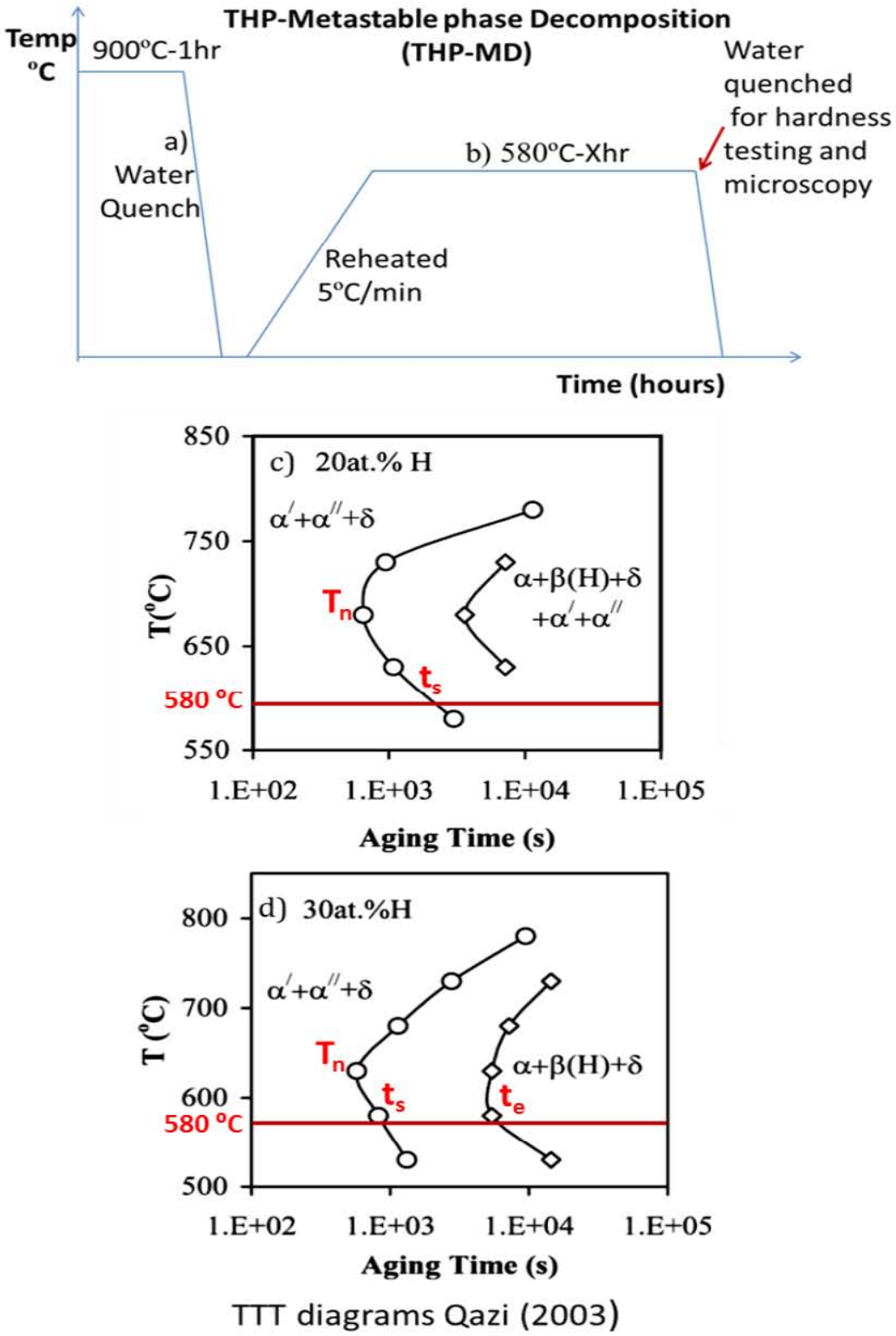

Figure 3.4: *THP-MD protocol (a, b) to study the effect of aging at 580°C on the microstructure. On TTT diagrams (c, d) the symbols T_n, t_s and t_e represent the nose temperature (T_n), the start (t_s) and completion (t_e) of martensite decomposition respectively.*

3.5 The effect of hydrogen on the deformability

In **Section 3.4**, thermohydrogen processing (THP) was perfomed on non-deformed samples to examine microstructure evolution in THP treatments. **Section 3.5**, examines the combined effects of THP and deformation on the microstructure and deformability. Hydrogen (20±3 at.% H) was used to improve deformability and all deformed samples were quenched. Quenching formed metastable phases and these were decomposed in a subsequent metastable phase decomposition step (THP-MD-**Figure 3.4**).

All hot compressions (deformations) were done on the Gleeble 3800 at a vacuum of 10^{-5} Torr. The heating, isothermal hold and cooling cycles were programmed using Quicksim. Quicksim is a computer programme that generates Gleeble Script Language (GSL) files. GSL files control the Gleeble`s heating, isothermal hold and cooling cycles **(see Appendix B)**.

3.5.1 Hot compression sample preparation

Hot compression samples were prepared using steps (1) to (7) shown in **Figure 3.5**. The flat ends of the sample that contact the anvils were covered by a Graphite|Tantalum|Graphite foil sandwich (1-3).

Two 19 mm diameter graphite foils (1) were folded around a 15x15 mm^2 tantalum foil (2) for lubrication. Thermocouples were then welded at the centre of the sample (4) using a thermocouple welder. The foil sandwiches (3) were attached to the sample flat ends using conductive carbon paste (5).

The conductive carbon paste was made out of a 2:1 mixture of adhesive and carbon respectively. A single tube ceramic insulator (6) was inserted on one of the thermocouples at the base of the sample to prevent their non-insulated wires from touching. To ensure accurate temperature readings, the distance between the thermocouples was kept below 1 mm. High temperature cement (7) was placed at the thermocouple welding point, to stabilise thermocouples at high temperatures (1000°C).

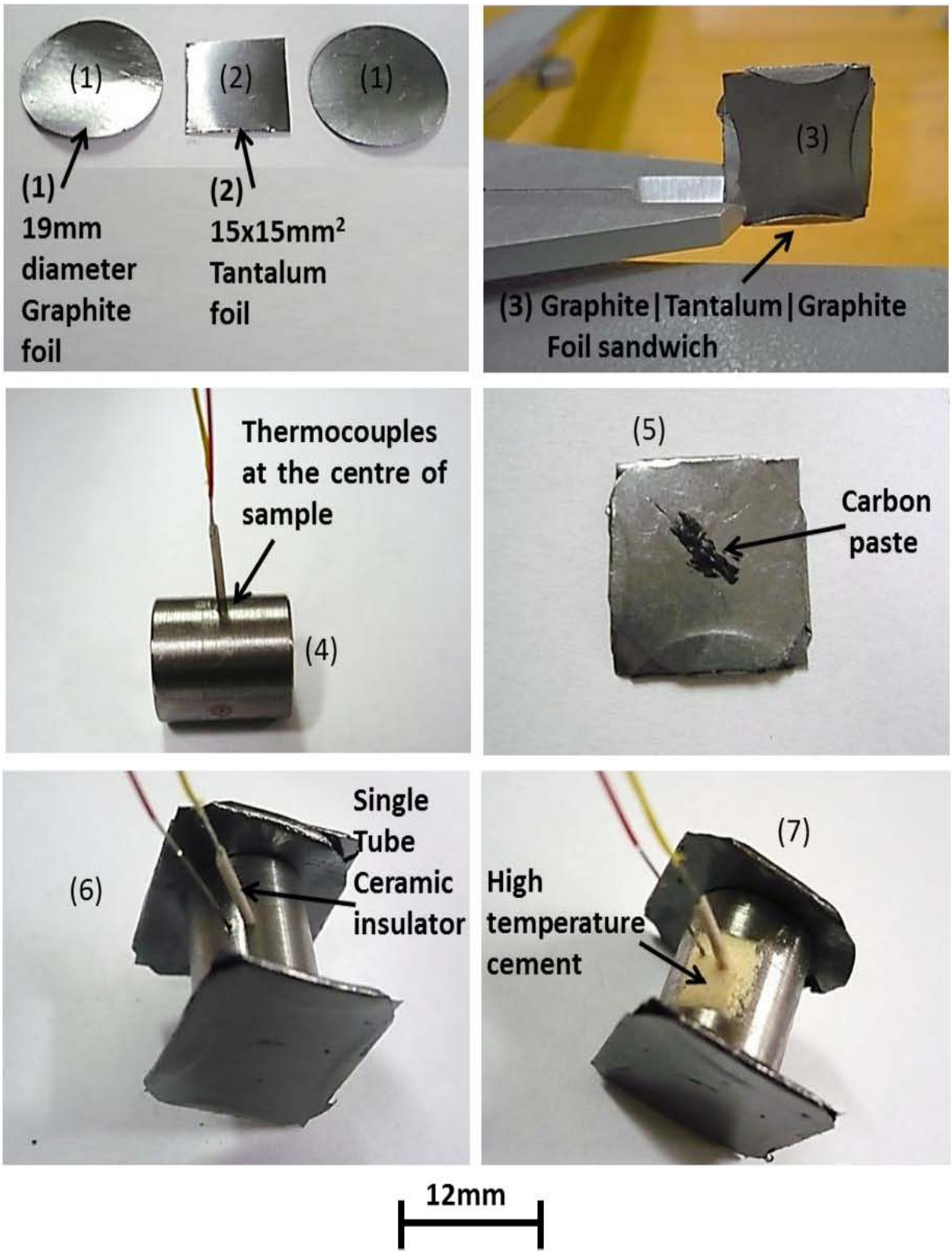

Figure 3.5: *The sample preparation protocol for Gleeble 3800 uniaxial compressions.*

3.5.2 Hot compression protocol

Plane strain (12mm x 18mm diameter) or uniaxial compression (12mm x 10mm diameter) samples were hydrogenated to 20±3 at.% H at 650°C for 3 hours and deformed. As cast (c) and dehydrogenated (HD) samples were also compressed (deformed) to justify the hydrogen softening effect. The hot compression heating and air quenching rates were kept constant, the variable parameters were:

- Starting material [as cast (C) or hydrogenated (H) or dehydrogenated (HD)].
- Deformation temperature.
- Strain.
- Strain rate.

Table 3.5: *Gleeble 3800 deformation processing window and its variable parameters*

Starting material	Def. Temp. °C	Strain			Strain rate s^{-1}	
		0.2	0.5	0.8	1	10
As cast (C)	1000	✓	✓		✓	✓
As cast (C)	900	✓	✓		✓	✓
As cast (C)	800	✓	✓	✓		
Hydrogenated and dehydrogenated (HD)	900	✓	✓	✓		✓
Hydrogenated and dehydrogenated (HD)	800		✓	✓		✓
Hydrogenated at 650 for 3hrs (H)	750	✓	✓	✓		✓
Hydrogenated at 650 for 3hrs (H)	700	✓	✓	✓		✓
Hydrogenated at 650 for 3hrs (H)	600	✓	✓	✓		✓
Hydrogenated at 650 for 3hrs (H)	550		✓	✓		✓
Hydrogenated at 650 for 3hrs (H)	500		✓	✓		✓

Def. Temp. - Deformation temperature

In **Table 3.5**, a row of ticks (✓) represents a combination of deformation variables. For example, in row 1 four as cast (c) samples were deformed at 1000°C, at 20% (0.2) or 50% (0.5) strain and strain rates of 1 s^{-1} or 10 s^{-1}. Multiple samples were deformed at each deformation variable combination to ensure reproducibility of results.

Figure 3.6 shows the programmed (red) and the actual thermocouple readings (blue) of heating, isothermal hold temperature, and air quenching rates.

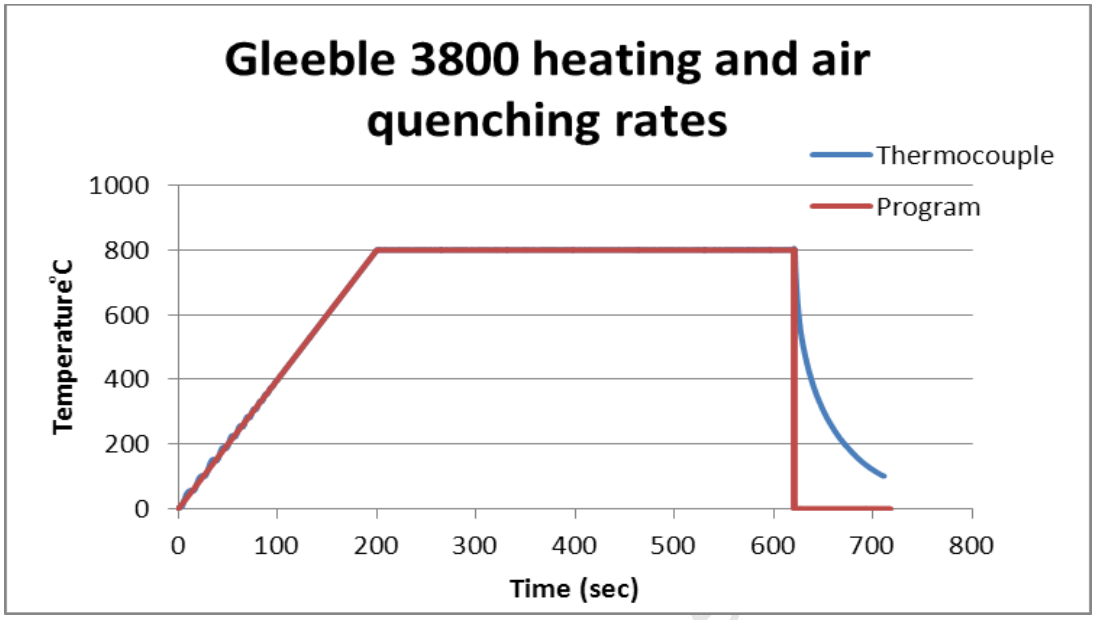

Figure 3. 6: *The heating and quenching rates used in the Gleeble 3800.*

In **Figure 3.6**, the thermocouple (blue) and Quicksim (red) graphs show a similar heating and isothermal holding trend. The samples were heated at 4°C/sec and isothermally held for 7 minutes to ensure a homogenous temperature distribution within the sample. After holding, samples were deformed and quenched to prevent further phase transformations.

The Ti6Al4V alloy has no significant phase transformations below 500°C, therefore its critical quenching temperature range is above 500°C. Upon quenching, the programme curve (red) shows an immediate drop in temperature from 800°C to 500°C in zero seconds. The thermocouple shows that the sample quenched from 800°C to 500°C degrees in approximately 15 seconds (1200°C/min). Deformation and quenching induced strain energy and formed metastable phases in the microstructure respectively. Therefore, two separate post deformation annealing treatments were performed to recrystallise new grains and decompose metastable phases. Lastly, samples were dehydrogenated to decompose hydrides and remove hydrogen.

3.6 Metallographic analysis

3.6.1 Explanation of the systematic sample labelling system

A sample labelling system was used to reflect the heat treatment history of that particular sample. Samples hydrogenated in 5 vol.% H or 15 vol.% H gas atmosphere are named 5H or 15H respectively. In **Table 3.6**, A dash (-) means a heat treatment step was not performed. Heat treatment conditions are similar for easier understanding.

Table 3.6: *Explanation of the sample numbering system*

	Hydrogenation			**Deformation**			**Recry.**		**THP-MD**		**Vac anneal**	
	Atm vol.%	Temp ºC	Time hrs	Temp ºC	Strain (ε)	Strain rate (έ) s^{-1}	Temp ºC	Time hrs	Temp ºC	Time hrs	Temp ºC	Time hrs
a)	5H	650	8	-	-	-	-	-	-	-	-	-
b)	15H	650	8	-	-	-	-	-	-	-	-	-
c)	-	-	-	800	05	10	-	-	-	-	-	-
d)	15H	650	8	800	05	10	-	-	580	8	675	16
e)	15H	650	8	800	05	10	900	1	580	8	675	16

Recry. - Recrystallisation **Atm** - hydrogen gas atmosphere **hrs** - hours

In **Table 3.6**, the numbering system denotes heat treatment order. If a heat treatment step was not done, for example d) was not recrystallised the next annealing step (THP-MD) follows after deformation on its name. The resultant sample names are in square brackets bold and italicized on a)-e).

a) Hydrogenated in a 5 vol.% H atmosphere for 8 hours at 650ºC ***[5H650-8]***.
b) Similar sample to a), but hydrogenated in a 15 vol.% H atmosphere ***[15H650-8]***.
c) Non-hydrogenated (as cast) sample deformed at 800ºC, 50% strain (0.5) and strain rate of 10 s^{-1} ***[800-05-10]***.
d) Hydrogenated, deformed and annealed sample. It was annealed at 580ºC for 8 hours to decompose metastable phases and vacuum annealed at 675ºC for 16 hours to remove hydrogen and decompose hydrides ***[15H650-8-800-05-10-580-8-675-16]***.
e) Hydrogenated, deformed and recrystallised at 900ºC for 1 hour, metastable phase decomposed and vacuum annealed ***[15H650-8-800-05-10-900-1-580-8-675-16]***.

3.6.2 Cutting

A Buehler Isomet Low speed saw supplied by Apollo scientific CC was used to cut or section the deformed (forged) specimens. **Figures 3.7 a)** and **b)** are schematic images showing uniaxial and plane strain compressed samples. Plane strain compression was performed to differentiate the individual effects of the heat treatment cycle and deformation on the microstructure. After deformation, heat treatment regions R1 and R2 in **Figure 3.7 b)** would have undergone the same heat treatment cycle. The only difference between them would be that R1 is deformed and R2 is non-deformed. After understanding the individual effects of heat treatment on the microstructure, uniaxial compressions were performed.

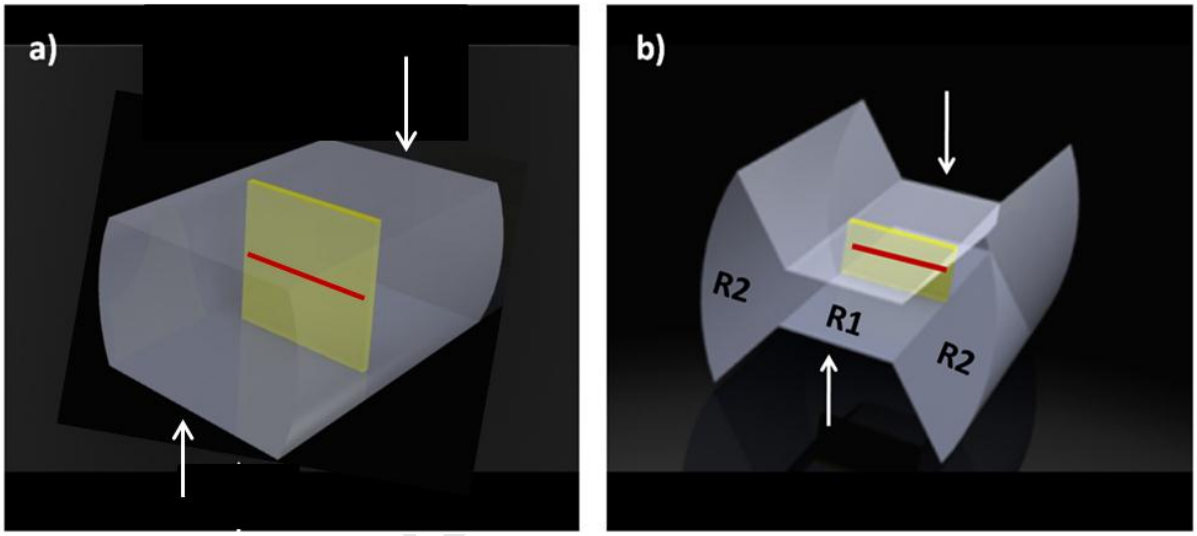

Figure 3.7: *Schematics of a) uniaxial and b) plane strain compressed samples. In a) and b), the compression direction is vertical as shown by the white arrows. In b), R1 and R2 are deformed and non-deformed regions of a plane strain compressed sample respectively.*

In **Figure 3.7**, 12mm x 10mm and 12mm x 18mm diameter samples were used for all a) uniaxial and b) plane strain compressions respectively **(see Table 3.2)**. The compression direction is vertical as shown by the white arrows on images a) and b). All compressed samples were sectioned (cut) on a plane parallel to their compression direction (axis). This plane is shown in yellow on images a) and b). On these planes, the area of interest that was used for microstructure analysis is shown by a red line.

3.6.3 Hot Mounting

Mounting was done on a Struers Labopress-3 at 180ºC for 12 minutes (6 min heating and 6 min cooling) using a 20KN force. An acrylic resin, which is a thermoplastic, was used for mounting. This softens at 180ºC and molds to the sample. During mounting, the resin and sample mold is cooled under a 20KN force to get good adhesion between resin and sample.

3.6.4 Polishing

Polishing was done on a Struers Tegrapol-11, coupled to a Tegradoser-5. The equipment was supplied by IMP solutions. This was set to autodose at 3/10 and 4/10 for 9µm and attack solutions respectively. This means that for every 10 rotations, the polishing medium was dosed out 3 or 4 times respectively as shown in **Table 3.7**.

Table 3.7: *Polishing protocol*

Polishing step	Struers Pad	Medium	Time (min)
Grinding (800 gritt)	MD FUGA	Water	4
Polishing	MD DUR/ DAC	9µm	10
Polishing	MD NAP	Attack solution	10
Washing	MD NAP	Water	5

Grinding was done for 4 minutes using an 800µm SiC paper attached to the Struers adhesion plate MD FUGA. This was done to obtain a high material removal rate to obtain a flat sample surface within a short time period.

A diamond abrasive with 9 µm grain size and a MD DUR pad were used to remove scratches after grinding. Autodosing was strategically set to provide smallest quantities of polishing media in short time intervals. This reduced wastage whilst providing enough lubricant against friction. The rotation speed was kept at 300 rpm during grinding to increase abrasion and material removal. During polishing, 150 rpm was used to limit abrasion and reduce scratching. An attack solution which is a mixture of 25 ml colloidal silica (OP-S) and 5 ml H_2O_2 (50%) was used in the final polishing step. This provided a combination of chemical attack and gentle abrasion to remove deformation and produce a mirror finish.

3.6.5 Etching

Samples were etched for 30 seconds using Krolls reagent and its composition is shown in **Table 3.8**. After etching they were flushed with tap water to stop the corrosion reaction. The sample surface was cleaned with cotton wool and detergent. After cleaning, samples were rinsed with distilled water and ethanol and dried in hot air.

Table 3.8: The composition of Krolls reagent

Components	Volume
50% $HN0_3$	6ml
50% HF	3ml
Distilled water	100ml

3.6.6 Microstructure and phase composition analysis

Attack polished and etched samples were used to obtain qualitative topographical information from light and scanning electron microscopy (SEM). A Reichert Me F3 light microscope was used to examine the etched samples in bright field mode. This obtained qualitative microstructural information which acted as a precursor for the quantitative orientation mapping technique known as electron backscatter diffraction (EBSD).

Scanning electron microscopy (SEM) was then performed on the etched samples to obtain high resolution images using the Nova NanoSEM 230. An accelerating voltage of 20kV, a spot size of 5 (0.9 nano Amps) and a varying working distance was used to capture images. Topographical microstructure information was obtained by detecting secondary electrons using the Everhart-Thornley (ETD) detector.

Quantitative grain size and phase analysis was obtained from attack polished and un-etched samples using the EBSD technique in the SEM. EBSD obtained crystallographic orientation information at certain scanned points on selected regions of the sample. The step size between these points was kept at 0.1 μm for high and 0.5 μm to 1.5 μm for low resolution EBSD scans respectively.

The HKL Channel 5 software supplied by Oxford Instruments was used to post-process and to analyse the obtained EBSD data. Each scanned point was coloured according to its orientation, relative to Euler angle positions on a Cartesian axis. This information was displayed in Euler colour maps whereby groups of similar coloured points were regarded as areas of similar orientation.

On these similarly coloured areas, misorientations of less than 15° were low angle grain boundaries (LAGB) and were regarded as subgrains. Areas that had a misorientation greater than 15° had high angle grain boundaries (HAGB) and they were demarcated as separate grains. Grain diameters were measured to quantify the extent of grain refinement and the information was presented on a grain size distribution histogram.

X-ray diffraction (XRD) was performed to determine the differences between the phase constituents of the as cast and the hydrogenated samples. The solution of hydrogen and the formation of hydrides cause a lattice volume expansion. This causes XRD peaks to widen and shift to lower 2 theta positions. This is mostly prominent on alpha phase peaks because the alpha phase absorbs a lesser amount of hydrogen when compared to the beta phase. [40]

XRD was carried out in a Bruker D8 Advance X-ray diffractometer equipped with a cobalt source (λ = 1.78897 Å) and a Bruker Vantec position sensitive detector. The optics were set to parallel beam geometry to prevent possible peak shifts that may be caused by sample height differences. The sample height was kept relatively constant because only 1x18mm diameter samples were used for XRD analysis. The scan range was at 2 theta 80°-100° in order to cover enough alpha and beta peaks. The stepsize and the time per step were kept at 0.001151626° and 0.5s respectively.

4. RESULTS AND DISCUSSION

4.1 Introduction

The experimental findings are presented in the following order:

i. **Characterization of the as cast Ti6Al4V microstructure:**
   - Alpha phase morphology and porosity.

ii. **Effect of hydrogen absorption on as cast Ti6Al4V:**
   - Extent of hydrogen absorption.
   - Phase composition of hydrogenated Ti6Al4V.
   - Microstructure analysis of hydrogenated Ti6Al4V.
   - Effect of hydrogen absorption on hardness.

iii. **Effect of beta decomposition on refinement:**
   - Microstructure and hardness evolution from beta decomposition.

iv. **Effect of metastable phase decomposition on refinement:**
   - Microstructure and hardness evolution from martensite decomposition.

v. **Effect of hydrogen on deformability and flow stress:**
   - Deformation limits of as cast Ti6Al4V marked by flow instability and the onset of sample cracking.
   - Effect of hydrogen on flow stress.

vi. **Post deformation annealing:**
   - Relationship between deformation temperature, minimum recrystallisation temperature and grain sizes.

4.2 Characterization of the as cast microstructure

Figure 4.1 is a picture montage of 300 light microscope images scaled at 2cm:500µm. This was done to provide the complete as cast Ti6Al4V microstructure variation throughout the sample surface. Hardness testing was done across the sample surface and the indents were spaced 1mm apart from one another.

Figure 4.1 A-E shows that the as cast Ti6Al4V microstructure has large prior beta grain sizes (A), which are separated by grain boundary alpha (B). In the prior beta grain there are colonies of Widmanstätten (C) alpha and beta morphology, which give rise in many cases to the basketweave morphology (D). The 1mm indent spacing (G) shows that the average diameter of the prior beta grains is approximately 2mm. Porosity (E and F) is occasionally observed in the microstructure.

The large prior beta grain sizes result from slow cooling below the solidus temperature during casting. When the casting is further cooled below the beta transus, alpha nucleates at the prior beta grain forming grain boundary alpha. The alpha grows from the prior beta grain boundary into the beta grain via a specific orientation related to the Burgers relationship. This is known as Widmanstätten or lamellar growth.

Basketweave morphology forms when it becomes more energy efficient to nucleate new alpha lamellae than grow the existing lamellae. There are twelve possible orientation variants of alpha in beta. Multiple occurrences of these orientation variants form the basketweave morphology. Therefore, the basketweave morphology represents repeated nucleation of the Widmanstätten growth morphology.

The aim of this work is to refine the as cast Ti6Al4V microstructure by reducing its prior beta grain sizes and refining its morphology. This will be attempted firstly by hydrogen doping and heat treatments (thermohydrogen processing) and secondly by hydrogen doping and deformation.

Figure 4.1: *Optical image of the as cast Ti6Al4V microstructure showing A) large prior beta grain sizes, B) prior beta grain boundary, C) Widmanstätten growth giving rise to D) basketweave morphology E)-F) porosity and G) hardness testing indents.*

Figure 4.2 a) shows the typical as cast Ti6Al4V Widmanstätten morphology. As cast Ti6Al4V has equilibrium alpha (hcp) and beta (bcc) phases **(Figure 4.2 b)** which formed during slow cooling. Comparing **Figures 4.2 a)** and **b)** illustrates the lamellar (or plate-like growth) of the alpha phase, as the beta phase decomposes below the beta transus temperature during cooling. The beta phase appears as residual thin lamellae between the alpha phase transformation product.

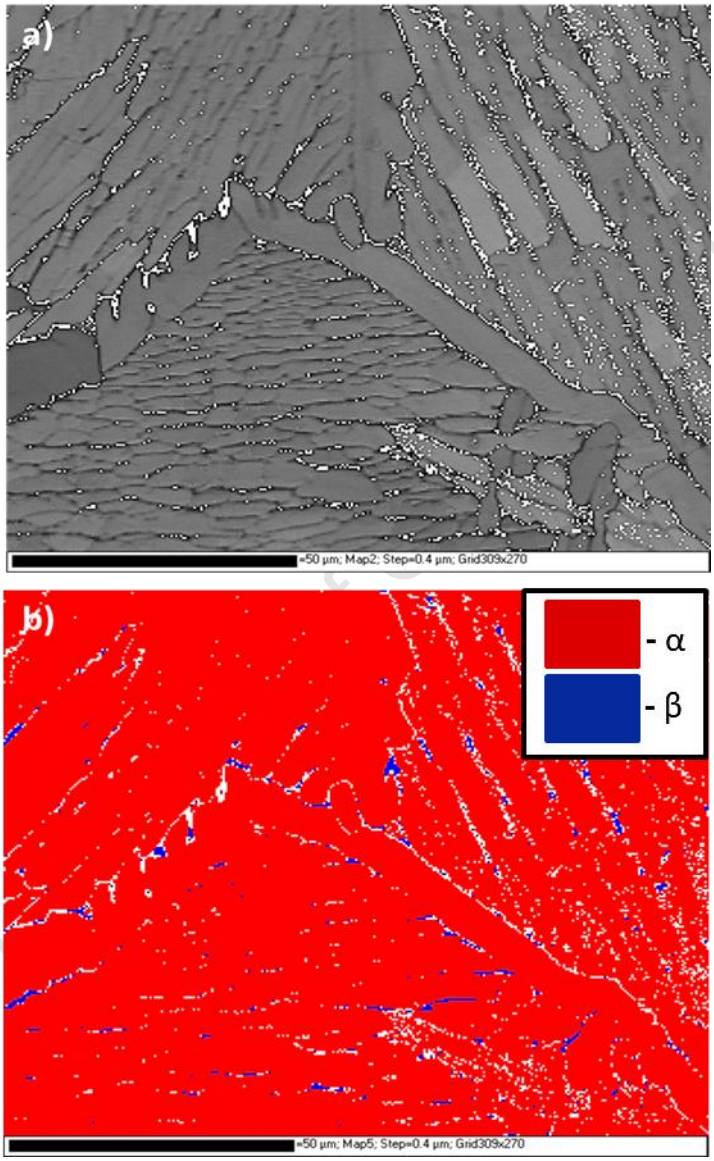

Figure 4.2: *EBSD a) band contrast and b) phase maps showing the phase composition of as cast Ti6Al4V. In image b), red is hcp phase, blue is bcc phase and non-indexed regions are white.*

4.3 Effect of hydrogen absorption on the microstructure

4.3.1 Extent of hydrogen absorption

In order to assess the effect of hydrogen absorption on the as cast Ti6Al4V microstructure, it was necessary to quantify the amount of hydrogen absorbed. This was done by weighing samples to the nearest 0.1mg before and after hydrogenation. The mass gain caused by hydrogenation was equated to atomic percent (at.%) hydrogen absorption. The effect of hydrogenation temperature, concentration of hydrogen gas and sample size on the absorption of hydrogen is shown in **Figure 4.3**. The legend in **Figure 4.3** is explained in **Table 4.1**. The letter X on the legend represents hydrogenation temperature. It substitutes the temperatures shown on the x-axis in **Figure 4.3**.

Table 4.1: *Legend to the hydrogen absorption profile* ***(Figure 4.3)***

Legend	Sample size and heat treatment
5HX-3_1*18	1mm x 18mm (L x D) hydrogenated in 5 vol.% H, at temp. X for 3 hrs
15HX-3_1*18	1mm x 18mm (L x D) hydrogenated in 15 vol.% H, at temp. X for 3 hrs
15HX-8_1*18	1mm x 18mm (L x D) hydrogenated in 15 vol.% H, at temp. X for 8 hrs
15HX-3_10*12	12mm x 10mm (L x D) hydrogenated in 15 vol.% H, at temp. X for 3 hrs
15HX-8_10*12	12mm x 10mm (L x D) hydrogenated in 15 vol.% H, at temp. X for 8 hrs
15HX-3_12*18	12mm x 18mm (L x D) hydrogenated in 15 vol.% H, at temp. X for 3 hrs
15HX-8_12*18	12mm x 18mm (L x D) hydrogenated in 15 vol.% H, at temp. X for 8 hrs

temp. – temperature **hrs** - hours

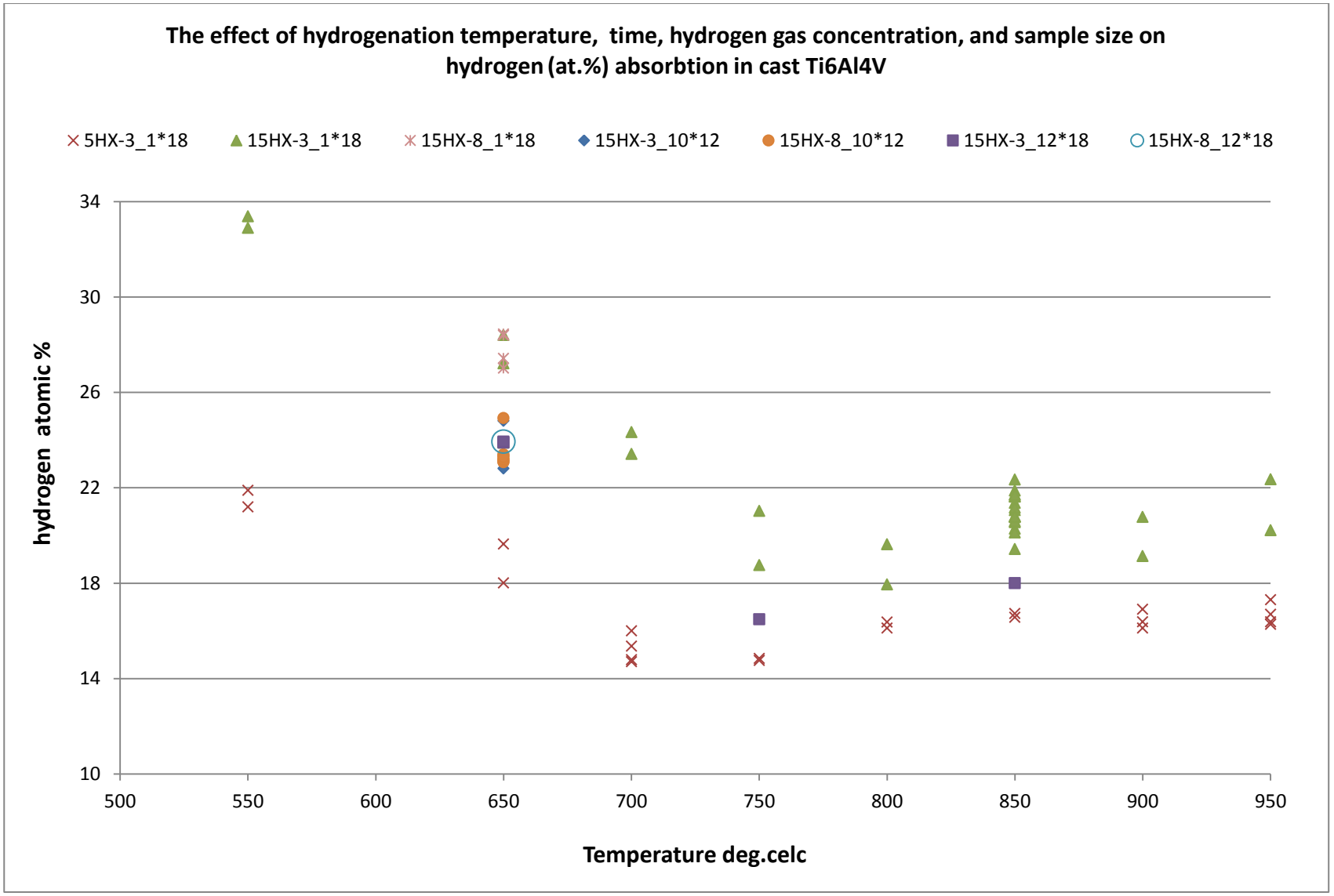

Figure 4.3: *The effect of hydrogenation temperature, time and sample size on hydrogen absorption.*

In **Figure 4.3**, the relative hydrogen absorption trend is similar for all specimen sizes. However, a greater amount of hydrogen is absorbed at lower hydrogenation temperatures. For example, the 1mm x 18mm diameter samples hydrogenated at 550°C for 3 hours using 15 vol.% H gas concentration absorbed the highest amount of hydrogen (33±3 at.% H).

Hydrogen absorption increases with an increase in hydrogen gas concentration. The specimens hydrogenated in 5 vol.% H had the least amount of absorption at all investigated temperatures. However, at temperatures above 800°C, hydrogen absorption for 5 vol.% H and 15 vol.% H specimens is similar. This may be due to increasing surface oxide formation at these temperatures, which hinders hydrogen absorption. This means that mass measurements become an unreliable measure of absorbed hydrogen above 800°C. Alternatively it may be argued that the lower solubility of hydrogen at higher temperatures decreases the sensitivity to the hydrogen atmosphere.

The investigated sample sizes show no significant change in hydrogen absorption with increasing sample size. This is seen at 650°C where 1mm x 18mm samples absorbed 27±3 at.% H. In comparison, 10mm x 12mm and 12mm x 18mm samples absorbed 24±3 at.% H respectively.

There is no change in hydrogen absorption with increasing hydrogenation time from 3 to 8 hours. This is seen at 650°C where the hydrogen absorption for 15HX-3_1*18, 15HX-3_10*12 and 15HX-3_12*18 is similar to 15HX-8_1*18, 15HX-8_10*12 and 15HX-8_12*18 respectively.

In summary, the hydrogen / Argon atmosphere and soak temperature have a much greater influence on hydrogen absorption than sample size and soak time for the investigated conditions in this study.

Figure 4.4 shows the hydrogen content of 16 samples (samples 1-16) that were hydrogenated at varying temperatures and vol.% H atmosphere. These are superimposed on a phase diagram obtained from Qazi et al.`s[35, 44, 45] TEM analysis of hydrogenated Ti6Al4V. The phase diagram was included to compare with published results; it is not necessarily the accepted phase diagram.

In **Figure 4.4**:

- The green lines delineate the various phase regions for hydrogenated Ti6Al4V. [35]
- The blue markers represent samples 1-8 which were hydrogenated in a 5 vol.% hydrogen atmosphere.
- The red markers represent samples 9-16 which were hydrogenated in a 15 vol.% hydrogen atmosphere.

In **Figure 4.4**, the phase diagram (green lines) shows that:

- Alloying with 30 at.% hydrogen decreases the beta transus from 1000°C to 800°C.
- No hydrides form below 13 at.% hydrogen.
- An alpha (α), beta (β) and hydride (δ) region exists below the transus temperature at 13-30 at.% hydrogen.
- A beta (β) and hydride (δ) region exists above the beta transus up to 900°C at hydrogen concentrations between 13-30 at.% hydrogen.

The phases that form when alloying Ti6Al4V with up to 30 at.% H were examined by Qazi et al. [35, 44, 45] through TEM. The phase diagram in Qazi et al. [35] acts as a benchmark of the expected phases in hydrogenated Ti6Al4V. In the present work, XRD was used to analyse the phase composition of hydrogenated samples 1-16 and the results are shown in **Figure 4.6**.

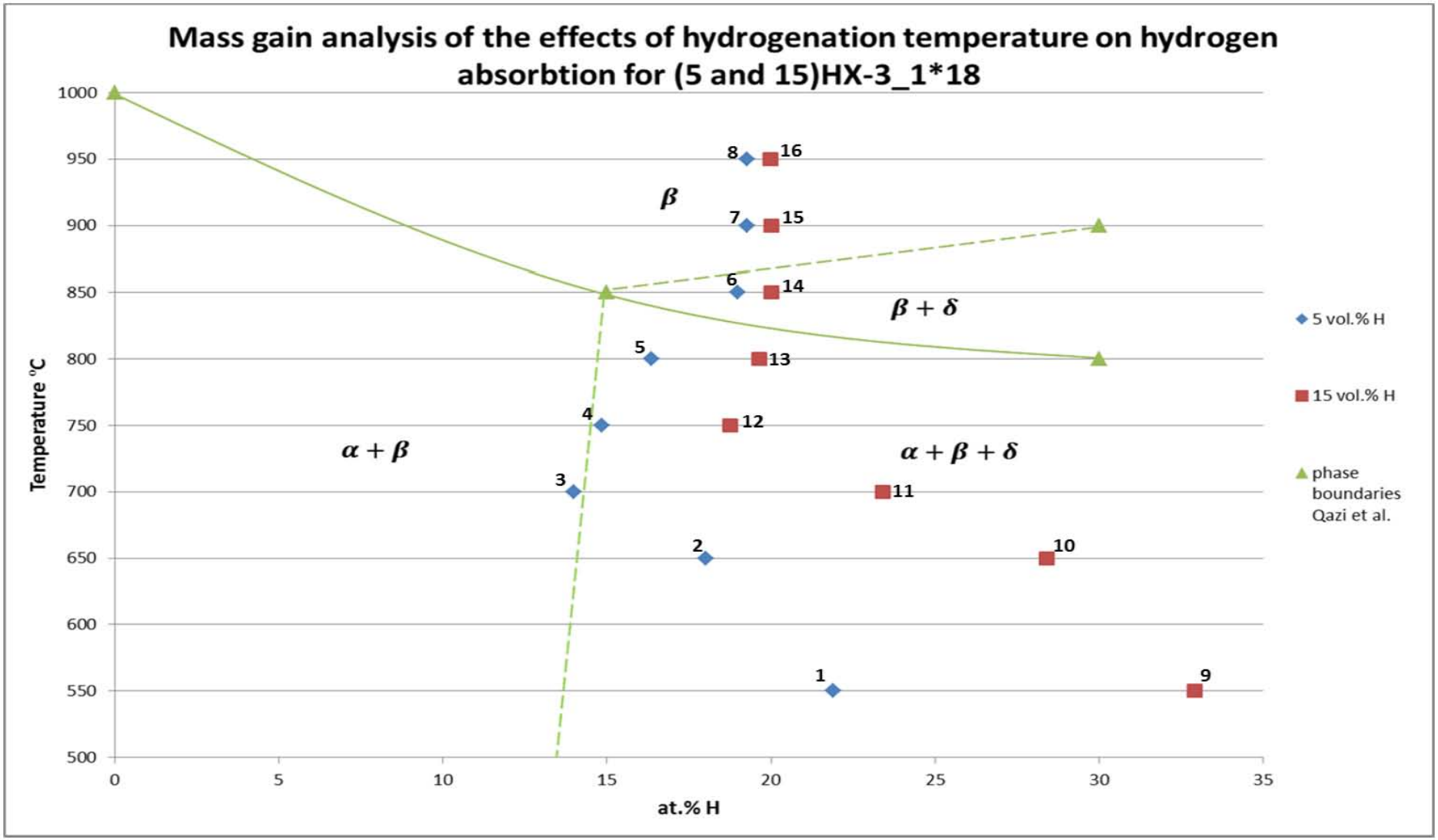

Figure 4.4: *The hydrogen content of samples 1-16 superimposed on a phase diagram (green lines) obtained from Qazi et al.* [35] *Blue and red markers show samples 1-8 and 9-16 respectively.*

4.3.2 Phase composition of hydrogenated Ti6Al4V

The interpretation of XRD data in hydrogenated Ti6Al4V is made difficult by the several peak overlaps that occur for the alpha, beta, alpha` (martensite) and hydride phases. This fact is illustrated in **Figure 4.5**, where the markers represent the 2 Theta peak positions of the abovementioned phases as obtained from the literature.[41, 44]

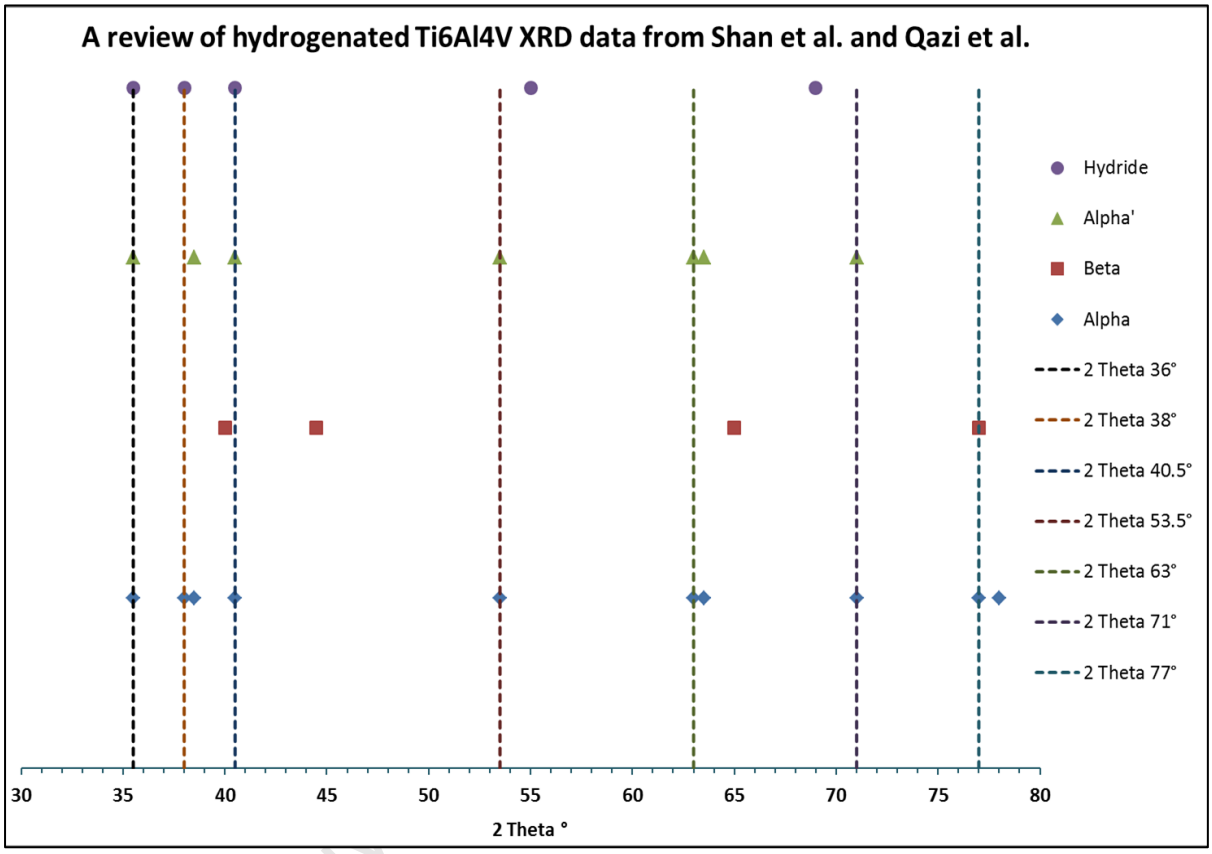

Figure 4.5: *A review of hydrogenated Ti6Al4V XRD data showing 2 Theta peak positions of the alpha, alpha` (martensite) beta and hydride phases. The dotted lines highlight the peak overlaps which cause difficulties in identifying the individual phases that form in hydrogenated Ti6Al4V.*[41, 44]

Nevertheless, there are factors associated with hydrogenation that promote peak broadening and reduction in diffraction intensities. These alterations in the XRD traces can be associated with the various levels of hydrogenation.

The XRD analysis of samples 1-16 in **Figure 4.4** is shown by the corresponding XRD traces 1-16 in **Figure 4.6**. In **Figure 4.6**, trace (0) is as cast (non-hydrogenated) Ti6Al4V and traces 1-16 are hydrogenated Ti6Al4V samples. The hydrogenation conditions are shown in the legend in **Figure 4.6**.

In **Figure 4.6**, trace (0) (non-hydrogenated Ti6Al4V) shows dominant peaks at 2 theta 36°, 38°, 39°, 41°, 53°, 77° and 78° which are alpha and beta phases. When comparing as cast Ti6Al4V trace (0) to hydrogenated Ti6Al4V (traces 1-16) varying degrees of relative peak widening are evident especially on traces 1-3 and 9-13 at 2 Theta 35°, 38° and 41°. This intensity of peak widening is lower in traces 4-8 when compared to 14-16. This suggests that there was a lower solution of hydrogen at higher hydrogenation temperatures and at 5 vol.% H which supports the findings in **Figure 4.4**. In the case of XRD traces 1,3,9 and 10 there is also a significant reduction in overall diffraction intensity.

Peak broadening and reduction in intensity can be influenced by several factors including strain (lattice distortion), crystallite size and the presence of an amorphous layer. All three of these factors can in some way be related to increasing levels of hydrogen in the alloy.

In the first instance, hydrogen dissolved in solid solution will distort the titanium lattice particularly in the alpha phase. In the case of the alpha phase, this is more prominent at lower hydrogenaion temperatures where more hydrogen is absorbed. Secondly, the formation of sub-micron hydride phases will cause peak broadening in view of the general reciprocal relationship between peak width and crystallite size. This becomes more particular as the crystallite size falls below 1μm diameter. Lastly, it has been noted that during metallographic specimen preparation, considerable smearing can occur during grinding and polishing when fine crystallites are present. This disturbance of the near surface introduces an acute armophous nature which influences the diffraction intensity. In summary, whilst it is difficult to obtain quantitative information from XRD data with respect to levels of hydrogenation, the indicators are consistent with the data presentation in **Figure 4.4**. The microstructures of samples 1-16 are discussed in **Section 4.3.3**.

Legend

Hydr. Temp °C	550	650	700	750	800	850	900	950
5 vol.% H	1	2	3	4	5	6	7	8
15 vol.% H	9	10	11	12	13	14	15	16

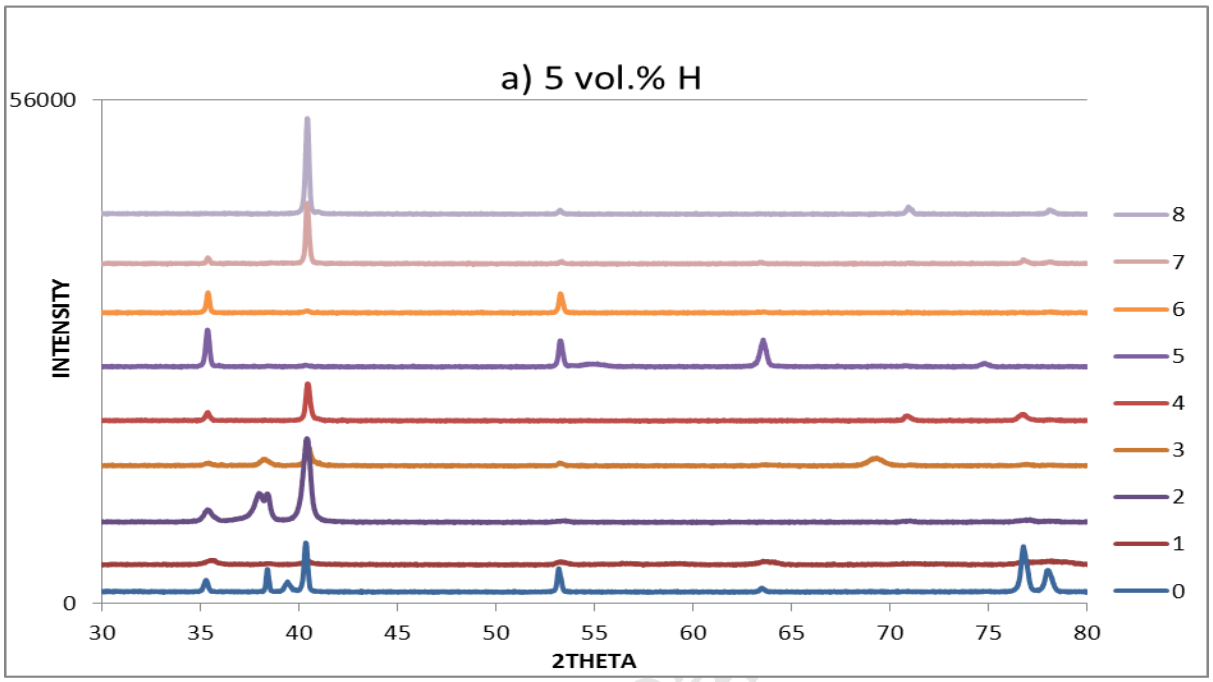

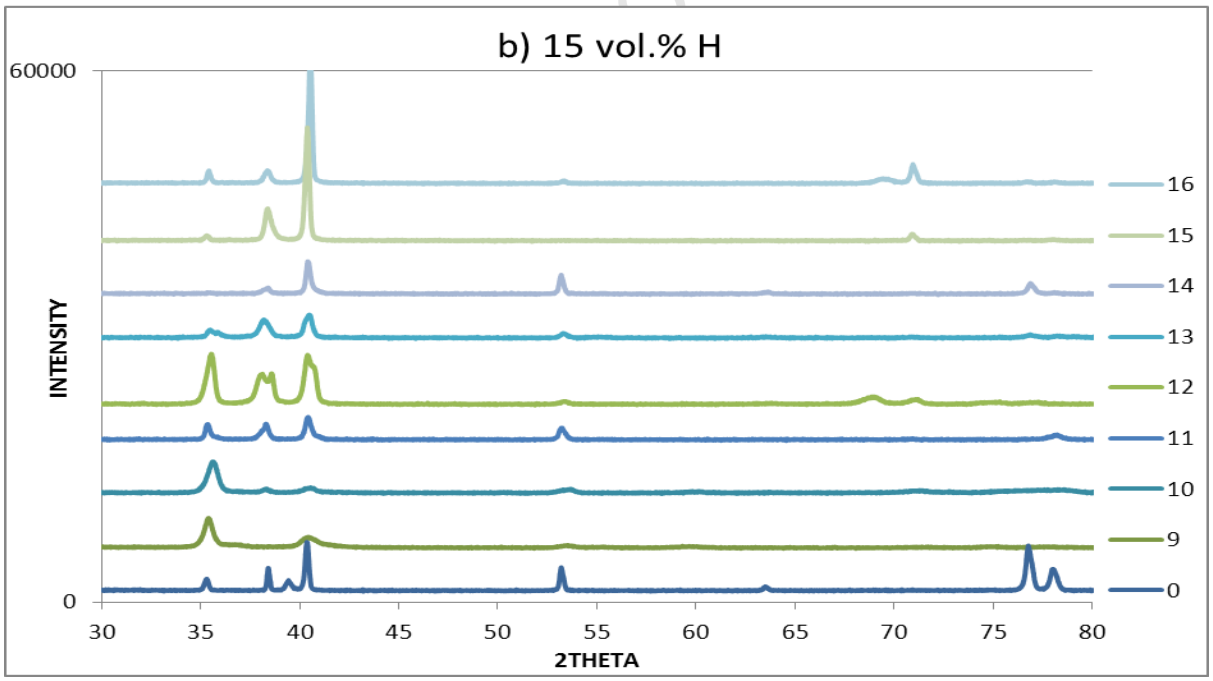

Figure 4.6: *XRD analysis of samples 1-16 hydrogenated in a) 5 vol.% H or b) 15 vol.% H at a temperature range of 550°C-950°C (see legend). Their hydrogen content and microstructures are shown in* ***Figures 4.4, 4.7*** *and* ***4.8*** *respectively.*

4.3.3 Microstructure analysis of hydrogenated Ti6Al4V

Figures 4.7-4.8 show the microstructures of samples 1-16, these have martensite needle, Widmanstätten alpha, discontinuous alpha and feathery morphologies.

The needle morphology is shown in **Figures 4.7-4.8** for samples 11-16. This was observed on samples hydrogenated using 15 vol.% H at hydrogenation temperatures above 700°C. Hydrogen reduced the critical cooling rate for martensite formation. This is because martensite needles formed at slow furnace cooling rates of 5°C/min. No needle martensite formed at the 5 vol.% H condition. This shows that microstructures 13-16 have a greater amount of hydrogen when compared to 5-8.

This contradicts **Figure 4.4** which shows the hydrogen absorption analysis determined by mass gain measurements. In **Figure 4.4**, there is no significant difference in the hydrogen content of the 5 vol.% H and 15 vol.% H conditions at hydrogenation temperatures above 800°C. Therefore, this highlights that mass gain measurements become an unreliable measure of absorbed hydrogen at higher hydrogenating temperatures. However, similar work in [32, 48] shows that a minimum of 15 at.% H is absorbed by samples hydrogenated in 15 vol. % H above 650°C. This is consistent with the results in **Figures 2.12, 4.3** and **4.4** where all samples hydrogenated in 15 vol.% H absorbed at least 15 at.%H at hydrogenating temperatures above 650°C. The consistency in these results shows that although mass measurents may be unreliable at higher hydrogenating temperatures, but at least 15 at.% H is absorbed in 15 wt.%H at hydrogenating temperatures above 650°C.

Discontinuous alpha lamellae are shown in **Figures 4.7-4.8** samples 5-8. They result from Widmanstätten growth when hydrogen saturated beta transforms to hydrogen saturated alpha during cooling. The feathery morphology is shown in **Figure 4.8** samples 1-2 and 9-10. It has light "feathery" regions in a contrastingly darker matrix. This morphology is associated with high hydrogen and hydride content. In Matthews and Knutsen,[32] the feathery morphology in Ti6Al4V was associated with increased levels of hydrogen embrittlement.

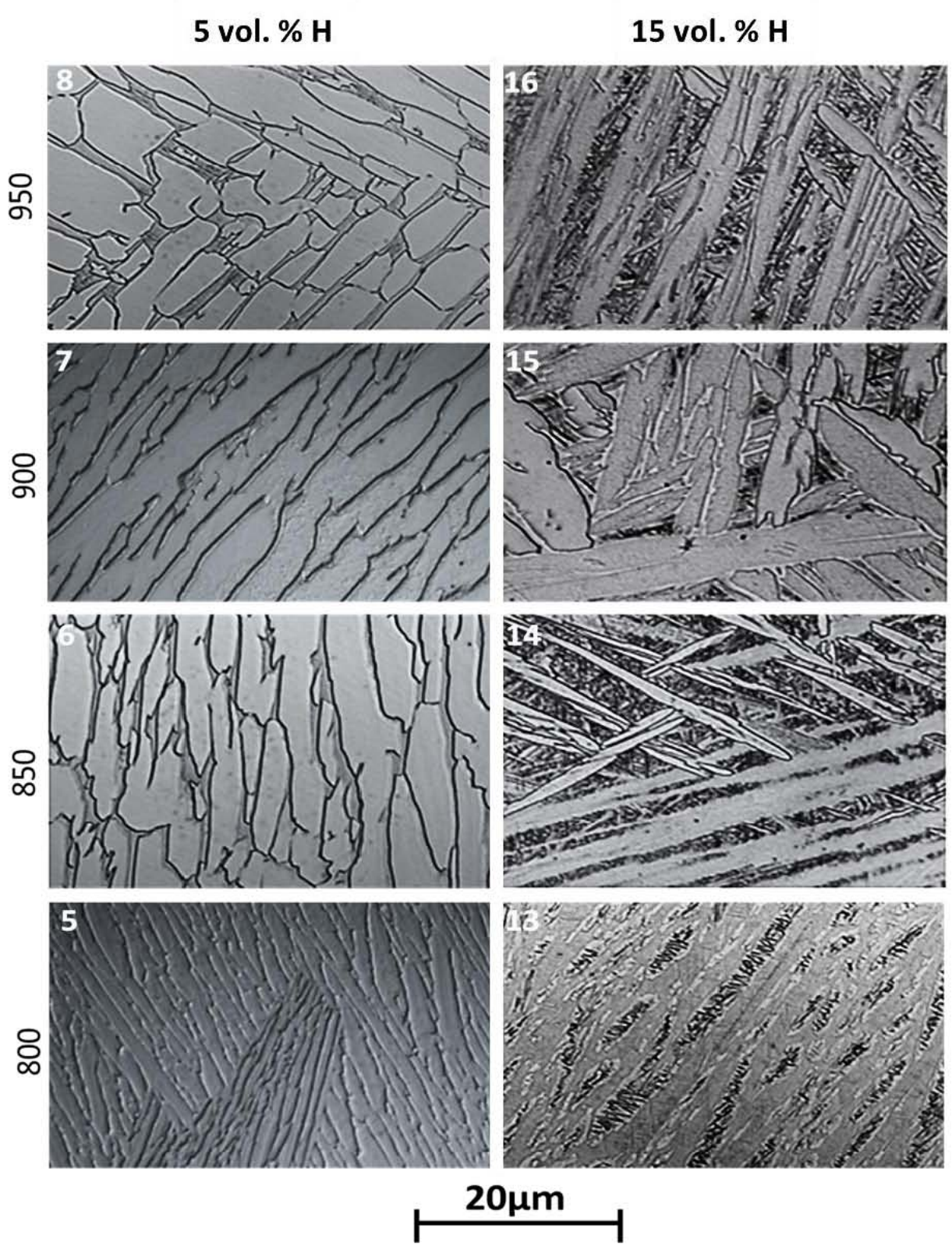

Figure 4.7: *Optical images of samples (5-8) and (13-16) showing 5 vol.%H and 15 vol.%H conditions at hydrogenation temperatures 800°C-950°C* ***(see Figures 4.4*** *and* ***4.6)****.*

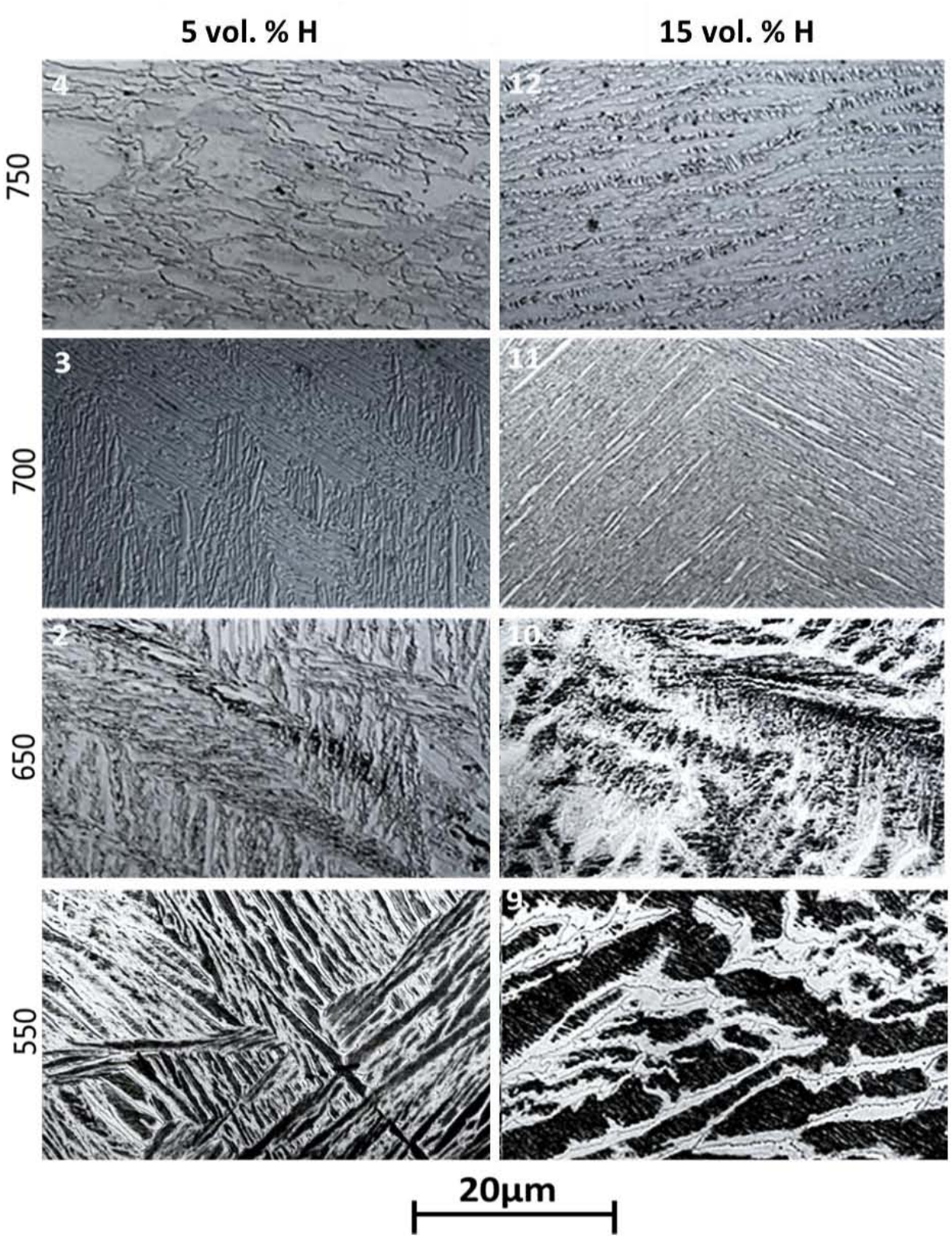

Figure 4.8: *Optical images of samples (1-4) and (9-12) showing 5 vol.% H and 15 vol.% H conditions at hydrogenation temperatures 550°C-750°C* ***(see Figures 4.4*** *and* ***4.6)****.*

In the present work, the brittle nature of the feathery morphology was manifested by the cracking of all samples hydrogenated at 550ºC (samples 1 and 9). In **Figure 4.9**, the images of samples 1 and 9 show increasing levels of hydride related cracking with increasing hydrogen atmosphere concentration from 5 vol.%H to 15 vol.% H.

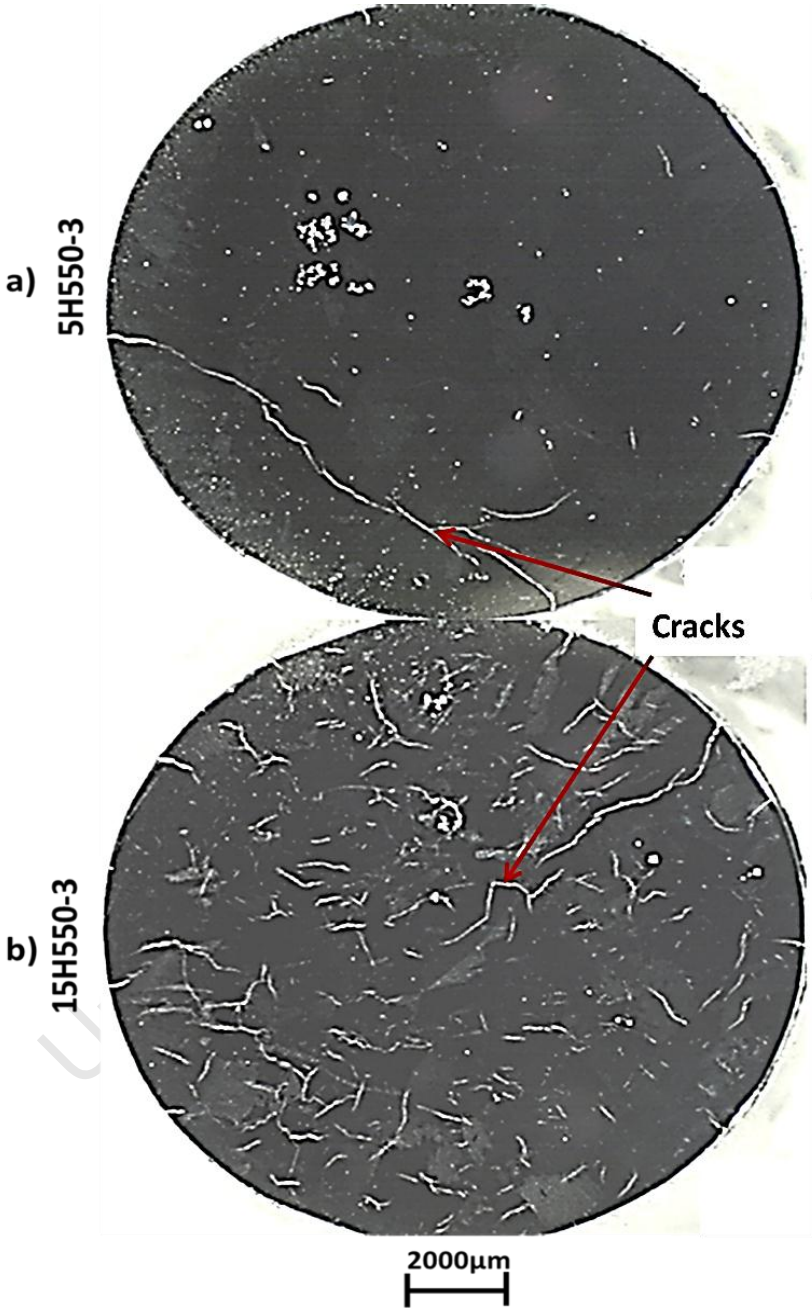

Figure 4.9: *A stereomicrograph of a polished sample surface showing hydride related cracking. Samples a)-b) were hydrogenated at 550ºC in a) 5 vol.% H and b) 15 vol.% H atmosphere. More cracks are seen on the 15 vol.% H sample (b) which absorbed a higher amount of hydrogen* ***(see Figure 4.4)****.*

4.3.4 Effect of hydrogen absorption on hardness

In **Figures 4.10 a)**, **b)** samples 1-16 were hydrogenated at various temperatures and furnace cooled at 5°C/min as previously described. A minimum of 30 hardness measurements at 10kgf were taken from each sample condition (1-16). The indents were made on a polished sample surface and they were spaced 1mm apart. Their hardness values are compared to as cast and wrought Ti6Al4V. The box and whisker plots show the distribution of the hardness data. The interquartile range (IQR) is the 3rd quartile minus the 1st quartile. Outliers are hardness values that are more than one and a half times the IQR (1.5 X IQR), either above the 3rd quartile or below the 1st quartile respectively.

In **Figure 4.10** the average hardness of as cast and wrought Ti6Al4V is 340HV and 350HV respectively. It was expected that hydrogenation would increase the hardness due to hydrogen solution strengthening or formation of hydrides. The absorbed hydrogen occupies interstitial sites of alpha and beta. Hydrogen stabilises more beta at lower temperatures and beta absorbs more hydrogen than alpha. Therefore increasing hydrogen absorption should increase hardness.

However, **Figure 4.10** shows that there is no significant relationship between hydrogenation temperature and hardness. Minor hardness peaks occur at 550°C for both a) 5 vol.% H and b) 15 vol.% H conditions. These minor hardness peaks indicate that a large volume fraction of hydrides precipitate at this temperature. Precipitation of hydrides causes a volume misfit of 8-11% in beta and 0-5% in alpha. [40] This volume misfit distorts the lattice causing strain fields which are accommodated plastically by formation of dislocations around the hydrides. This increase in dislocations results in an increase in hardness. In **Figure 4.10 b)**, hardness plateaus above hydrogenation temperature 800°C. This indicates that softer martensite phase was forming. Hydrogen lowered the critical cooling rate for martensite formation and martensite formed at furnace cooling rates of 5°C/min. [35] The hardness plateau is less significant in **Figure 4.10 a)** for the 5 vol.% H condition and **Figure 4.7** shows that no needle martensite was observed in the 5 vol.% H treated samples.

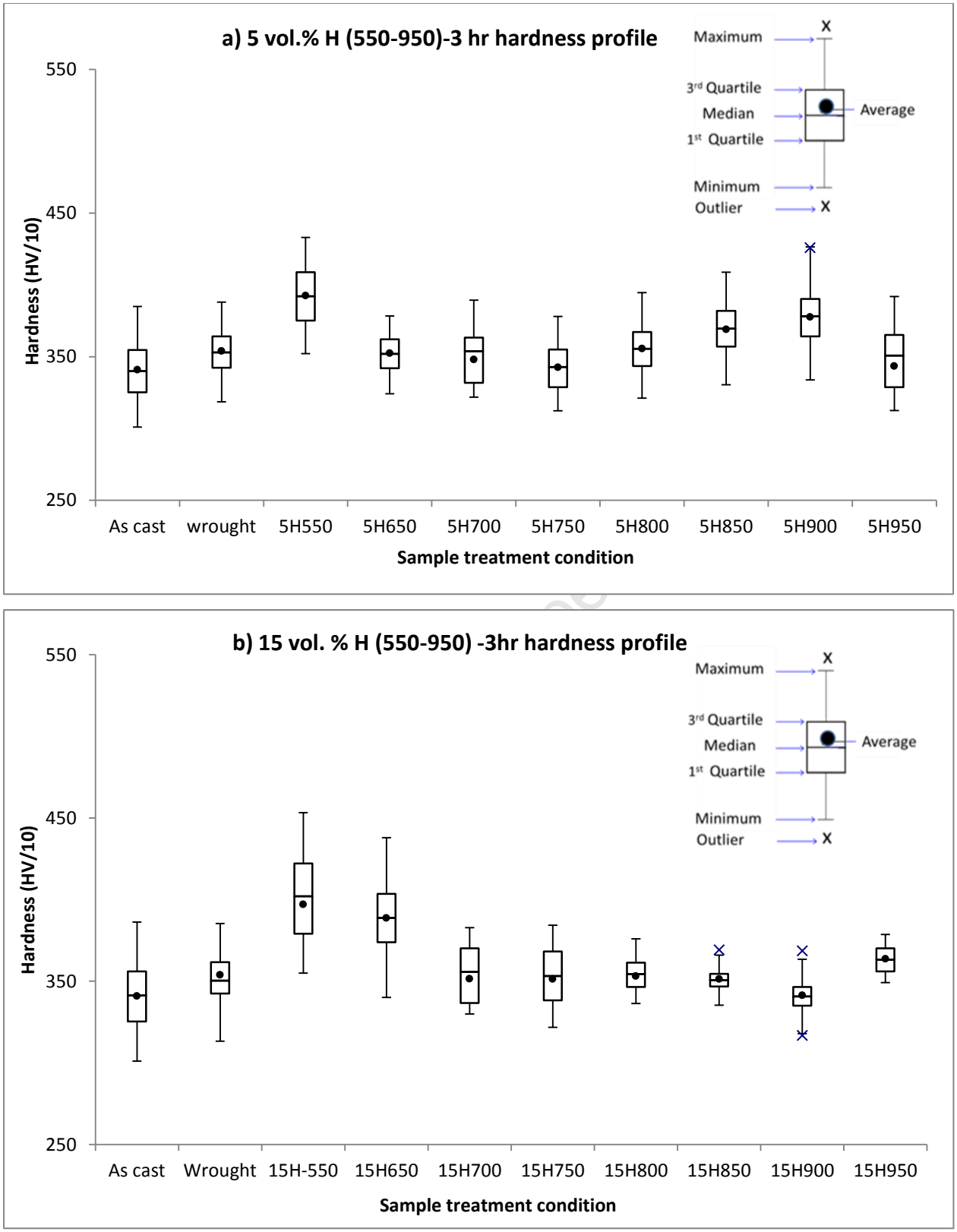

Figure 4.10: *Macrohardness data for samples 1-16 which were hydrogenated and furnace cooled in a) 5 vol.% H and b) 15 vol.% H at temperatures 550°C-950°C.*

In summary, **Figure 4.10** shows that the hydrogenation procedures considered in the present work do not significantly alter the hardness relative to the as cast condition. This may be caused by the competing effects of hydrogen solution, hydride formation and increased tendency for martensite formation. However, minor hardness peaks for the 550ºC treatment emphasize the substantial hydride formation and the hydrogen solid solution (α_H) at this temperature. The effect of hydride formation on hardness is further highlighted in **Section 4.4** where beta decomposes to form alpha and hydrides.

4.4 Effect of beta decomposition (THP-BD) on refinement

4.4.1 Effect of beta decomposition on microstructure and hardness

The results in **Figures 4.11-4.12** were obtained from 1mm x 18mm diameter samples hydrogenated to 20±3 at.% H at 850ºC for 3 hours. These were solution treated at 900ºC for an hour. After solution treatment, the microstructures in **Figures 4.12 A1)-A2)** were quenched and **Figures 4.12 B1)-B2)** were furnace cooled.

From the solution temperature, **Figures 4.12 C)-E)** were cooled at 5ºC/min to the isothermal hold temperatures of 700ºC (C1-C4), 600ºC (D1-D4) and 500ºC (E1-E4). These samples were isothermally held for up to 30 hours followed by water quenching for hardness testing.

The control study was performed at similar conditions to **Figure 4.12 D)** using as cast (non-hydrogenated) Ti6Al4V samples as starting material. As cast samples were subjected to a thermal cycle equivalent to (D1-D4) in order to assess the influence of hydrogen. **Figures 4.12 C1-C2** and **C3-C4** were isothermally annealed for 1 hour or 3 hours respectively, this also applies to **Figures 4.12 D1-D4** and **E1-E4**.

All samples were coated in isomol to prevent oxidation and the possible escape of hydrogen at high annealing temperatures **(see Figure 3.2)**.

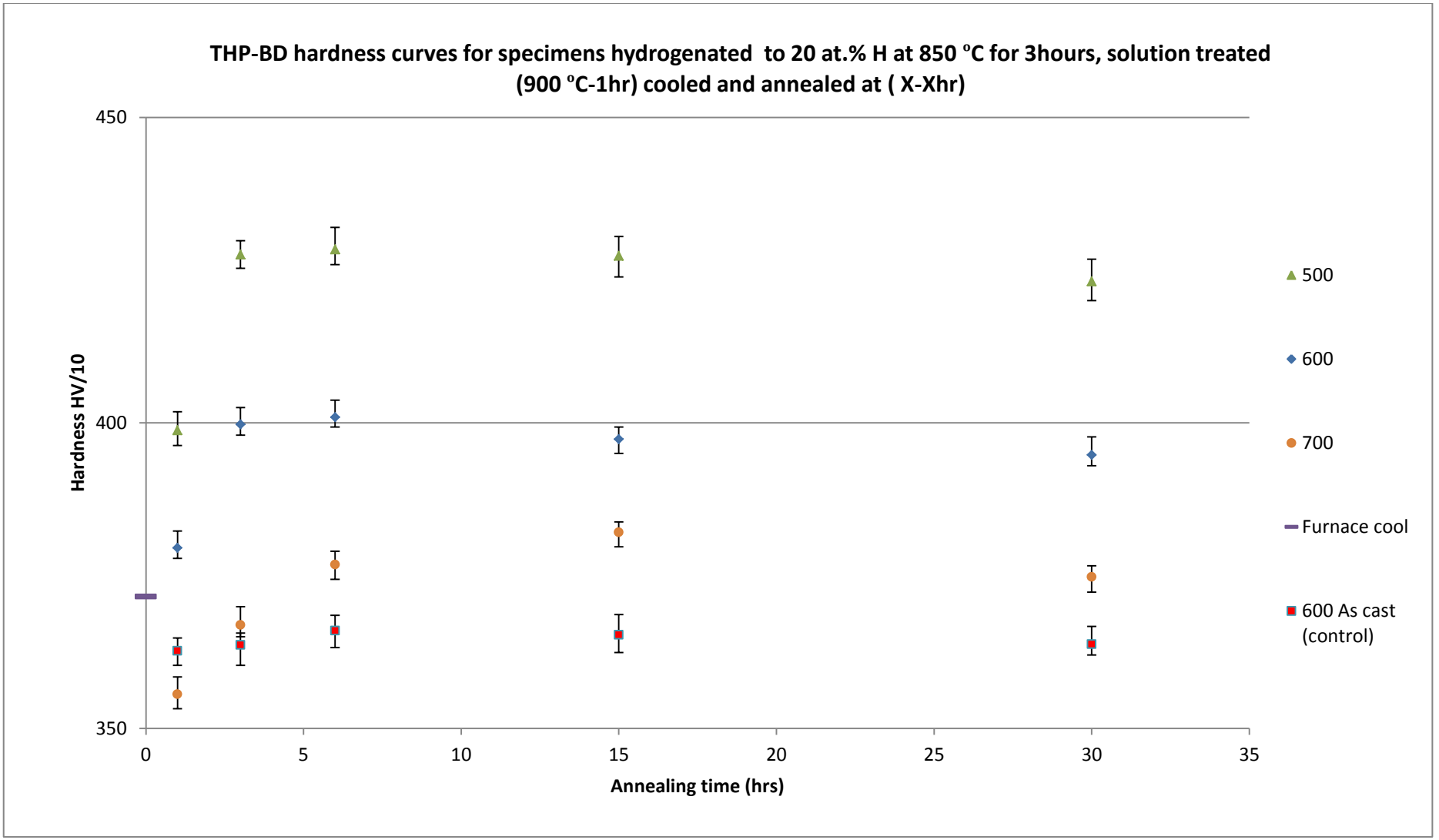

Figure 4.11: *The beta decomposition of softer beta phase to harder alpha and hydride phases. The start of the hardness plateau represents the completion of the beta decomposition.*

In **Figure 4.11**, hardness increases to peak hardness and plateaus. The decomposition of softer beta phase to form harder alpha and hydride phases causes this hardness increase. In **Figure 4.10 b)**, the average hardness of samples hydrogenated in 15 vol.% H at 850ºC for 3 hours is 350HV. The average hardness increased by approximately 80HV (from 350HV) after solution treating and isothermally annealing at 500ºC for 3 hours. This was the largest hardness increase as shown in **Figure 4.11**. The samples isothermally annealed at 700ºC and 600ºC had approximate average increases of 30HV and 50HV (from 350HV) respectively. Samples annealed at 500ºC and 600ºC reached peak hardness after 3 hours of isothermal annealing. On the contrary, samples annealed at 700ºC reached peak hardness after 6 hours of isothermal anneal. Peak hardness depicts the completion of the beta to alpha and hydride decomposition.[44]

The control experiment is non-hydrogenated Ti6Al4V beta decomposed at 600ºC. It shows a 20HV hardness increase from 340HV (cast Ti6Al4V hardness) to 360HV. This is an insignificant hardness increase when compared to the hydrogenated condition beta decomposed at a similar temperature (600ºC). Beta decomposition at 600ºC resulted in finer Widmanstätten lamellae which slightly increased the hardness. This shows that the greatest hardness increase is due to hydrogen solution and the formation of hydrides.

The hardness values of hydrogenated specimens are lowest at 700ºC. This is because beta was more stable at 700ºC and therefore less beta decomposed to the harder hydride phase. The Temperature Time Transformation (TTT) diagram in **Figure 3.3** shows that the nose temperature for beta decomposition is 600ºC. Beta is least stable at annealing temperatures between 500ºC and 600ºC when compared to 700ºC. Therefore, more beta decomposition is expected to occur at 500ºC and 600ºC than at 700ºC.

The corresponding microstructures are shown in **Figures 4.12 A-E)** and their EBSD phase analysis is shown in **Figures 4.13-4.15**. In **Figures 4.12 A-E**, images **A2, B2, C2, C4, D2, D4, E2** and **E4** are high magnification images of **A1, B1, C1, C3, D1, D3, E1,** and **E3** respectively.

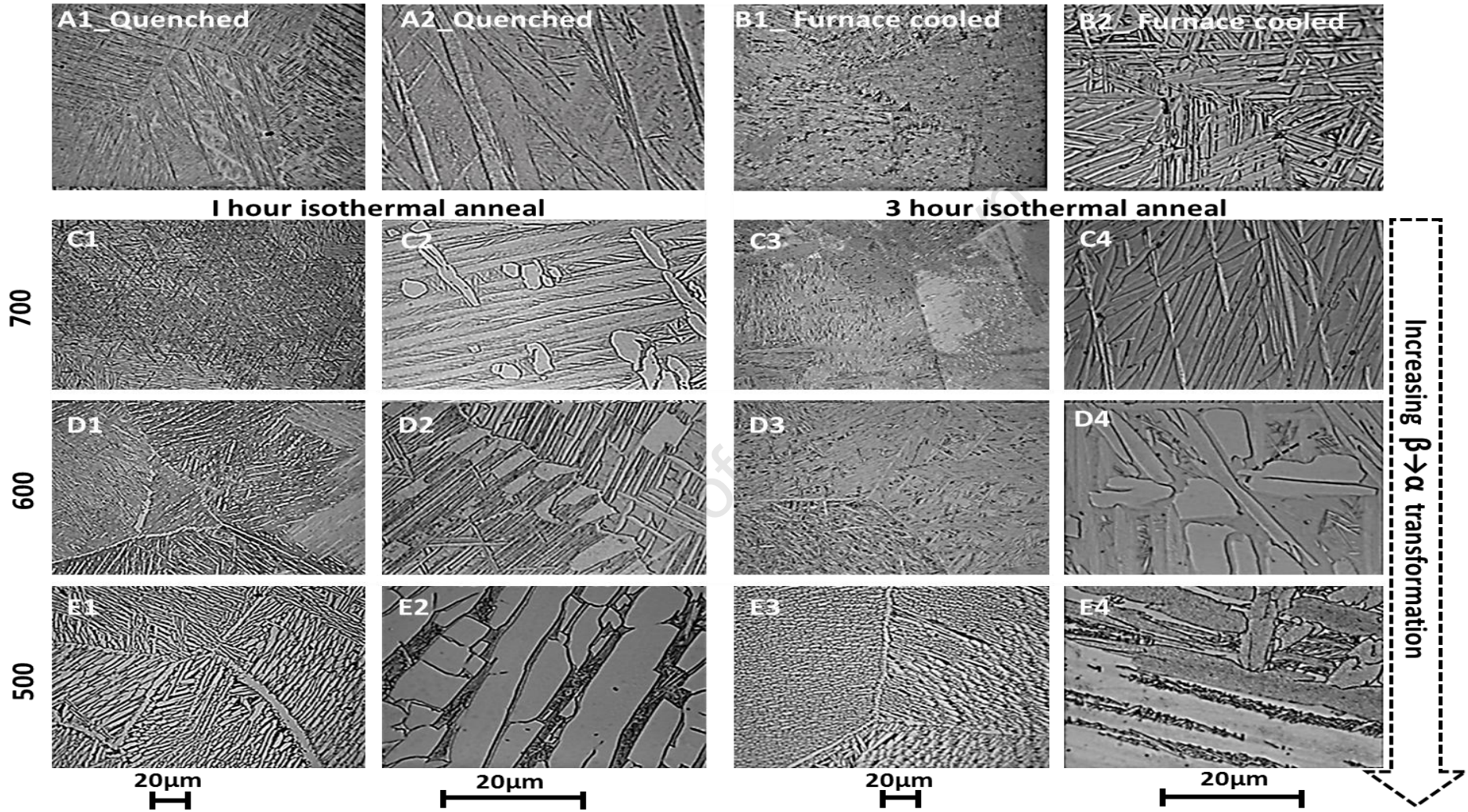

Figure 4.12: *Optical images showing microstructure evolution during beta decomposition at 700ºC (C1-C4), 600ºC (D1-D4) and 500 ºC (E1-E4). Conditions D-E have the highest hardness increase between 1-3 hours of isothermal anneal, which is not seen at condition C. Conditions A1-A2 and B1-B2 were quenched and furnace cooled from solution temperature (900ºC) respectively.*

Figures 4.13-4.15 show the corresponding EBSD images of the microstructures in **Figure 4.12**.

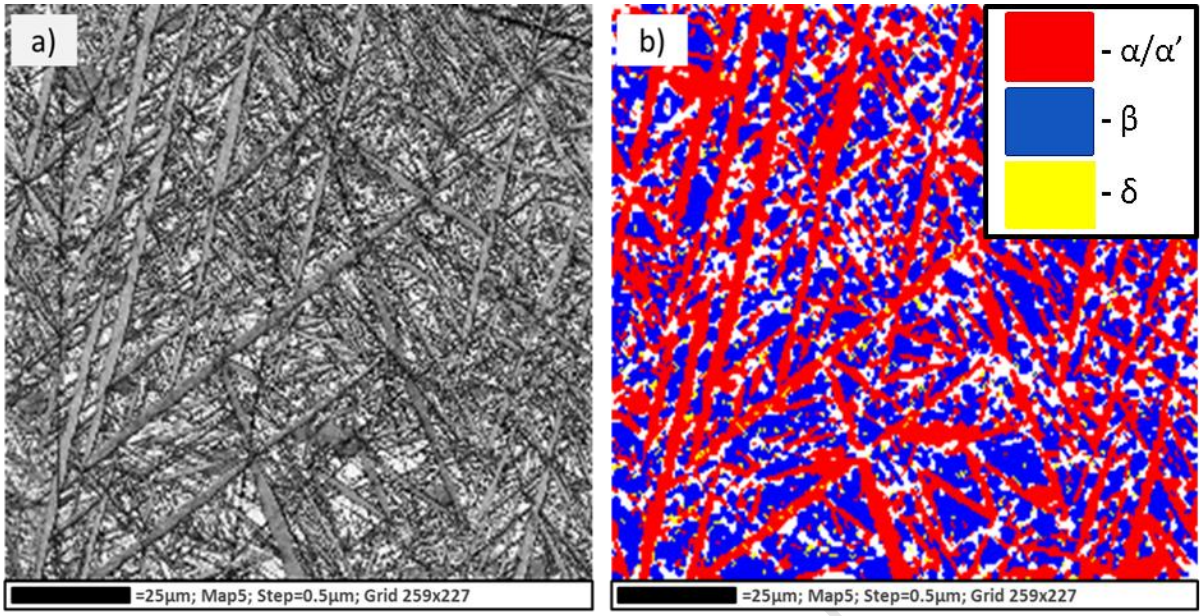

Figure 4.13: *a) band contrast and b) phase maps of a hydrogenated, solution treated and quenched sample. In image b), red is hcp (α/ά), blue is bcc, yellow is hydride and non-indexed regions are white. The quenched microstructure has needle hcp morphology and retained metastable bcc (beta) phase.*

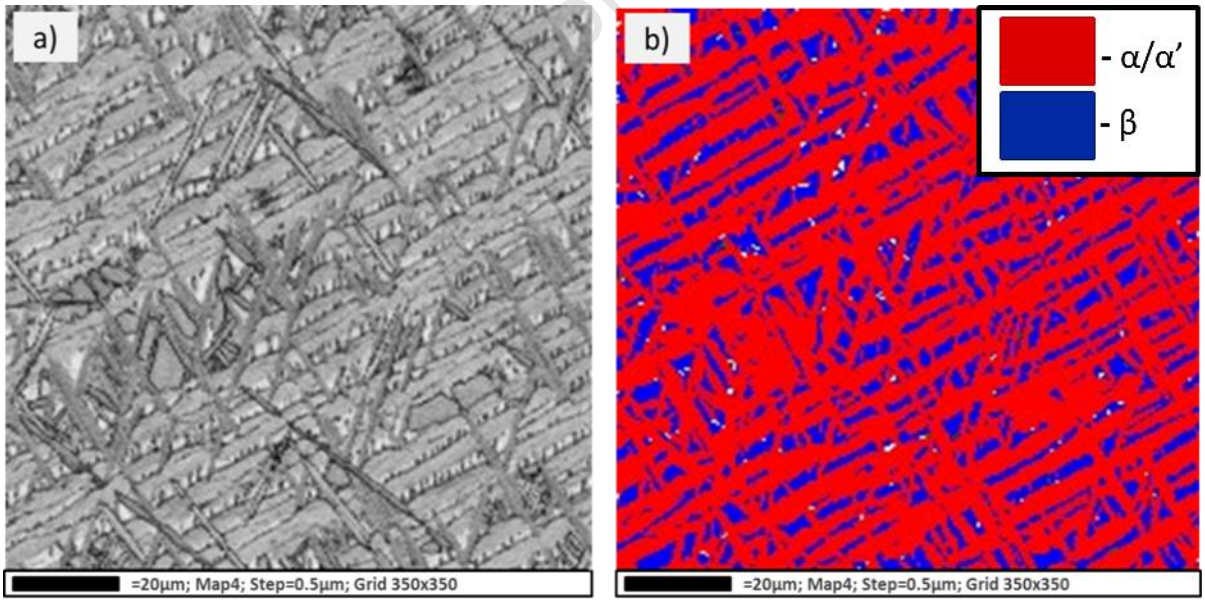

Figure 4.14: *a) band contrast and b) phase maps of a hydrogenated, solution treated and furnace cooled sample. In image b), red is hcp (α/ά), blue is bcc phase and non-indexed regions are white. The furnace cooled microstructure has needle and lamellar hcp phase. It also shows less bcc phase when compared to the quenched microstructure.*

Figures 4.13 a), b) show that the solution treated and quenched microstructures in **Figures 4.12 A1-A2** have needle hcp morphology and retained bcc phase. This means that beta transformed to hexagonal martensite, but hydrogen stabilised some of the beta phase as retained metastable beta. Authors [49, 50] have reported on the coexistence of beta and hexagonal martensite on quenched titanium alloys that have a high amount of beta stabilizing elements.

The furnace cooled microstructures in **Figures 4.14 a), b)** show the microstructures in **Figures 4.12 B1-B2.** They have needle and lamellar hcp and less bcc phase when compared to **Figure 4.13 a), b)**. This could be hcp alpha or hcp martensite phase. Furnace cooling at 5ºC/min causes a Widmanstätten beta (bcc) to coarse acicular alpha (hcp) transformation. However, the alloyed 20±3 at.% H can also cause a beta to martensite transformation at slow furnace cooling rates of 5ºC/min. [35]

Figure 4.15 is an EBSD phase analysis of samples hydrogenated, solution treated and beta decomposed at 700ºC (a-b), 600ºC (c-d) and 500ºC (e-f) for 6 hours. In **Figure 4.15**, the band contrast maps show that beta decomposed samples have acicular (a, c) and discontinuous (e) morphologies. Discontinuous hcp (alpha) lamellae formed during a Widmanstätten saturated beta to saturated alpha transformation.

Figures 4.15 a), b) show that samples beta decomposed and quenched at 700ºC have hcp and bcc phases and no indexed hydride phase. No hydrides were indexed at 700ºC because beta was most stable at 700ºC. Beta can dissolve up to 40 at.% H [40] thus it prevents the precipitation of hydrides. Decreasing the decomposition temperature to 600ºC or 500ºC transformed more beta to alpha phase **(Figures 4.15 c-f)**. Alpha dissolves only 8 at.% H [40] and this leads to non-dissolved hydrogen forming hydrogen rich regions that transform to hydrides [39] **(Figures 4.15 d, f)**. Therefore, this proves that the formation of hydrides was responsible for increasing the hardness of hydrogenated specimens in **Figure 4.11**.

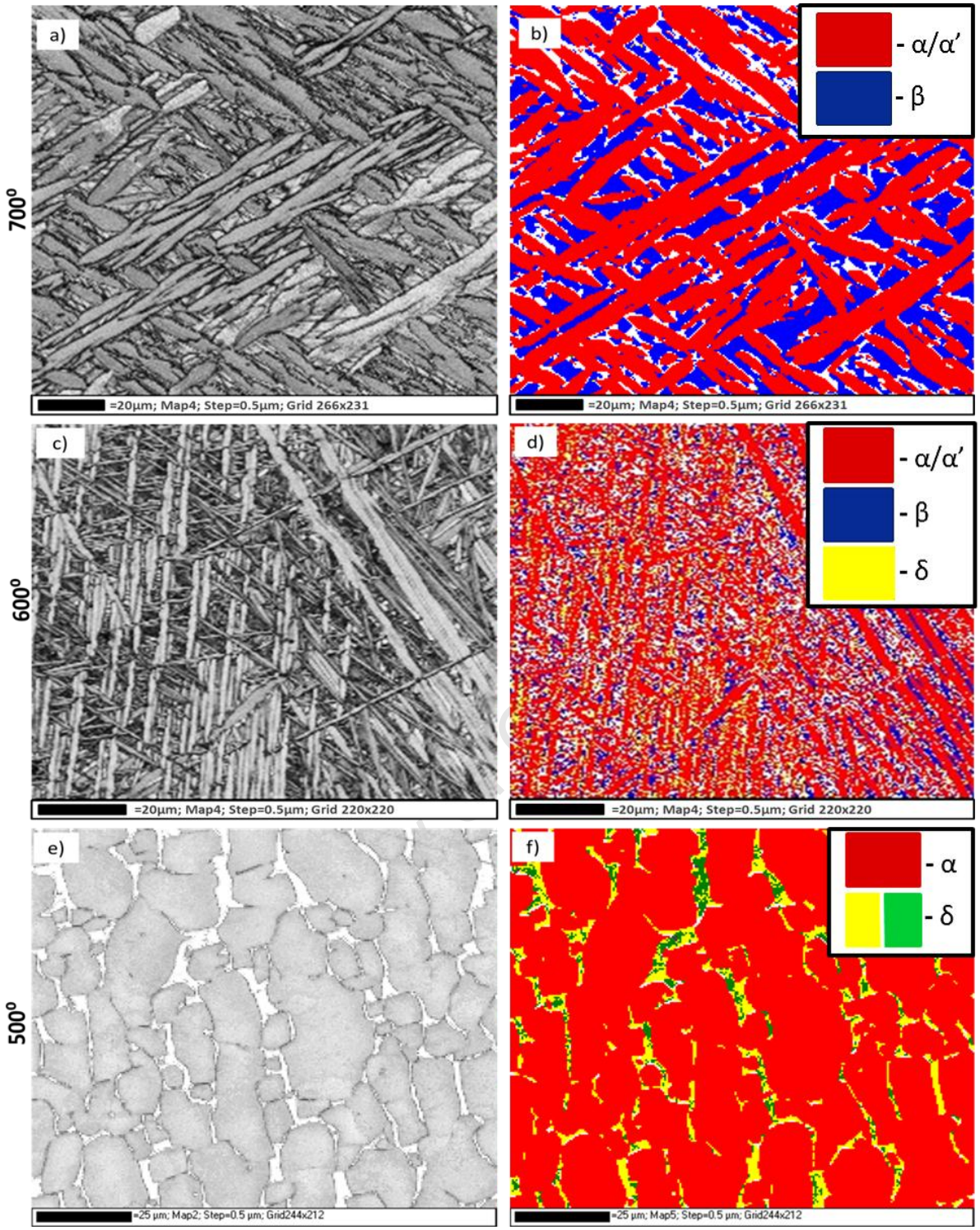

Figure 4.15: *Shows band contrast a), c), e) and phase maps b), d), f) of samples beta decomposed at 700°C (a-b), 600°C (c-d) and 500°C (e-f) respectively. In b), d), f), red is hcp (α/ά) blue is bcc, yellow and green are hydrides. Non-indexed regions are white.*

4.4.2 Beta transformations in hydrogenated titanium

In **Figure 4.13**, quenching from 900°C caused a bcc to needle hcp transformation. Hydrogen stabilised [49, 50] some of the high temperature bcc phase during quenching. This resulted in a needle hexagonal martensite structure in a retained metastable beta matrix. A similar situation arose during slow cooling except that increased hcp phase is present.

The phase transformations that occurred during isothermal beta decomposition and subsequent quenching are:

i. $\beta_H \rightarrow \alpha_H$ (Cooling below beta transus).

ii. $\beta_H \rightarrow \alpha + \delta$ (At eutectoid temperature).

iii. $\beta \rightarrow martensite$ (Quenching above M_s temperature or cooling at 5°C/min).

Formation of alpha

TEM studies in Qazi et al.[35] estimated that the beta transus at 20±3 at.% H is below 900°C. When the samples were solution treated at 900°C for an hour, a single saturated beta phase (β_H) existed. Saturated beta decomposed to form saturated alpha when cooled below the beta transus temperature. Saturated beta decomposition was slower at 700°C and it increased with decreasing isothermal beta decomposition temperature.

Formation of hydrides

Authors [40,42, 51] quoted that beta phase dissolves up to 40 at.% H whilst alpha dissolves only 8 at.% H. When saturated beta transforms to alpha, the hydrogen distorts the alpha lattice. In order to eliminate the lattice distortion, hydrogen saturated alpha separates into hydrogen lean and hydrogen rich regions. [39] The hydrogen rich regions transform to hydride, this transformation is represented in **Figures 4.15 (e, f)**. The formation of hydrides causes a 0-5 vol.% [40] expansion of the lattice. This causes lattice strain energy which distorts the matrix. This strain energy coupled with reduced critical cooling rates for martensite formation may enhance martensite formation in hydrogenated Ti6Al4V.

Formation of martensite

The EBSD technique cannot distinguish between alpha and hexagonal martensite because they both have an hcp structure. However, XRD results in **Figure 4.6** show diminishing alpha peaks at 2 theta 36º for curves 14, 15 and 16. This indicates that upon hydrogenation and furnace cooling from 850ºC, 900ºC, and 950ºC more martensite was forming instead of alpha. Martensite was expected to form in **Figure 4.12 A-E)** because the heat treatment conditions satisfy the martensite formation conditions for hydrogenated Ti6Al4V. [35, 44]

The furnace cooling rate of 5ºC/min was above the critical cooling rate for martensite formation in Ti6Al4V alloyed with 20±3 at.% H. Qazi et al. [35] stated that non-hydrogenated Ti6Al4V requires a minimum cooling rate of 30ºC/min to form martensite and 1000ºC/min to form a fully martensitic microstructure. In comparison, Ti6Al4V alloyed with 20 at.% H requires a minimum cooling rate of 1.5ºC/min to form martensite and 10ºC/min to form a fully martensitic microstructure. [35] Therefore, martensite has the potential to form in **Figures 4.12 B1-B2)** because it was furnace cooled at 5 ºC/min. This cooling rate is above the minimum critical cooling rate for martensite formation at 20 at.% H. [35]

After beta decomposition, all samples were water quenched. It is expected that martensite will form in **Figures 4.12 C-E)** because the isothermal beta decomposition temperatures (500ºC, 600ºC and 700ºC) are above the martensite start (M_s) temperature. Fujii [52] stated that the M_s temperature for Ti6Al4V alloyed with 15 at.% H is 480ºC [52] and this decreases with increasing hydrogen concentration. However, the microstructures in **Figure 4.15 (e,f)** suggest that the beta phase might have been completely decomposed prior to quenching from 500ºC.

The decomposition of martensite upon aging is explained in **Section 4.5**.

4.5 Martensite decomposition (THP-MD) in hydrogenated Ti6Al4V

In **Figure 4.16**, the as cast microstructure was hydrogenated to 20±3 at.% H, solution treated at 900°C for an hour and quenched (ST+quench). The solution treated and quenched microstructure has needle hcp and retained metastable beta [49, 50] **(Figure 4.13)**. Aging this microstructure at 580°C gives rise to the microstructures in **Figures 4.16-4.17**.

Aging at 580°C decomposed the retained beta in **Figure 4.13** to form a needle hcp (α/ά) and presumably hydrides **(Figures 4.16-4.17 a-f)**. However, the hydride phase was poorly indexed by EBSD in **Figures 4.17 b), d), f)**. Hydrides are expected to form because bcc phase decomposed to acicular hcp phase (α/ά). The hcp phase dissolves 8 at.% H. [39, 42, 51] This leaves supersaturated hydrogen to form hydrogen rich regions [39] that transform to hydrides.

The needle hcp morphology is still visible after 73 hours of aging **(Figures 4.16 (73)** and **4.17 e)**. This was also observed by Qazi et al. [44] after 100 hours of aging in **Figure 2.17 h)**. Qazi et al. [44] stated that if martensite is aged above its martensite start (M_s) temperature (480°C)[52] it temporarily transforms to metastable beta. This metastable beta decomposes to equilibrium alpha during aging. If the samples are quenched from aging temperature and this aging temperature is above the (M_s) temperature, metastable beta transforms back to martensite. In this work, the aging temperature (580°C) is above the (M_s) temperature (480°C)[52] thus martensite is expected to form in the aged and quenched samples.

The phase transformations that occur during aging and subsequent quenching are:

i. Retained Beta $\xrightarrow[Aged\ at\ 580°C]{}$ needle and acicular hcp (α/ά)**.**

ii. Martensite $\xrightarrow[Aged\ above\ M_S\ at\ 580°C]{}$ metastable beta → saturated alpha →hydrides.

iii. Residual metastable beta $\xrightarrow[Quenched\ from\ above\ M_S\ at\ 580°C]{}$ needle hcp martensite.

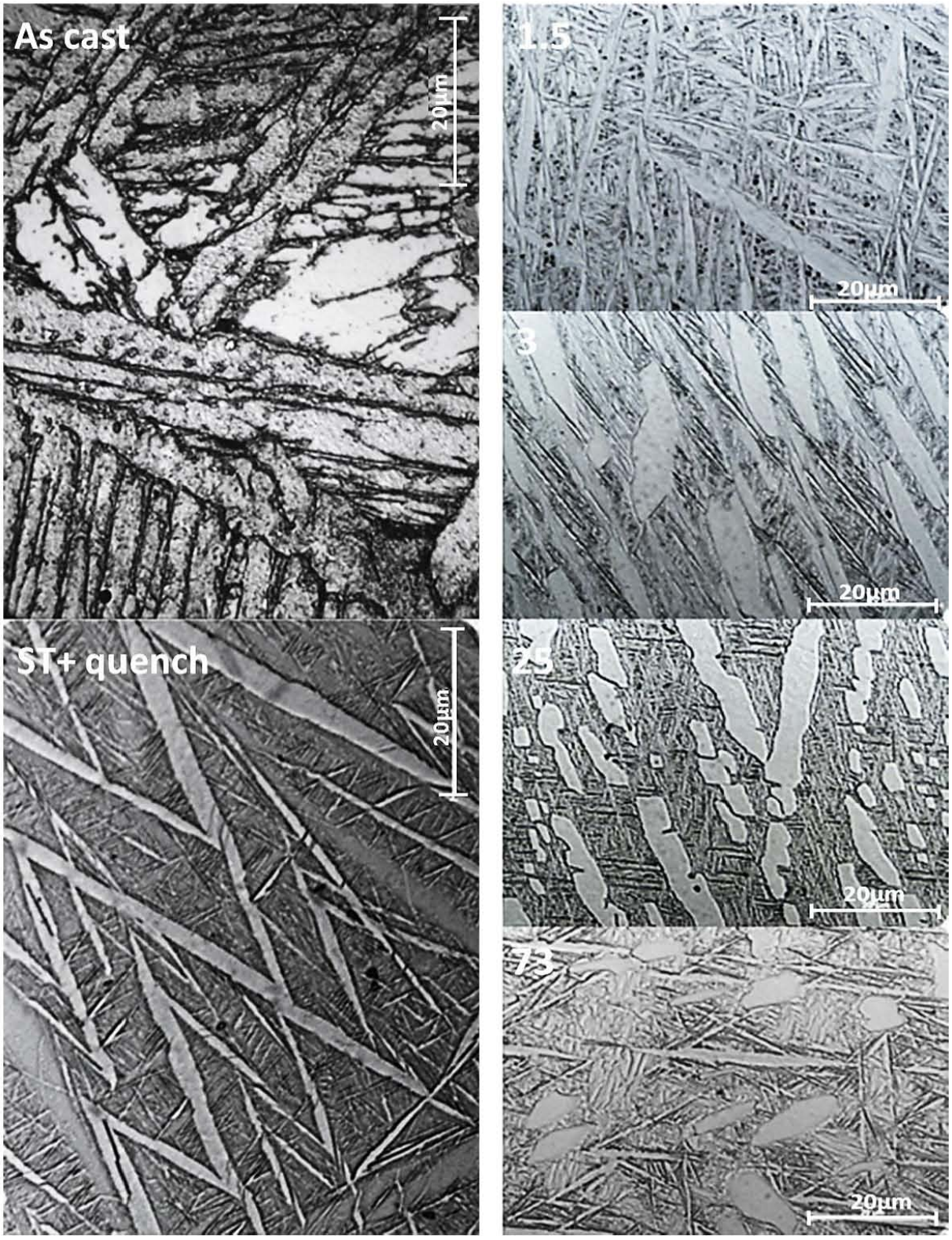

Figure 4.16: *Optical images of THP-MD samples showing the microstructure evolution from as cast Ti6Al4V to a hydrogenated-solution treated-quenched (ST+ quench) Ti6Al4V condition and lastly an aged at 580ºC (from 1.5 hours to 73 hours) condition.*

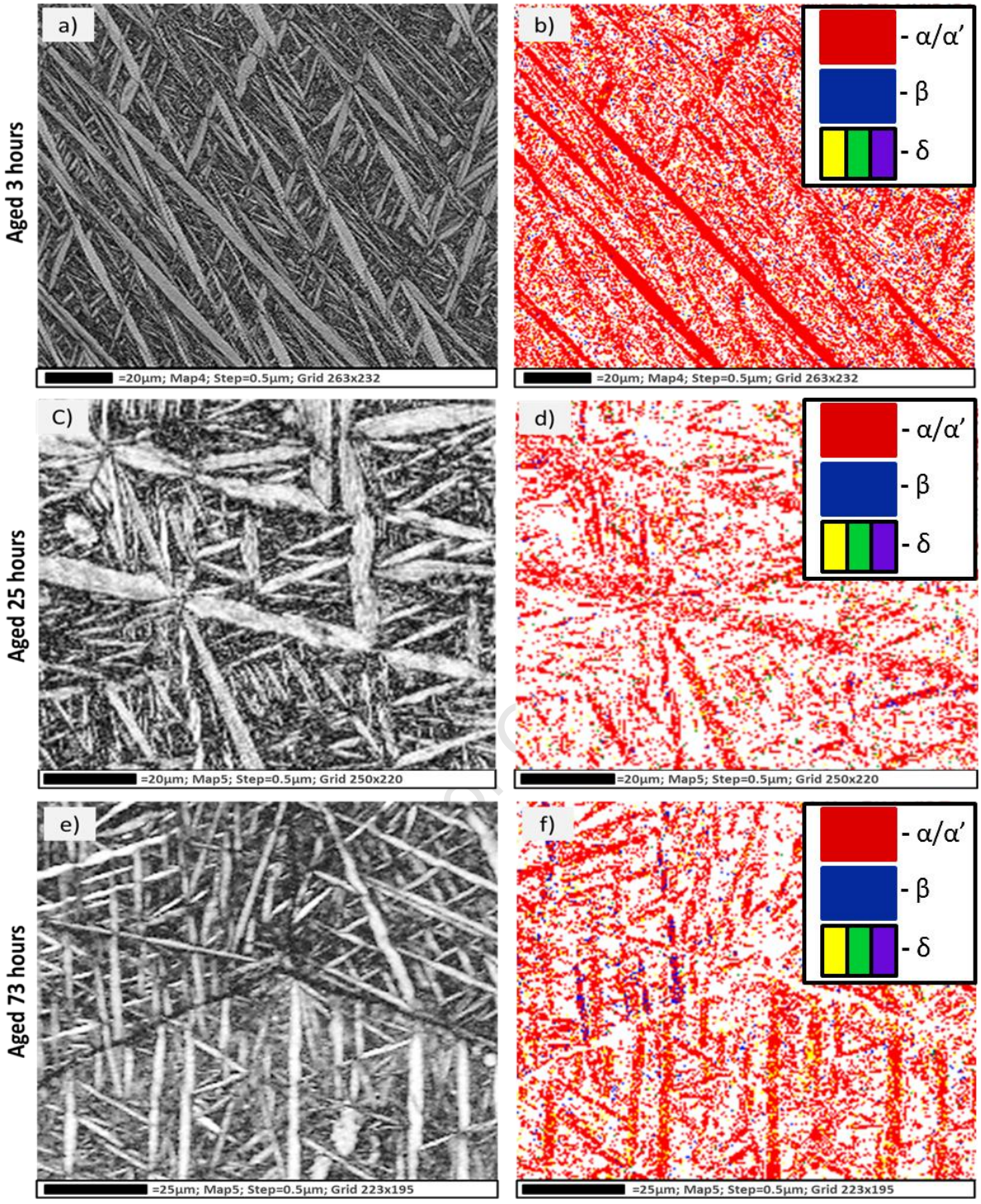

Figure 4.17: *Band contrast a), c), e) and phase b), d), f) maps of hydrogenated, solution treated, quenched and aged samples at 580°C for 3 (a-b), 25 (c-d) and 73 hours (e, f). In images b), d), f), red is hcp (α/ά), blue is bcc, yellow, green and purple are three forms of hydrides. Non-indexed regions are white.*

4.5.1 Effect of martensite decomposition (THP-MD) on hardness

In **Figures 4.18 a), b)**, a minimum of 30 hardness measurements were taken per sample condition. The hardness indents were made across the 18 mm diameter sample surface and they were spaced at least 1 mm apart. **Figure 4.18 a)** was hydrogenated to 28±3 at.% H at 650ºC for 8 hours. **Figure 4.18 b)** was hydrogenated to 20±3 at.% H at 850ºC for 3 hours. The control experiment was not hydrogenated but was solution treated, quenched and aged at similar conditions to **Figures 4.18 a), b).** The box and whisker plots show the distribution of the hardness data. The interquartile range (IQR) is the 3rd quartile minus the 1st quartile. Outliers are hardness values that are more than one and a half times the IQR (1.5 X IQR), either above the 3rd quartile or below the 1st quartile respectively.

When aging martensite in hydrogenated Ti6Al4V hardness increases [35] because the softer martensite phase decomposes to harder alpha and hydride phases. The hardness peaks after 1.5 hours of aging and then plateaus. The peak hardness corresponds to completion of the martensite to alpha, beta and hydride transformation. There is no difference in hardness increase between specimens hydrogenated to a) 28±3 at.% H or b) 20±3 at.% H.

Hardness increases in both hydrogenated and non-hydrogenated (control) conditions because softer metastable beta and hexagonal martensite [35] decomposes to harder alpha. In addition, the hardness increase could also be caused by the formation of intermetallics. The magnitude of the hardness increase (from as cast Ti6Al4V hardness) is greater in hydrogenated Ti6Al4V when compared to non-hydrogenated Ti6Al4V. After 1.5 hours of aging, the average hardness increase in hydrogenated Ti6Al4V was 100HV and non-hydrogenated Ti6Al4V was 30HV. This difference could be caused by hydrogen solution strengthening and the formation of hydride in hydrogenated specimens. The formation of hydrides and the solution of hydrogen in alpha and beta distorts the lattice by 0-5 % and 9-11 %[40] respectively. The lattice distortion causes stress fields that are accommodated by plastic deformation of the adjacent matrix. This increases the amount of dislocations in the microstructure. A greater number of dislocations increase the materials resistance to further deformation and thus increases its hardness.

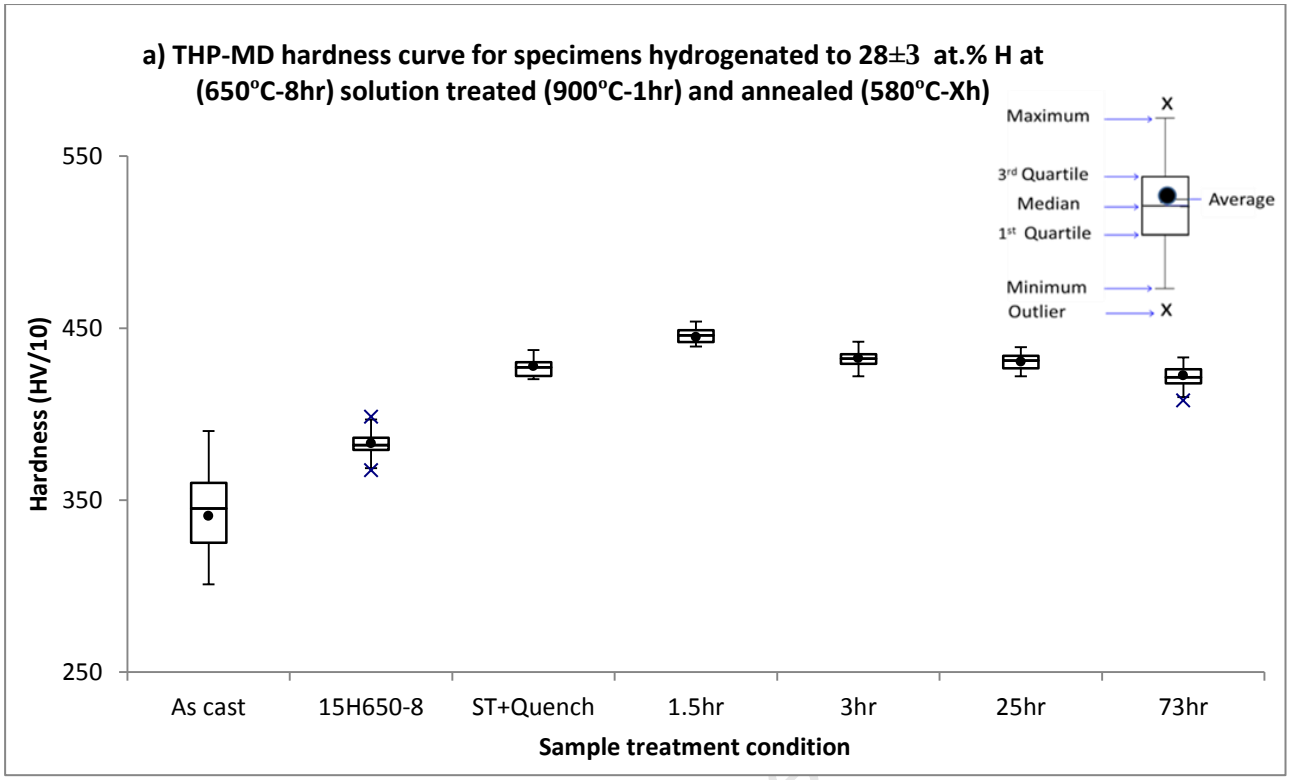

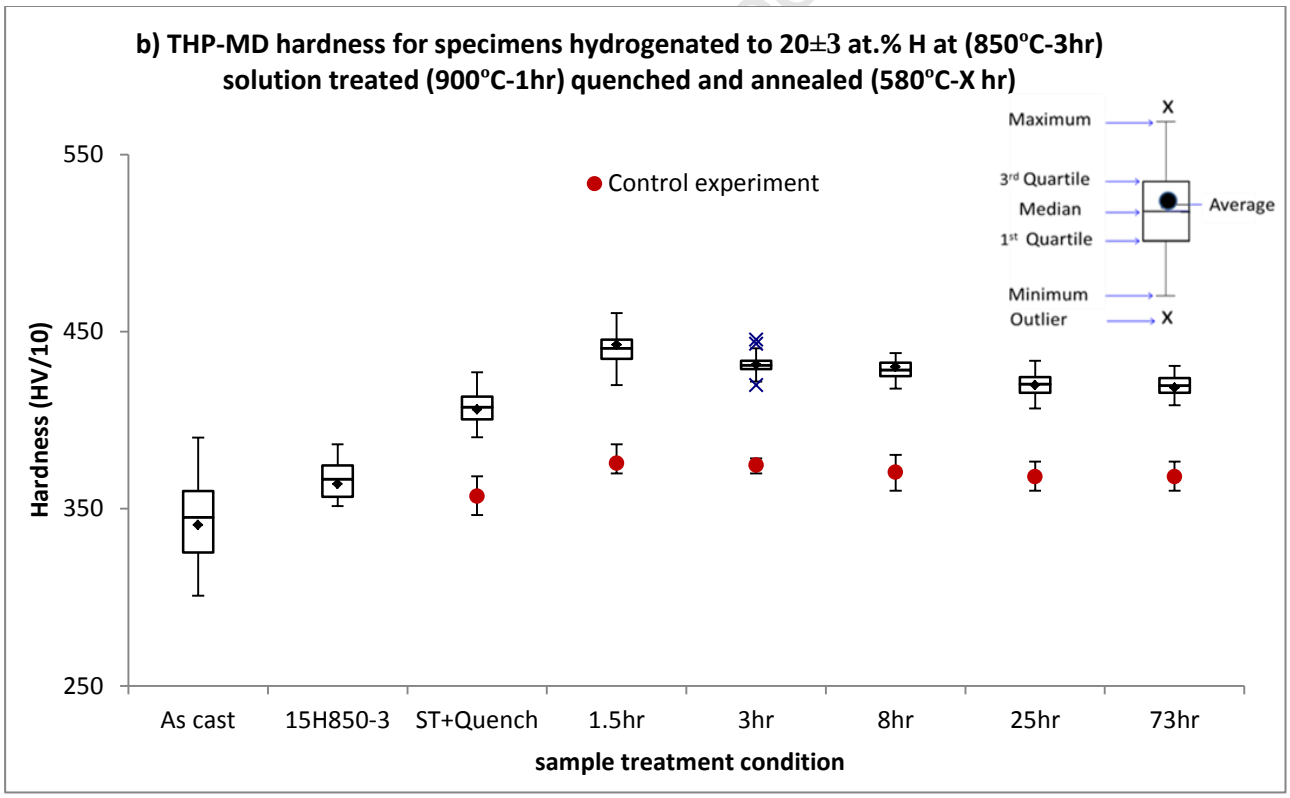

Figure 4.18: *Metastable phase decomposition of the softer martensite phase to harder alpha phase. The control in b) shows that there is a general hardness increase associated with aging Ti6Al4V but this is lower than the hardness increase in hydrogenated Ti6Al4V.*

4.6 Extent of refinement achieved from THP

The thermohydrogen (THP) methods explored were beta decomposition (THP-BD) and metastable phase decomposition (THP-MD). An amount of at least 20±3 at.% H was alloyed to decrease the beta transus temperature in order to solution treat at a lower temperature. It was found that 20±3 at.% H reduced the beta transus to temperatures below 900°C. Solution treating could be done at 900°C and this resulted to finer Widmanstätten lamellae.

Beta phase decomposition in **Figure 4.15 e), f)** formed hydride phase and discontinuous alpha morphology. Decomposing the as quenched metastable phases in **Figures 4.16-4.17** formed needle hcp and hydride phases. The nucleation and growth associated with the decomposition of beta and metastable phases refined the alpha and beta grains. Yoshimura[53] stated that martensite forms high density dislocations which act as nucleation points for recrystallisation of grains.

In the present work, beta and martensite decomposition refined the morphology of the alpha and beta phases. However, they did not refine the prior beta grain boundary network. **Figures 4.19-4.20** show that the prior beta grain boundary network is still visible after a solution treating, quenching and aging treatment.

In **Figures 4.19 a)-b)** the 1mm x 18mm diameter samples were hydrogenated to 20±3 at.% H, at 850°C for 3 hours in a 15 vol.% H atmosphere (15H850-3). Samples a) and b) were then solution treated for an hour at 850°C and 900°C respectively.

In **Figures 4.19 c)-d)** the 1mm x 18mm diameter samples were hydrogenated to 28±3 at.% H, in 15 vol.% H, at hydrogenation temperature 650°C for 3 hours (15H650-3). Samples c) and d) were then solution treated at 850°C and 900°C respectively. All samples were quenched after solution treatment.

The samples solution treated at 850°C in **Figures 4.19 a)** and **c)** were aged at 580°C to enhance martensite decomposition. **Figures 4.20 a)-d)** show the aged samples after (a, c) 1.5 hours and (b, d) 73 hours of aging respectively.

In **Figures 4.19-4.20**, the martensite decomposition treatment refined the morphology but did not eliminate the prior beta grain boundary network. Zhao et al.`s [38] positron annihilation analysis shows that Ti6Al4V refinement is caused by two processes, which are phase transformations and recrystallisation. Their work proved that increasing the hydrogen content to 30 at.% H increases dislocations. These dislocations act as nucleation points for finer alpha and beta grains which refine the morphology. However, Zhao et al. [38] and several other authors [10, 35, 36, 44] did not specify the effect of these transformations on the refinement of the as cast prior beta grain boundary network.

As cast prior beta grain sizes present an indelible influence on the extent of grain refinement that could be achieved from THP treatments. This is because of the persistent transformation orientation relationships that occur during THP treatments. Deformation and subsequent recrystallisation of these large prior beta grain sizes is necessary to eliminate their indelible effect on refinement.

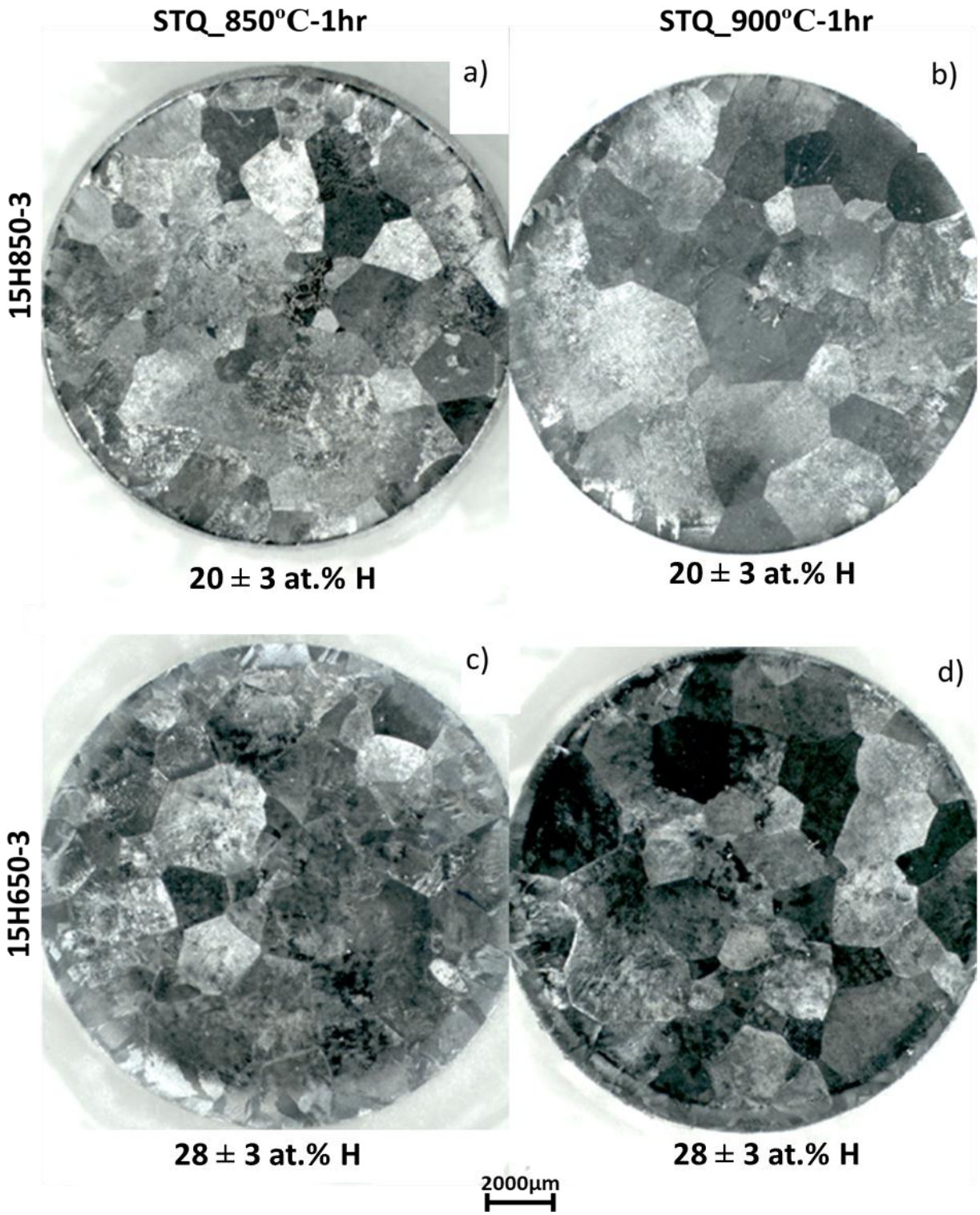

Figure 4.19: *Stereomicrographs of 1mm x 18mm samples showing prior beta grain sizes. Samples were hydrogenated for 3 hours at (a, b) 850°C and (c, d) 650°C, solution treated for an hour at (a, c) 850°C and (b, d) 900°C. Samples (a, b) and (c, d) have 20±3 at.% H and 28±3 at.% H respectively.*

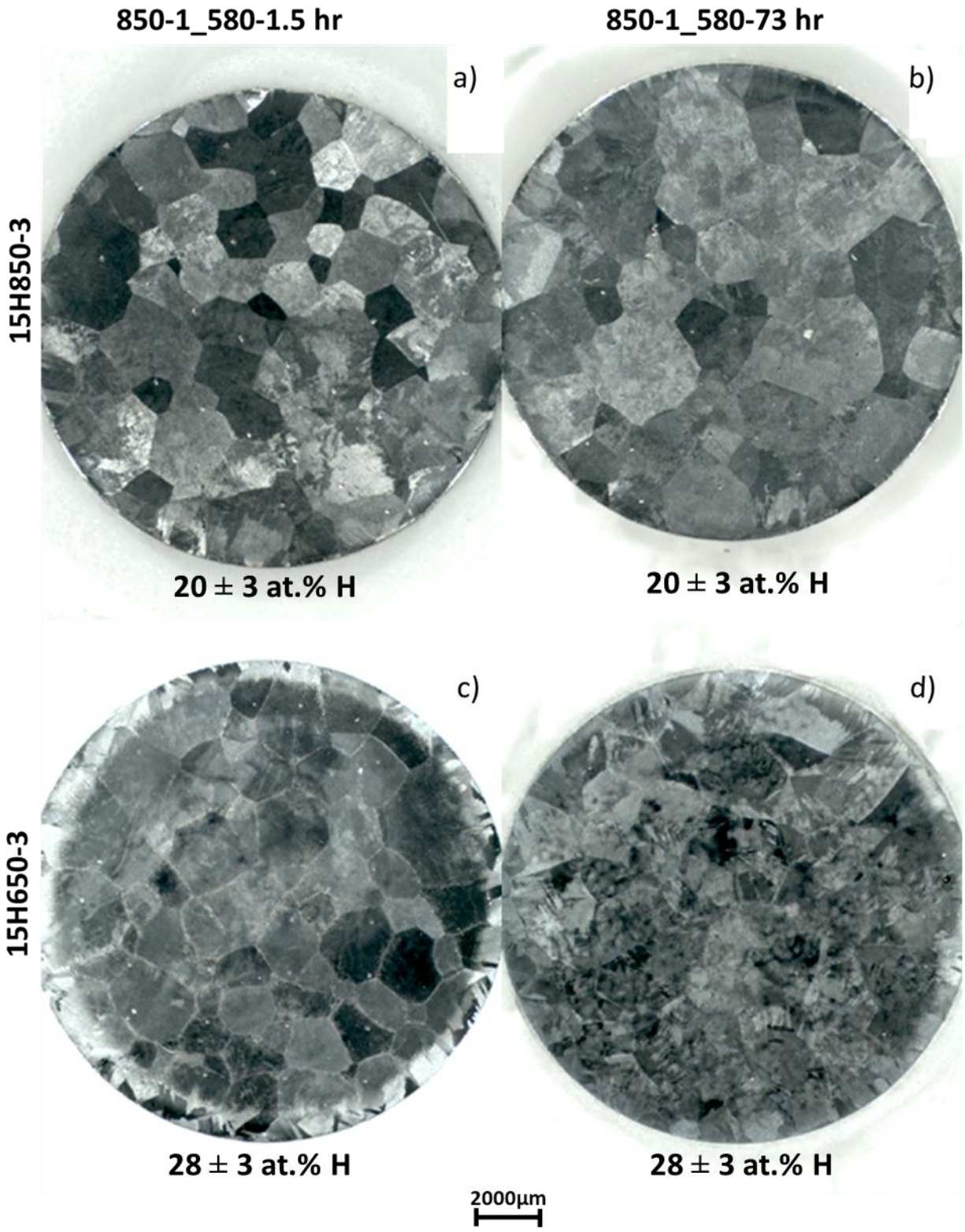

Figure 4.20: *Stereomicrographs of 1mm x 18mm diameter samples showing prior beta grain sizes after of aging treatment at 580°C for a), c) 1.5 hours and b), d) 73 hours. Samples (a, b) and (c, d) have 20±3 at.% H and 28±3 at.% H respectively.*

4.7 Effect of hydrogen on hot deformability

As discussed in **Section 4.6**, beta and metastable phase (martensite) decomposition does not refine the prior beta grain boundary network. Therefore, deformation and recrystallisation are required to refine the prior beta grain sizes. **Figure 4.21** shows the deformed and non deformed regions of a plane strain compressed sample. The deformed region was deformed at 1000°C to a strain of 50% (0.5) at a strain rate of 10 s^{-1}. The specimen in **Figure 4.21** was recrystallised at 1100°C after deformation.

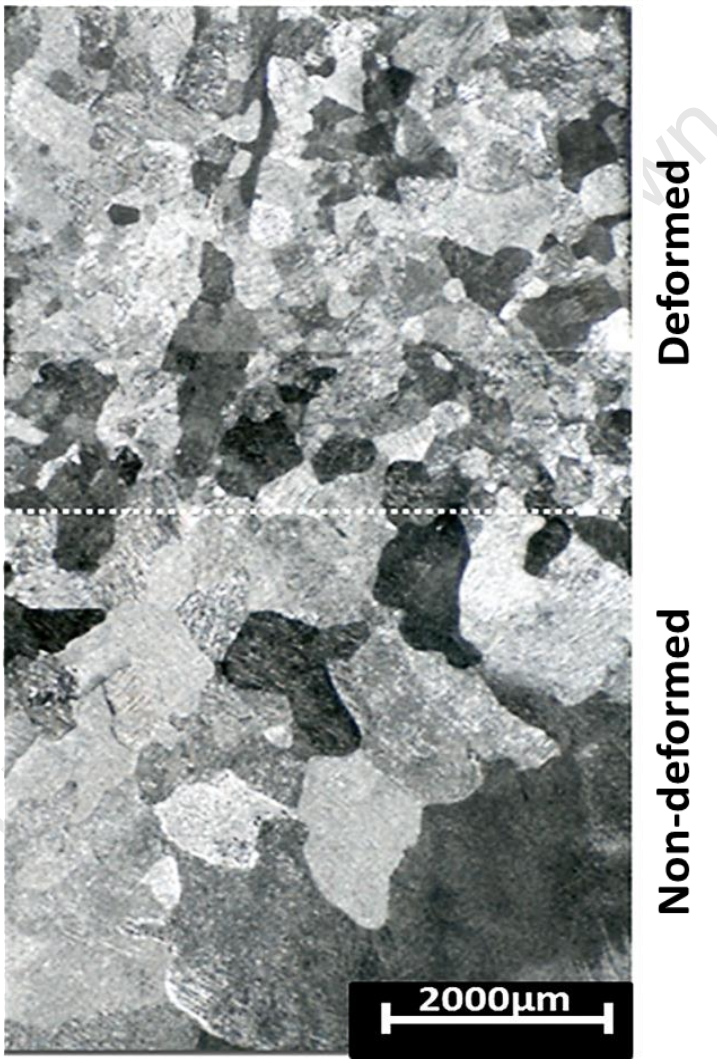

Figure 4.21: *Stereomicrograph of as cast Ti6Al4V, showing the deformed and non-deformed regions of a plane strain compressed and recrystallised sample. The sample was deformed at 1000°C and recrystallisation only occurred in the deformed region at a minimum recrystallisation temperature of 1100°C.*

In **Figure 4.21**, the deformed and non-deformed regions underwent a similar heat treatment cycle. Upon annealing, only the deformed region of the sample recrystallised.

The grain sizes in the recrystallised region are still relatively large. This is because samples deformed between 900°C-1000°C only recrystallise at a minimum annealing temperature of 1100°C. At high temperatures (1100°C) the grain growth exponents in titanium alloys are high.[5] It is therefore necessary to deform and recrystallise at lower temperatures to minimize grain growth and optimise refinement.

Figure 4.22 shows the hot deformation limits of a) as cast Ti6Al4V and b)-d) Ti6Al4V alloyed with 20±3 at.% H. A hot deformation limit is the lowest temperature at which deformation can be successfully performed without cracking specimens. The deformed cast and hydrogenated specimens cracked at 800°C and 500°C respectively. Their deformation limits are therefore 900°C and 550°C for the as cast and hydrogenated sample conditions respectively.

Figure 4.23 is a transverse section of **Figure 4.22 a)**, which is the as cast specimen deformed at 800°C. In **Figure 4.23**, region A is non-deformed and B and C are deformed. Shear caused the microstructure defects in **Figures 4.23 b), c)**. The flow instability in **Figure 4.23 b)** is caused by the deformation incompatibilities of the alpha and beta phases. This shears the lamellae to form kinks which eventually develop into cracks.

The low thermal conductivity of titanium enhances the formation of cracks **(Figure 4.23 c)**. Adiabatic heating causes localised flow at high strain regions, which are at 45° to the deformation direction. There is insufficient time to dissipate the adiabatic heat at high strain rates. This results in regions of increased material flow parallel to regions of low flow. The deformation incompatibilities between these two adjacent regions lead to development of cracks.

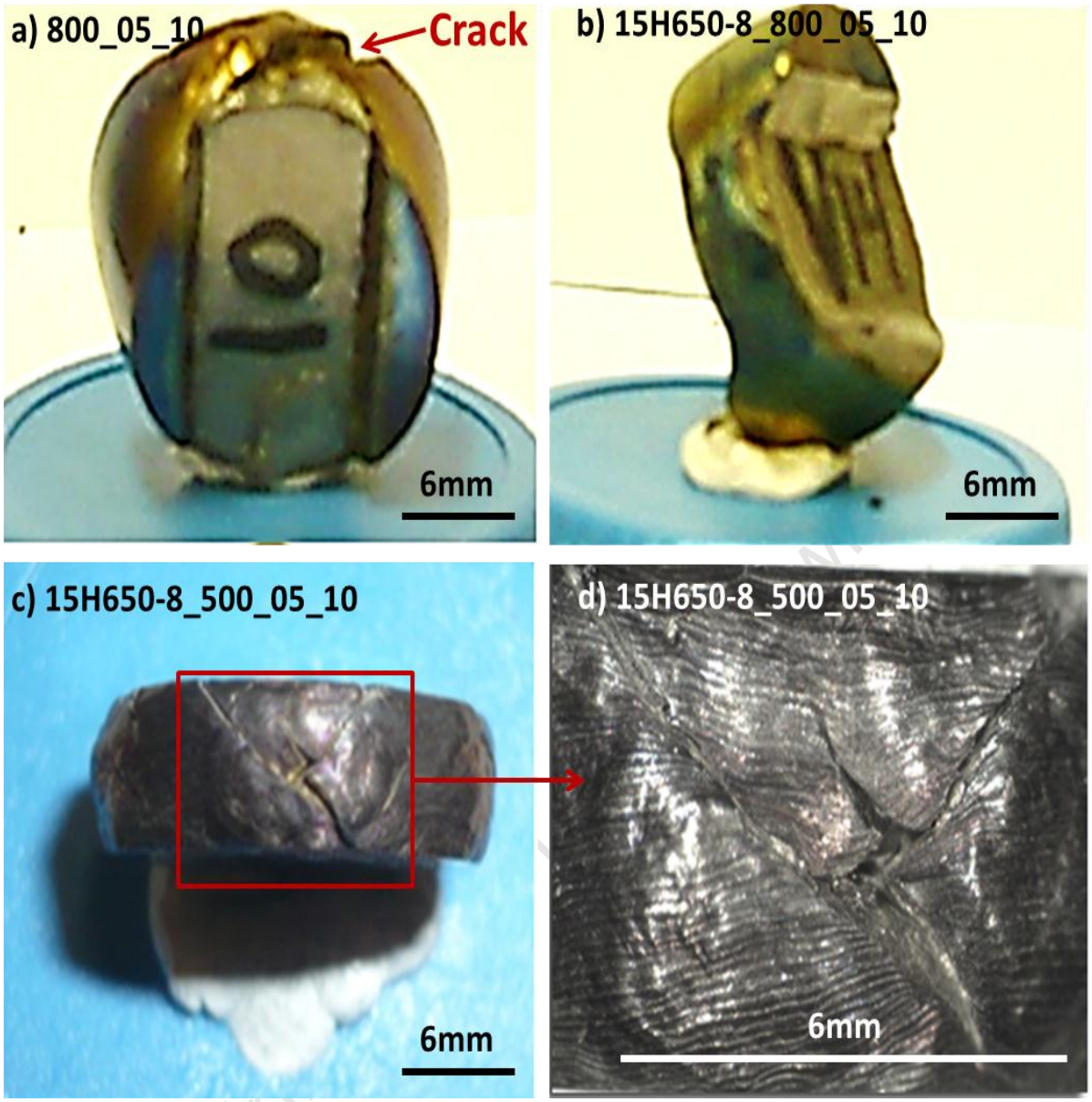

Figure 4.22: *Hot deformation limits of a) as cast Ti6Al4V and b)-d) Ti6Al4V alloyed with 20 at.% H. Image a) shows that as cast Ti6Al4V cracks when deformed at 800°C whilst hydrogenated Ti6Al4V in b) is deformable at 800°C but starts cracking at c) 500°C. The deformation temperature limits are 900°C (as cast) and 550°C (Ti6Al4V with 20±3 at.%H).*

Figure 4.24 is a transverse section of **Figure 4.22 b)** which is the Ti6Al4V specimen hydrogenated to 20±3 at.% H and deformed at 800ºC. In **Figure 4.24**, regions A and B are the deformed and non-deformed regions respectively. The optical images in **Figures 4.24 a), b)** show needle morphology and no microstructure defects (neither cracking nor flow instability).

The needle morphology was not observed in the as cast microstructure **(Figure 4.23)** but it formed in the hydrogenated microstructure in **Figure 4.24**. This indicates that hydrogen reduced the beta transus temperature and the critical cooling rate for martensite formation. More of the softer, deformable beta phase was present at 800ºC (deformation temperature) and this improved deformability. Subsequent quenching after deformation caused a beta to needle martensite transformation to occur upon quenching.

In summary, **Figures 4.22-4.24** show that the lowest temperature at which cast Ti6Al4V can be successfully deformed is 900ºC. Cast Ti6Al4V deformed at this deformation limit (900ºC) recrystallises at a minimum temperature of 1100ºC. At this recrystallisation temperature (1100ºC), optimum refinement is not achieved **(see Figure 4.21)** because the grain growth exponents are high.[5] To optimize refinement, it is necessary to recrystallise at lower temperatures. Lower recrystallisation temperatures can be achieved by increasing the stored deformation energy. One way of doing this is by deforming below the cast Ti6Al4V deformation limit (900ºC).

In the present work, hydrogen (20±3 at.% H) was used to optimize low temperature deformability by decreasing the deformation limit from 900ºC (as cast) to 550ºC (hydrogenated). This improvement in low temperature deformability is evident when comparing **Figure 4.23** to **Figure 4.24**.

Improved low temperature deformability is also shown in the flow stress graphs in **Section 4.8**. The effect of deforming at lower temperatures on the minimum temperature required to recrystallise grains is shown in **Section 4.9**.

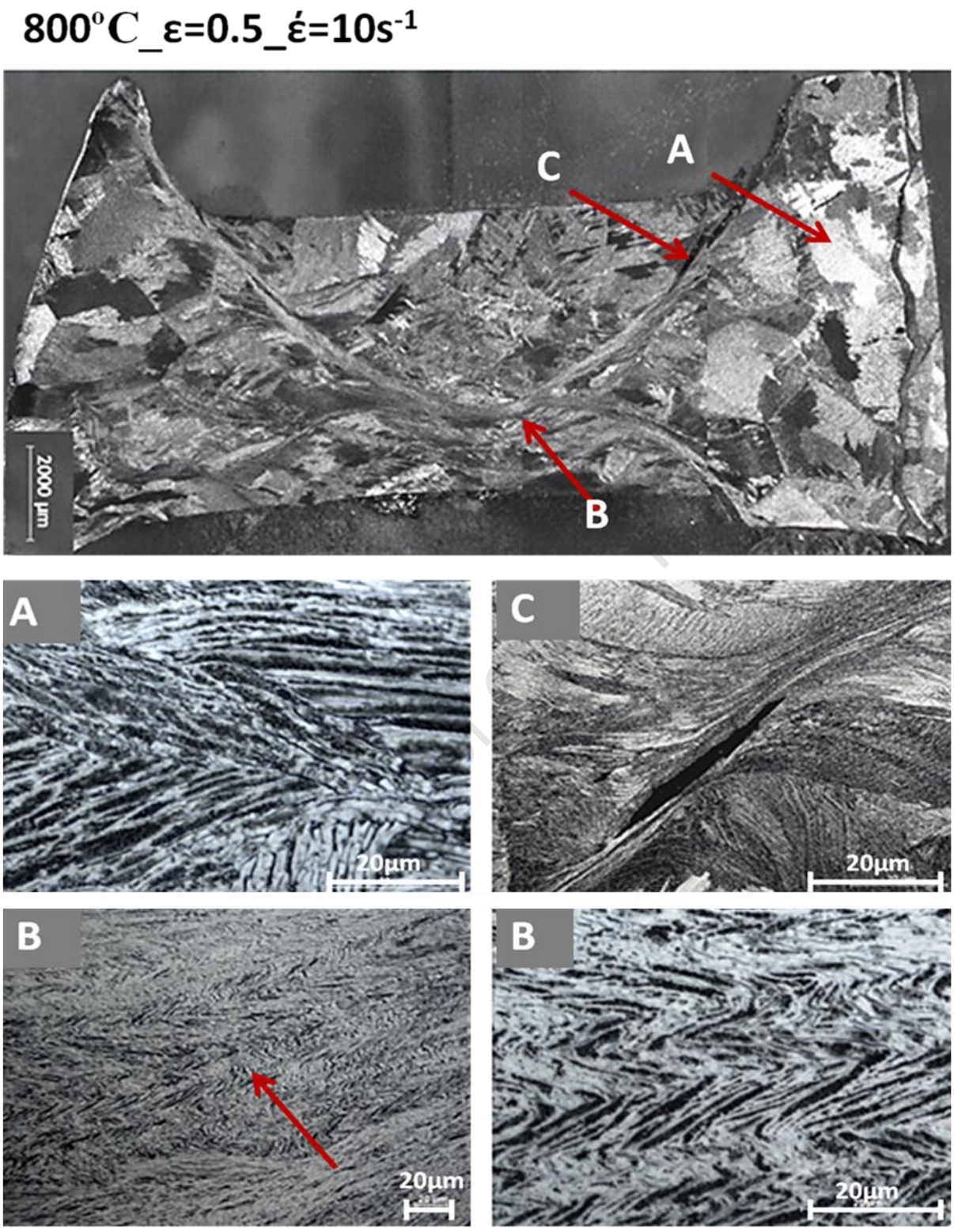

Figure 4.23: *Optical images of as cast Ti6Al4V deformed at 800°C, 50% strain (0.5) and strain rate 10 s^{-1}. The non-deformed region a) has a lamellar microstructure. The deformed regions show b) flow instability and c) cracking. Microstructure defects b) and c) are caused by shearing.*

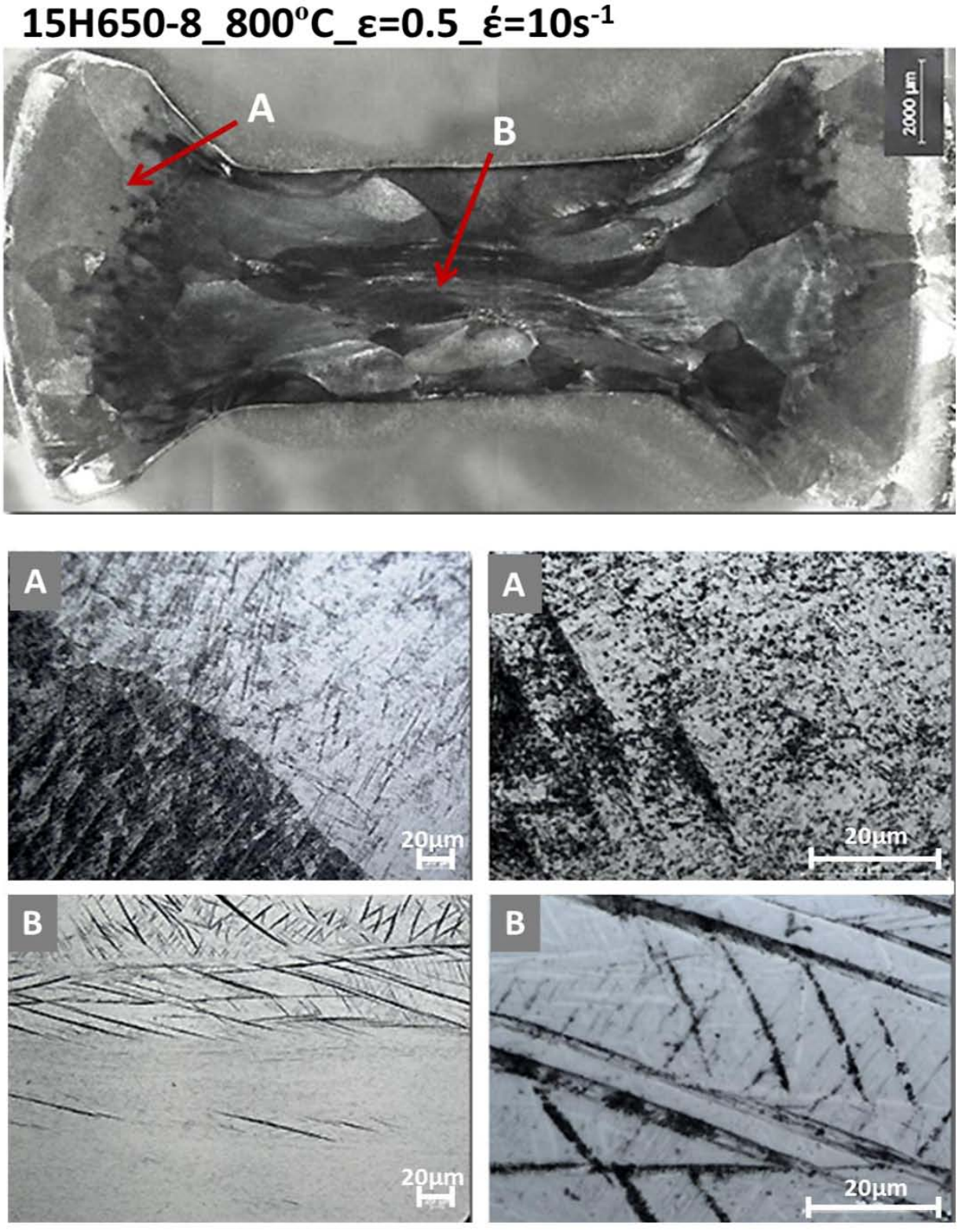

Figure 4.24: *Optical images of Ti6Al4V hydrogenated to 20±3 at.% H, deformed at 800°C, 50% strain (0.5) and strain rate 10 s^{-1}. Images a)-b) show martensite needles and no microstructure defects. Alloying with 20±3 at.% hydrogen improved Ti6Al4V deformability at 800°C.*

4.8 Effect of hydrogen on flow stress

In **Figures 4.23-4.24**, the as cast specimen cracked and the hydrogenated specimen did not crack. **Figure 4.25** shows the flow stresses of the plane strain compressed samples in **Figures 4.23-4.24**. The alloyed 20±3 at.% H reduced the peak flow stress by almost 35% from 1000 MPa (as cast) to 650 MPa (hydrogenated) as shown in **Figure 4.25**.

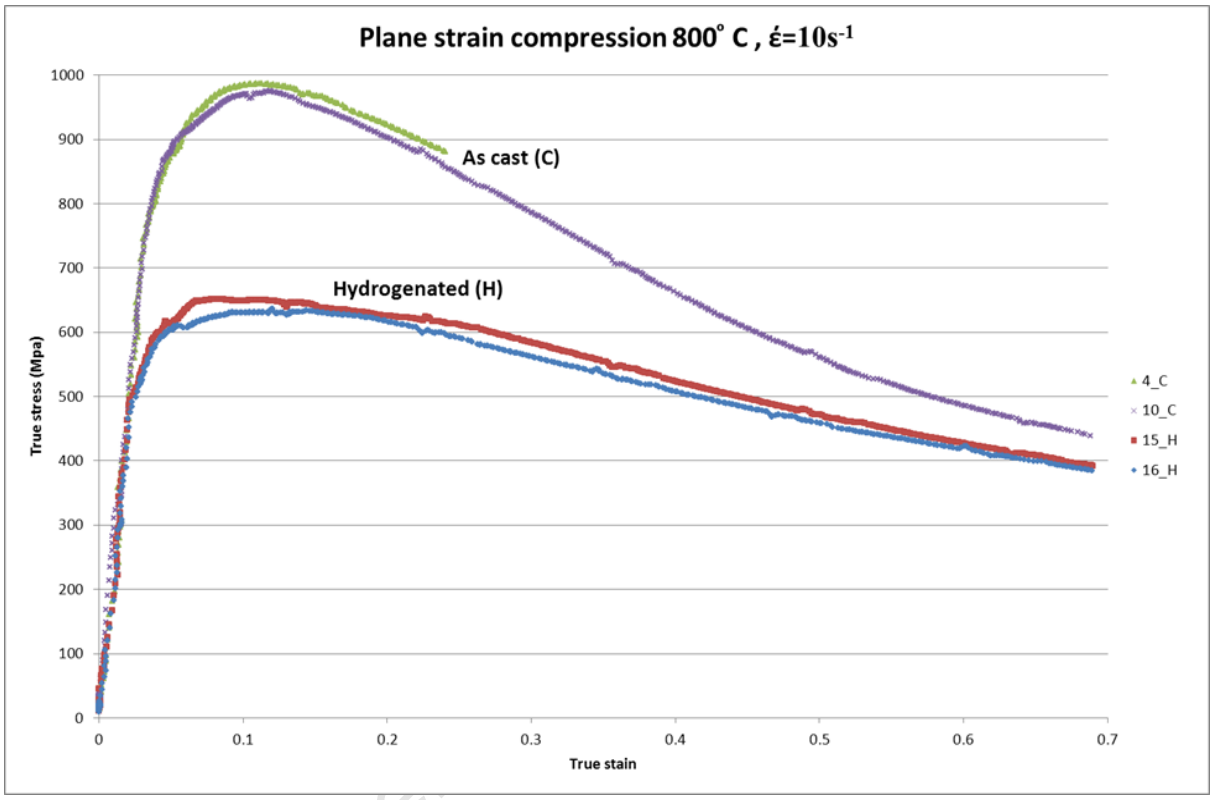

Figure 4.25: *Plane strain compression at 800°C showing the effect of 20±3 at.% H on flow stress. The flow stress of hydrogenated (HD) specimens is lower than that of as cast (c) specimens. This shows that 20±3 at.% H reduced the peak flow stress by up to 35 % which improved deformability at 800°C.*

In **Figure 4.25**, the cracking of as cast (c) specimens at 800°C is manifested by a rapid decrease in true stress from 1000 MPa to 450 MPa with increasing strain from 0.1 to 0.7. The flow curves of the hydrogenated (H) samples also show a decrease in true stress with increasing true strain. This decrease can be attributed to flow softening which is caused by adiabatic heating. This raises localised temperatures and stabilises softer, deformable beta phase. Increasing levels of deformable beta phase lowers the flow stresses.

In **Section 4.7**, it was specified that a deformation limit is the lowest temperature at which deformation can be done without cracking specimens. Uniaxial compression in **Figure 4.26** also shows that cast and hydrogenated Ti6Al4V specimens crack at 800°C and 500°C. Therefore, their deformation limits are 900°C and 550°C respectively.

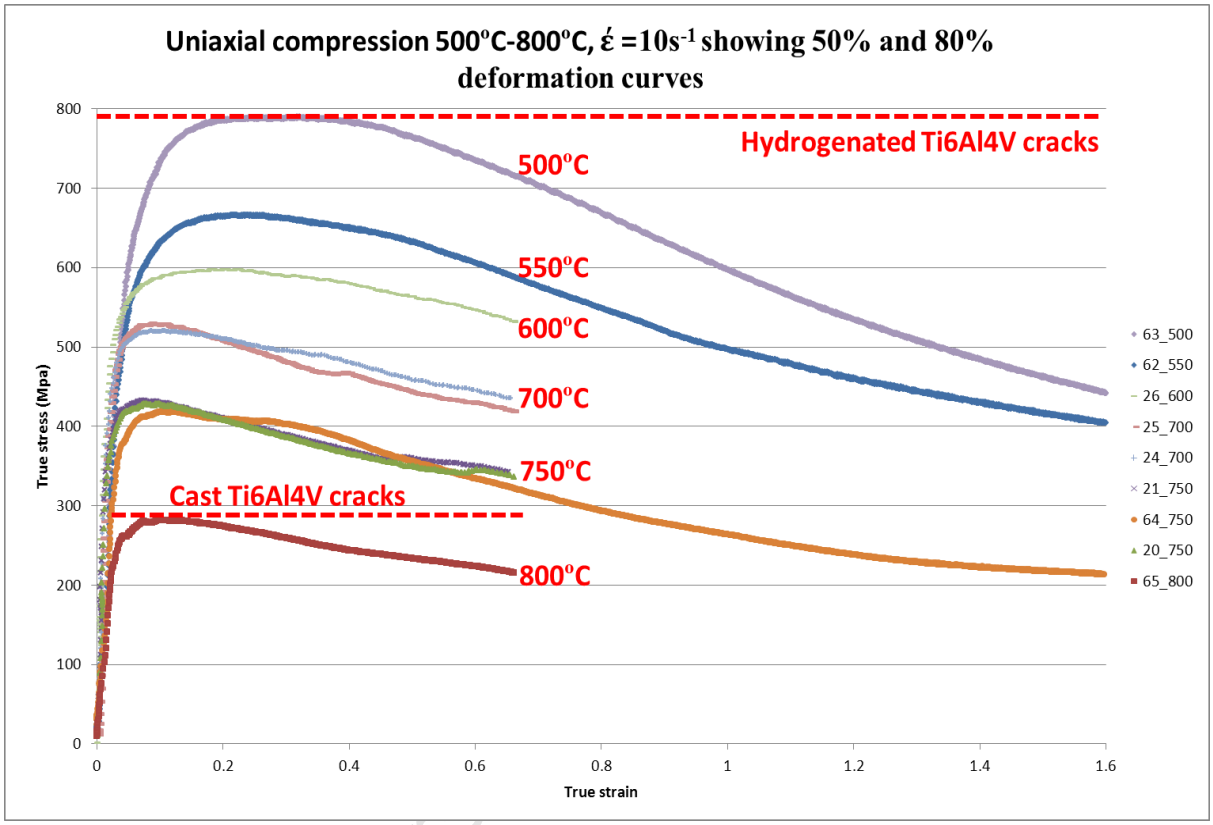

Figure 4.26: *Uniaxial compression of hydrogenated samples at temperatures 800°C to 500°C. Alloying Ti6Al4V with 20±3 at.% H improves deformability from 50% at 800°C to 80% at 550°C. The dotted lines show that as-cast Ti6Al4V cracks at 50% deformation at 800°C whilst hydrogenated Ti6Al4V cracks at 80% deformation at 500°C.*

In **Figure 4.26**, alloying Ti6Al4V with 20±3 at.% H increased the feasible deformation from 50% at 800°C to 80% at 550°C. This means that 20±3 at.% H improved deformability up to 350°C below the cast Ti6Al4V deformation limit. The flow stress increases from 300 MPa to 800 MPa with a decrease in deformation temperature from 800°C to 500°C respectively. Hydrogen improves deformability at lower temperatures by stabilising more beta phase. It also reduces the dislocation density by releasing pinned dislocations and promoting dislocation climb.[54]

Uniaxial compression in **Figure 4.27** also shows that hydrogen caused an approximate 35% decrease in peak flow stress from 420 MPa (as cast-C) to 275 MPa (hydrogenated). This decrease is caused by hydrogen because compressing hydrogenated and dehydrogenated (HD) samples yields peak flow stresses that are similar to the as cast (C) condition (420 MPa). The slightly higher peak flow stresses (450 MPa) could be caused by morphology refinement that occurs during formation and decomposition of hydrogen induced phases.

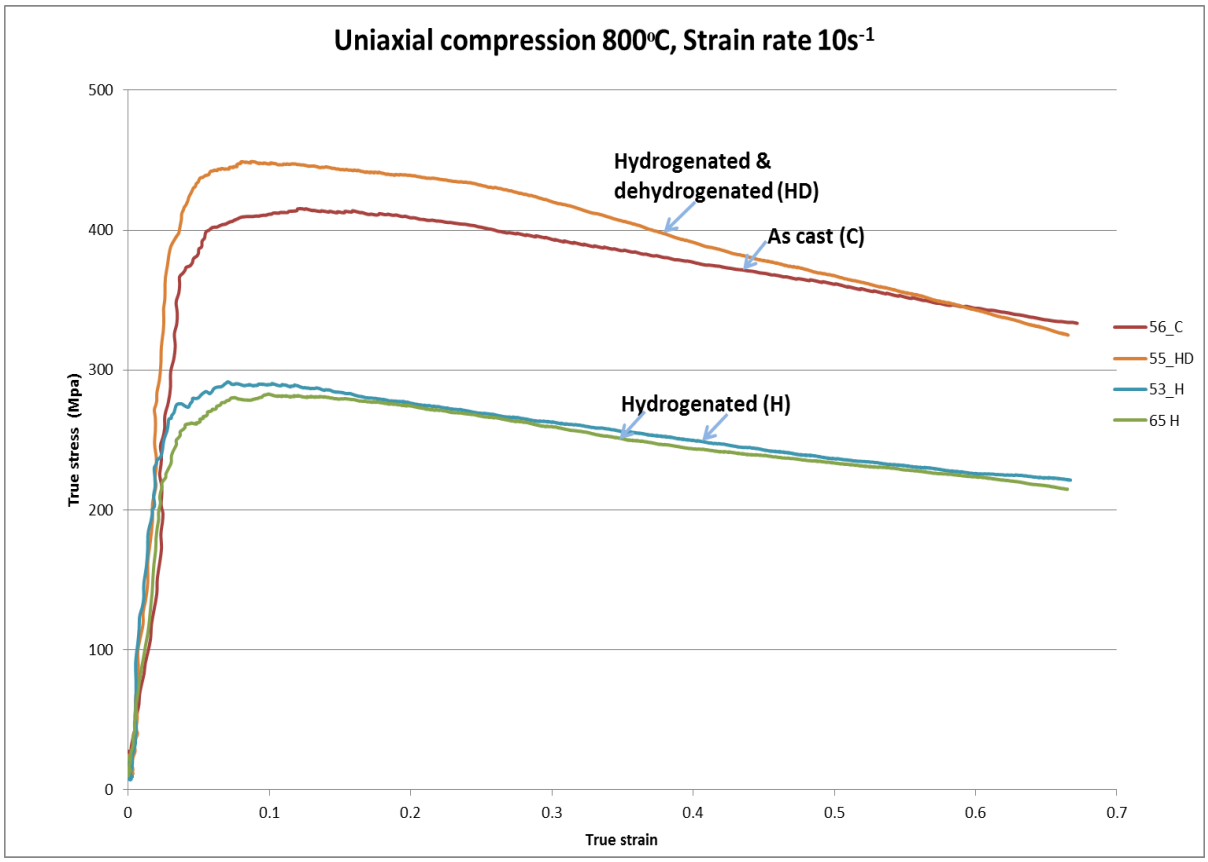

Figure 4.27: *Uniaxial compression at 800°C shows that hydrogen is responsible for the 35% decrease in peak true stress. This is illustrated by compressing hydrogenated and dehydrogenated specimens (HD) which yield flow stresses similar to as cast (C) specimens.*

In **Figure 4.28**, hydrogen alloying caused a 25% decrease in peak flow stress from 300MPa (as cast) to 225 MPa (hydrogenated). Deforming hydrogenated and dehydrogenated (HD) samples resulted in flow stresses that are slighty higher (340 MPa) than the as cast (C) condition (300 MPa). This observation is consistent with the findings in **Figure 4.27** and it can be attributed to morphology refinement that occurs during the hydrogenation and dehydrogenation proscess.

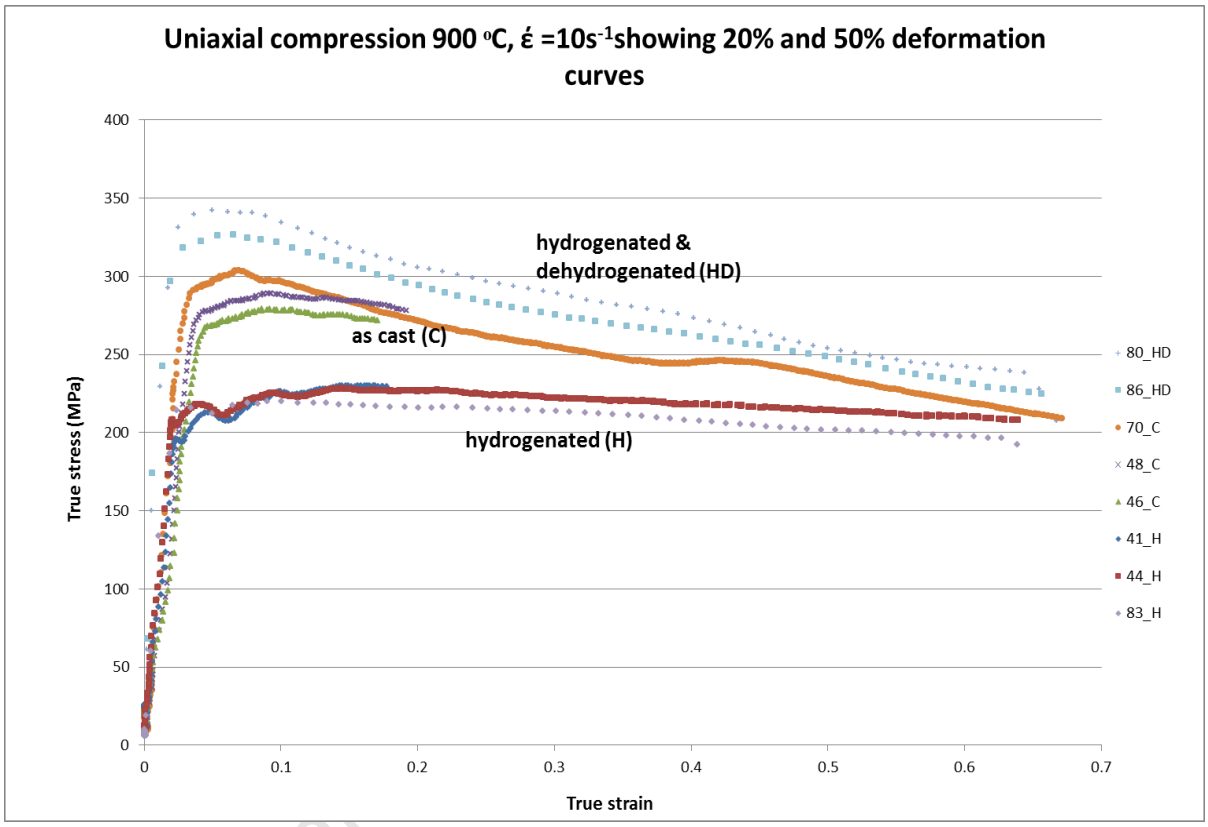

Figure 4.28: *Uniaxial compression at 900°C shows a 25% decrease in peak flow stress. Hydrogen softening decreases with increasing deformation temperature from 800°C to 900°C.*

In **Figures 4.27-4.29**, the effect of hydrogen on flow stress decreases with increasing deformation temperature from 800°C to 900°C. Hydrogen softening decreased between deformation temperatures 800°C and 900°C from 35% to 25% respectively. This is because hydrogen decreases the flow stress by stabilising the softer, deformable beta phase at lower temperatures. At higher deformation temperatures (900°C) more beta phase is anyway present in Ti6Al4V and deformability improves. Therefore, hydrogen`s beta stabilising effect becomes less significant.[22, 46, 55]

Decreasing hydrogen softening with increasing deformation temperature is further highlighted in **Figure 4.29**, where hydrogen softening is reduced to 0% at 1000ºC. In **Figure 4.29**, there is no significant difference between the flow stresses of as cast (c) and hydrogenated (H) sample conditions at 1000ºC. Their flow stresses are all between 150MPa and 200 MPa. This is because both the cast (c) and hydrogenated (H) samples are in the single phase beta region at 1000ºC. Therefore, hydrogen's beta stabilising effect is insignificant.

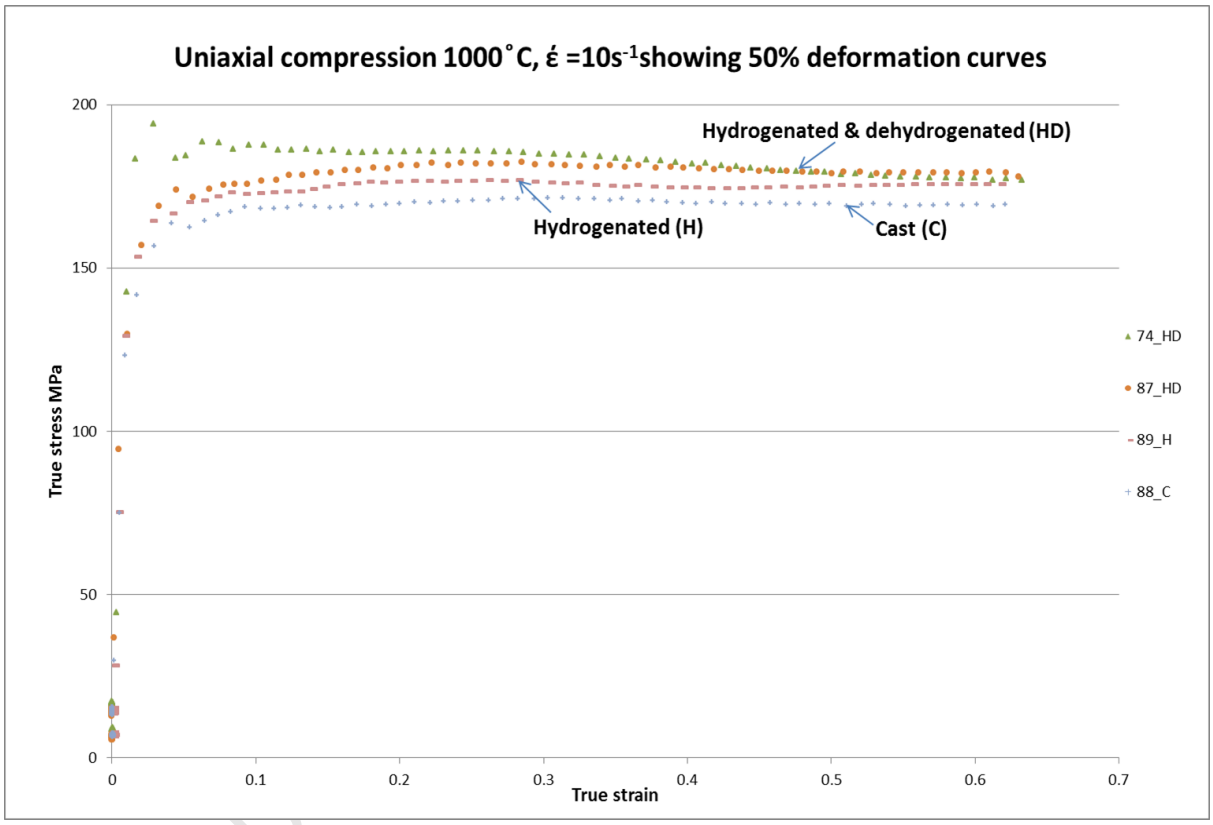

Figure 4.29: *Uniaxial compression results at 1000ºC showing no differences in the peak flow stresses of hydrogenated and as cast samples. No hydrogen softening was observed at 1000ºC.*

Figure 4.29 shows no evidence of flow softening, meaning the effect of localised adiabatic heating on the flow stress was less prominent at 1000ºC. This is because adiabatic heating causes flow softening by stabilising more beta at localised regions. At 1000ºC a single phase beta region exists and this nullifies any effects that localised heating can have on the flow stress. In conclusion, the effects of hydrogen and localised adiabatic heating on flow stress are prominent at lower deformation temperatures where less beta phase is stable.

4.9 Post deformation annealing

Deformed specimens were annealed to promote recrystallisation, decompose metastable phases, remove hydrogen and decompose hydrides. This section discusses the microstructure evolution during post deformation annealing.

4.9.1 Recrystallisation

Table 4.2 shows that there is a minimum temperature below which no recrystallisation occurs in deformed specimens. This minimum recrystallisation temperature is approximately half [56] the absolute melting temperature in alloys. This minimum recrystallisation temperature is required to thermally activate nucleation (in the non-classical sense) and growth.

Recrystallisation did not occur in **Figures 4.23-4.24** and the non-deformed part of **Figure 4.21**. This is because a critical amount of deformation stored energy is required for recrystallisation to occur. Recrystallisation therefore depends on the extent of prior deformation and the post deformation annealing temperature.

Energy is stored in materials in the form of defects, grain boundaries and surface energies. During deformation energy is stored in the material in the form of dislocations. The driving force for recrystallisation is releasing the stored deformation energy. The greater the deformation, the larger the stored energy, the lower the thermal energy required to recrystallise grains. **Table 4.2** shows that deforming at the lowest temperature of 550°C reduced the minimum temperature required to recrystallise grains from 1100°C to 800°C.

Table 4.2: *The effect of deformation parameters on minimum recrystallisation temperature*

Deformation Parameters		**Minimum Recrystallisation Temperature (°C)**			
Temperature(°C)	True Strain	1100	900	800	700
1000	0.7	✓	x		
900	0.7	✓	x	x	
800	0.7		✓	x	
750	1.6		✓	x	
700	0.7		✓	x	
600	0.2			✓	
600	0.7			✓	
600	1.6			✓	
550	1.6			✓	x

✓- Recrystallised x - Not Recrystallised

In **Table 4.2:**

i. All specimens deformed 900°C and above recrystallised at a minimum recrystallisation temperature of 1100°C.
ii. Samples deformed in the temperature range 700°C-800°C recrystallised at a minimum annealing temperature of 900°C.
iii. Only samples deformed below 600°C recrystallised at a minimum annealing temperature of 800°C.
iv. The minimum deformation temperature was 550°C; below this temperature hydrogenated specimens started cracking.
v. No recrystallisation was achieved below an annealing temperature of 800°C.

The microstructures of the specimens in **Table 4.2** are shown in **Figure 4.30.** In **Figure 4.30**, all the samples were prior hydrogenated to 20±3 at.% H, deformed and recrystallised. The deformation conditions are represented by the vertical captions on the left of the microstructures for example 900_08_10. The caption 900_08_10 means that the sample was deformed at 900°C, 80% strain (0.8) and strain rate of 10 s^{-1} **(see Section 3.6.1)**. The recrystallisation temperatures are written in the top left corner of each micrograph.

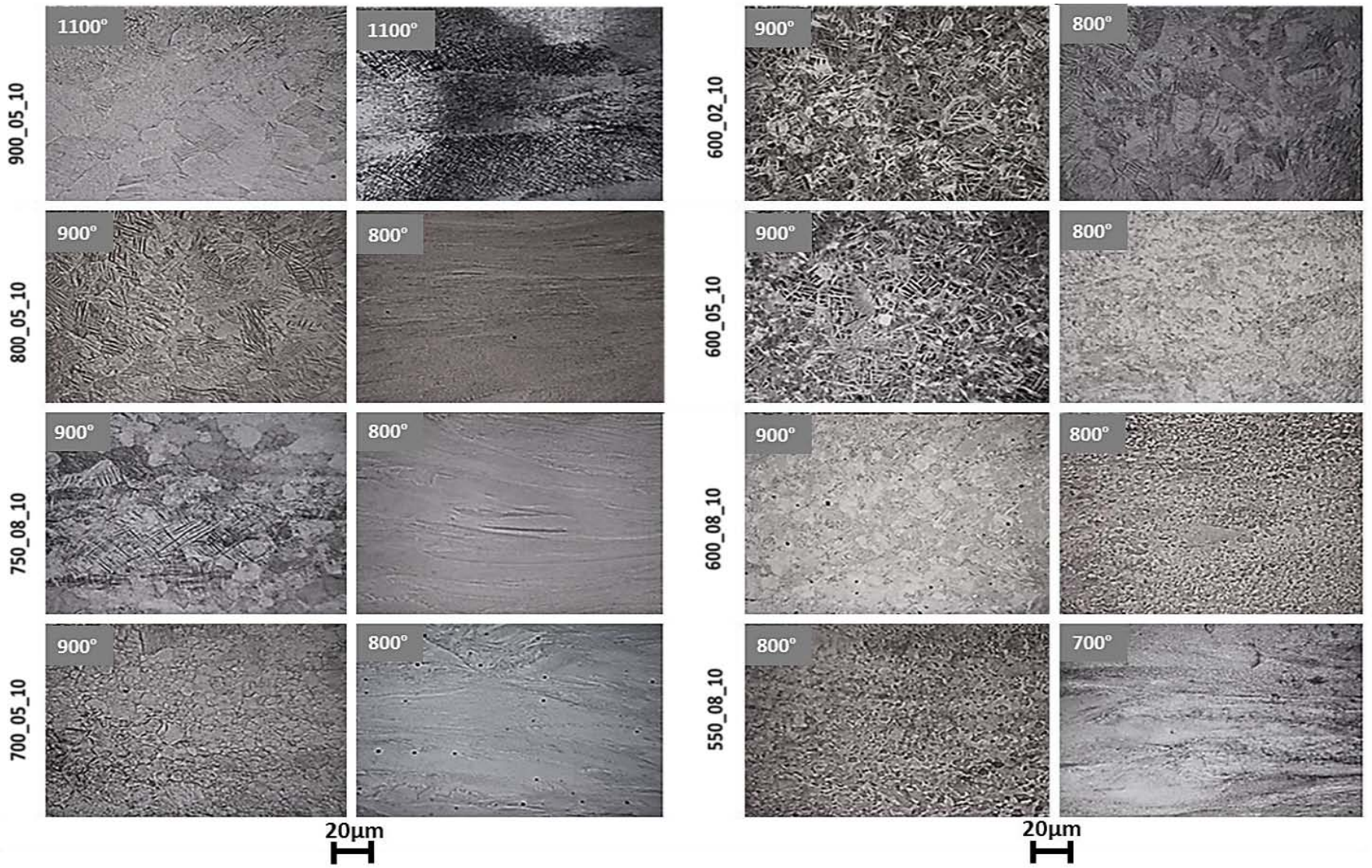

Figure 4.30: *Optical images illustrating the relationship between deformation temperature, strain, recrystallisation temperature and grain size.*

In **Figure 4.30**, samples deformed at 900ºC (900_05_10) did not recrystallise at 900ºC, they only recrystallised above 1100ºC. EBSD analysis in **Figure 4.31** agrees with these observations. **Figure 4.31** highlights the effect of hydrogen on the morphology and phase constitution of samples that were deformed and annealed at 900ºC.

Prior to the deformation at 900ºC, the initial sample conditions were: **(see Figure 4.28)**

- As hydrogenated (H) - **(Figure 4.31** images **a, c, e)**.
- Hydrogenated and dehydrogenated (HD) - **(Figure 4.31** images **b, d, f)**.

After deformation and quenching the samples were reheated and recrystallised at 900ºC.

In **Figure 4.31**, images a)-f) show that samples deformed at 900ºC do not recrystallise at 900ºC. Images a), c) and e) show that the prior hydrogenated (H) sample has needle morphology in a retained beta matrix. On the contrary, images b), d) and f) show that the prior dehydrogenated (HD) sample has Widmanstätten morphology and less indexed bcc phase.

In **Figure 4.31**, images a), c) and e) show that upon quenching the hydrogenated sample, a bcc to hcp needle martensite transformation occurred. The alloyed hydrogen acted as a beta stabiliser and retained some of the high temperature bcc phase at room temperature.

The dehydrogenated sample shown in **Figure 4.31**, images b), d) and f) has no hydrogen to neither lower its beta transus nor decrease the critical cooling rate for martensite formation. The quenching temperature (900ºC) was an alpha plus beta region in dehydrogenated Ti6Al4V. Therefore, quenching from the alpha plus beta region retained the primary lamellar alpha. **Figure 4.31 f)** shows less amount of indexed beta phase when compared to **Figure 4.31 e)**. This is because there was no hydrogen in **Figure 4.31 f)** to stabilise some of the beta as retained metastable beta upon quenching.

Contrary to **Figure 4.31**, recrystallisation occurred at 900ºC on samples that were deformed at lower temperatures (550ºC), this is shown in **Figure 4.32**.

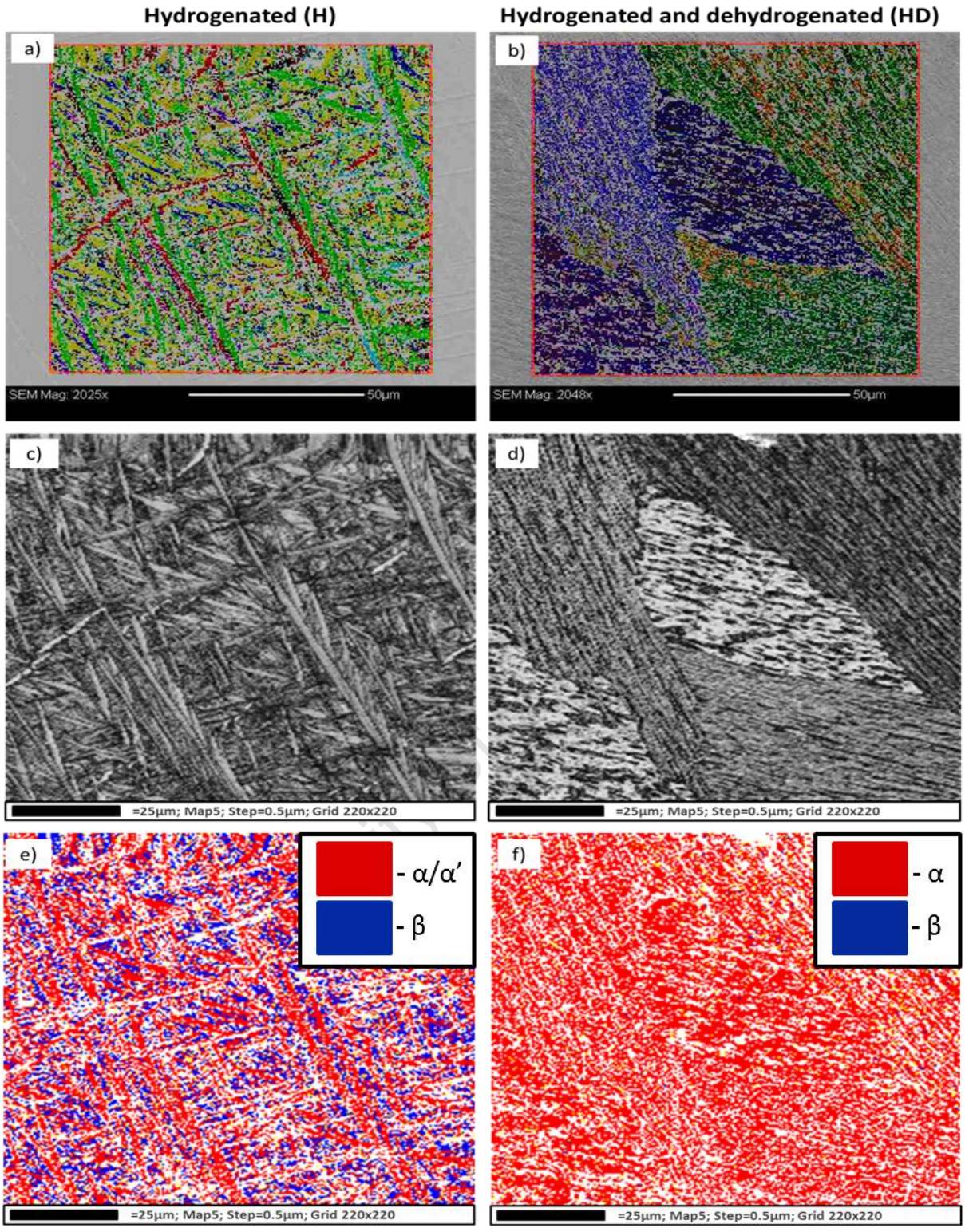

Figure 4.31: *The scanned regions (a, b), band contrast (c, d) and phase maps (e, f) of samples deformed and recrystallised at 900°C. Images (a, c, e) were prior hydrogenated (H) whilst images (b, d, f) were prior hydrogenated and dehydrogenated (HD). In images e), f), red is hcp, blue is bcc and non-indexed regions are white.*

In **Figure 4.32**, images a)-f) represent two samples that were that were deformed at 550ºC and recrystallised for 15 minutes at 900ºC (a, c, e) or 850ºC (b, d, f). The grain boundaries are defined by a minimum misorientation angle of 15 degrees.

In **Figure 4.32 a)-f)**, the recrystallised grain size decreases with decreasing recrystallisation temperature from 900ºC (images a, c, e) to 850ºC (images b, d, f). Images a)-f) show recrystallised samples that have an equiaxed bcc grain structure. The bcc grains have needle hcp morphology because bcc transformed to hcp martensite upon quenching from 900ºC. The coexistence of beta and hexagonal martensite in a quenched Ti-V-Al alloy that has a high amount of beta stabilisers was also observed by Sato et al. [49, 57]

Davies et al. [50] argued that the observed beta phase is retained on quenching. In addition, the amount of retained beta could also be enhanced by the stabilising effect of hydrogen on the beta phase. This is clearly proven in **Figure 4.31 f)** where the absence of hydrogen caused no needle hcp formation and no retained beta.

In-situ dilatometry in Abbas [48] shows that above 15 at.% H, the Ti6Al4V alloy is fully beta at 920ºC. The equiaxed bcc structure in **Figure 4.32** images (a-f) shows that the samples had a fully bcc structure at both recrystallisation temperatures namely 900ºC (images a, c, e) and 850ºC (images b, d, f). Therefore, at 20±3 at.% H the beta transus is estimated to be below 850ºC.

The α/β balance and the phase constitution in **Figure 4.32 a), c), e)** is consistent with the condition shown in **Figure 4.13 a), b)**. In both cases, the hydrogenated sample was quenched from 900ºC. Even though considerable grain refinement (formation of equiaxed grain structure) has occurred in **Figure 4.32 a), c), e)** when compared to **Figure 4.13 a), b)**, they both show consistency in terms of their phase evolution.

The beta phase retained upon quenching is metastable because it decomposes to needle hcp when aged at 580ºC **(see Figure 4.33)**.

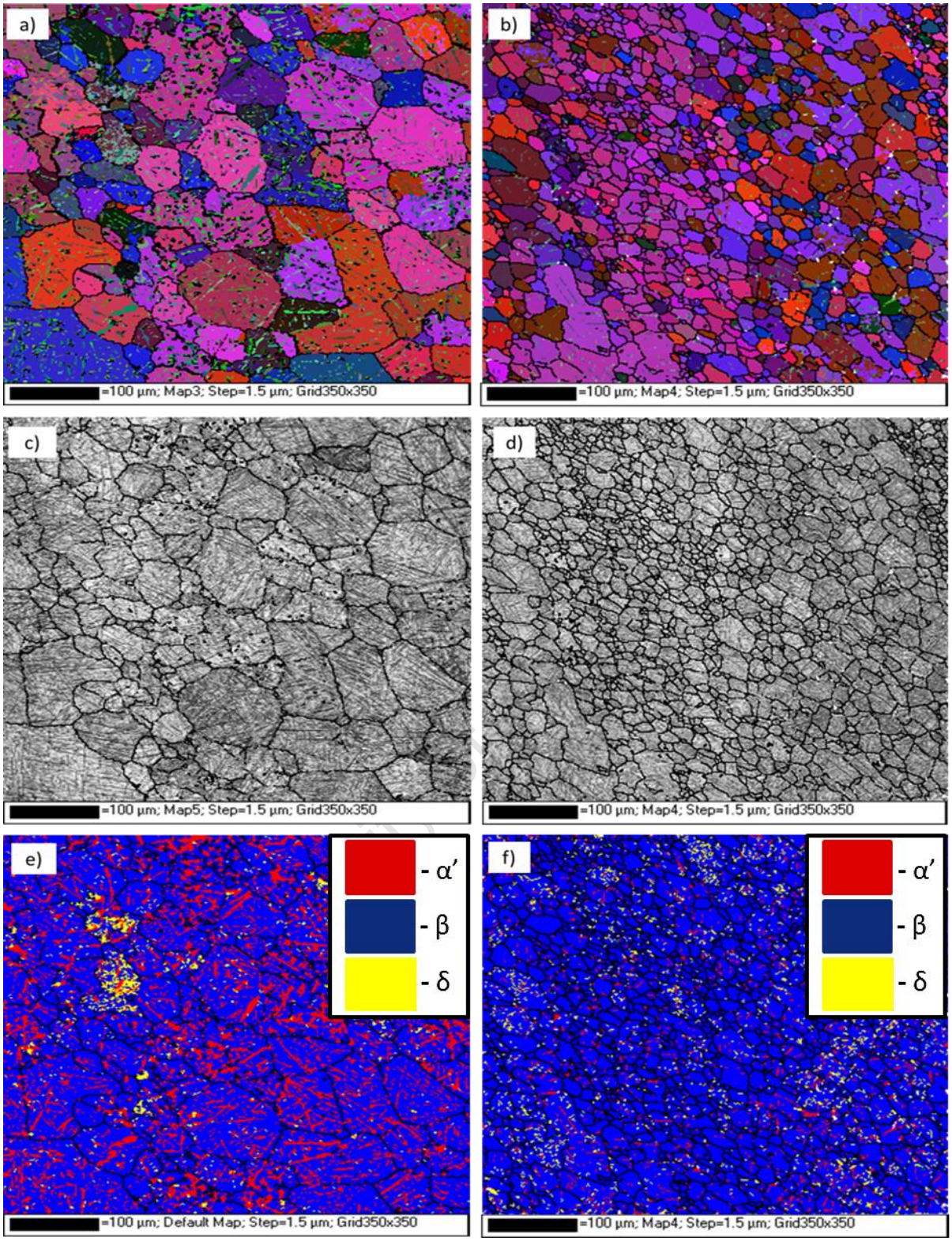

Figure 4.32: *The Euler color (a, b), band contrast (c, d) and phase maps (e, f) of two samples deformed at 550°C, recrystallised at 900°C (images a, c, e) or 850°C (images b, d, f) for 15 minutes and quenched. In images e), f), blue is bcc, red is hcp and yellow is hydride phase.*

4.9.2 Metastable phase decomposition

The deformed (at 550°C) and recrystallised (at 850°C for 15 minutes) sample in **Figure 4.32 (b, d, f)** was aged at 580°C for 3 hours and quenched. The EBSD analysis of the aged sample is shown in **Figure 4.33.** Aging decomposed the metastable bcc phase in **Figure 4.32 f)** to form the needle hcp structure in **Figure 4.33 c)**. This further decomposed during dehydrogenation to form an ultrafine equiaxed microstructure **(see Figure 4.34)**.

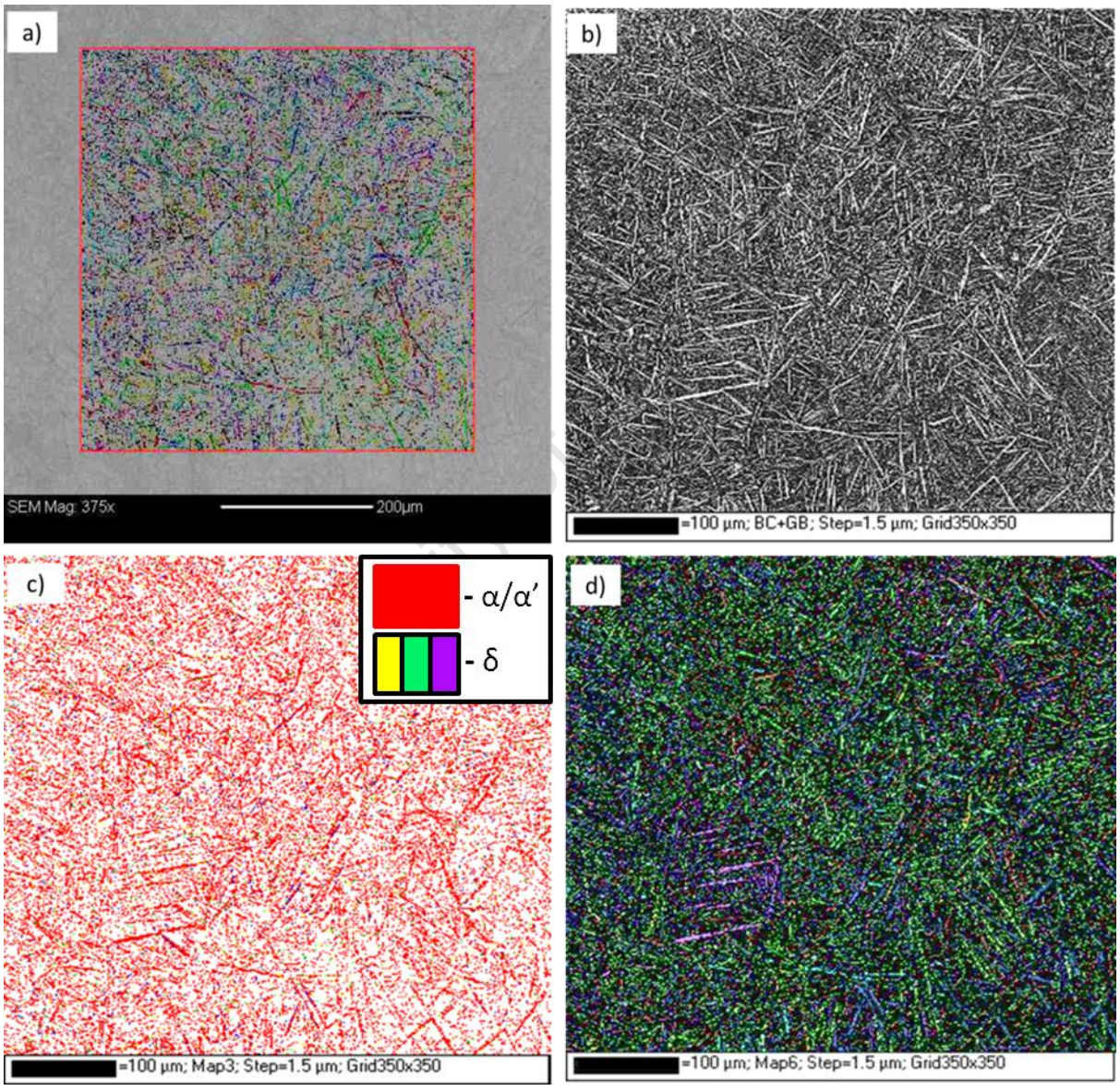

Figure 4.33: *The a) scanned region, b) band contrast, c) phase and d) Euler color maps of a sample deformed at 550°C recrystallised at 850°C for 15 minutes and metastable phase decomposed at 580°C for 3 hours. In image c), red is hcp, blue is bcc, yellow, green and purple are forms of hydride phase and non-indexed regions are white.*

4.9.3 Hydride decomposition

The deformed (at 550°C), recrystallised (at 850°C for 15 minutes) and aged (at 580°C for 3 hours) sample in **Figure 4.33** was dehydrogenated at 675°C for 2 hours. The EBSD results of the dehydrogenated sample are shown in **Figure 4.34.** In **Figure 4.34 a)-f)**, images a), c), e) and b), d), f), are low and high magnification images of the same sample respectively. Grain boundaries are defined by a minimum misorientation angle of 15 degrees. In **Figure 4.34**, a) and b) are SEM images showing the EBSD scanned regions highlighted in red.

Upon dehydrogenation of the aged sample, the needle microstructure in **Figure 4.33 b)** decomposed to form the ultrafine equiaxed microstructure **Figure 4.34** (images c, d). The phase analysis of the ultrafine microstructure in **Figure 4.34 e)** shows that only hcp (red) and bcc (blue) phases are present after dehydrogenation**.** This means that hydrogen was removed and hydrogen induced phases decomposed to form the ultrafine structure of equilibrium alpha and beta phases.

In summary, dehydrogenation decomposes hydrogen induced phases to form a refined microstructure of equilibrium alpha and beta phases. Hydrogen is released upon the decomposition of saturated alpha (α_H) and beta (β_H) phases. Refinement occurs because hydrogen induced phases form homogenously dispersed dislocations which act as nucleation points [53, 58] for fine grains. During decomposition, fine alpha and beta grains nucleate on these homogeneously dispersed dislocations to form the ultrafine equiaxed microstructure. The phase transformations that occur during dehydrogenation are therefore:

i. $\beta_H \rightarrow \beta + H_2 \uparrow$

ii. $\alpha_H \rightarrow \alpha + H_2 \uparrow$

iii. $\delta \rightarrow \alpha + H_2 \uparrow$

The grain size analysis of the refined microstructure is discussed in **Section 4.10**.

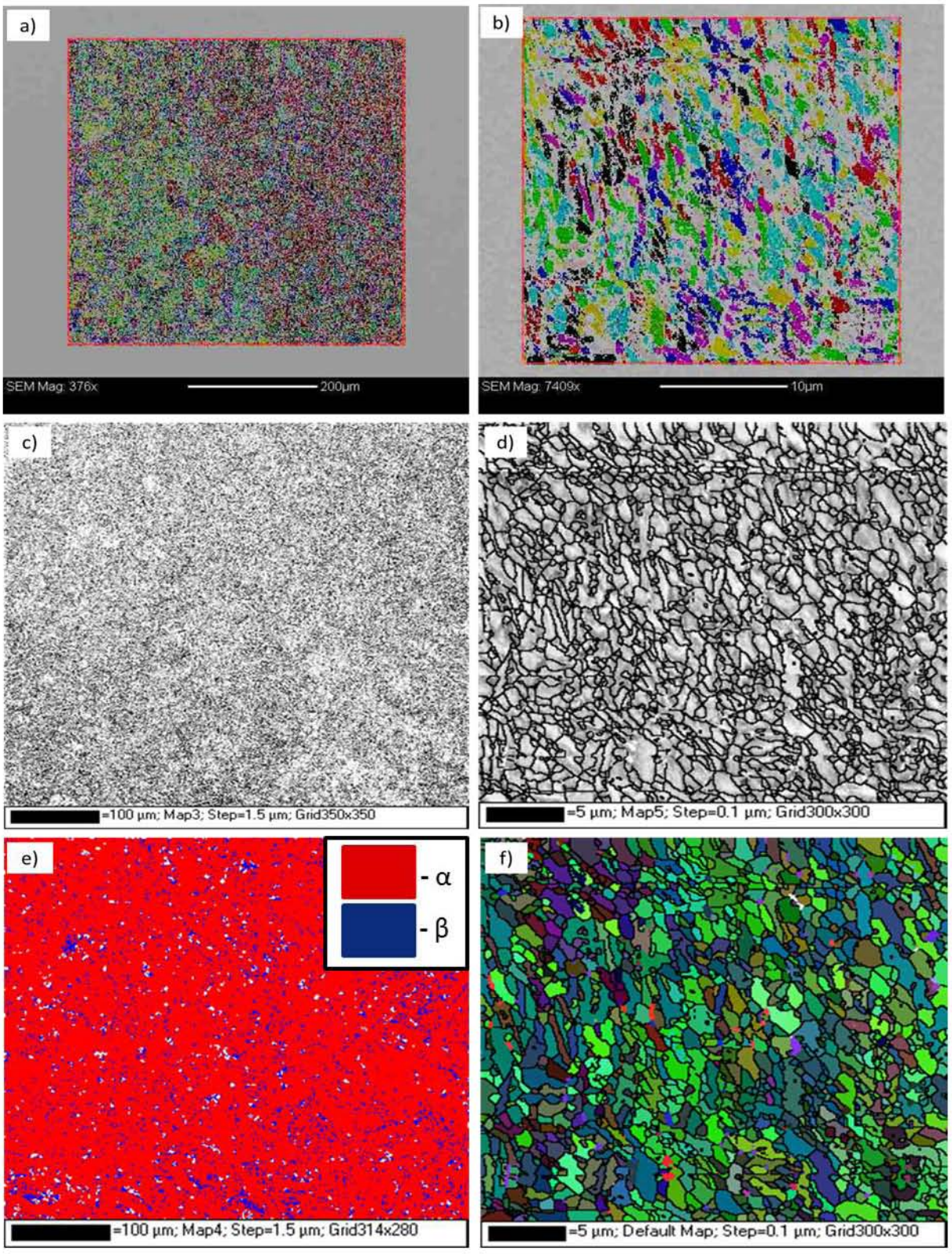

Figure 4.34: *The (a, b) scanned regions, (c, d) band contrast, e) phase and f) Euler color maps of a sample recrystallised at 850°C, metastable phase decomposed and dehydrogenated at 675°C for 2 hours. In image e), red is hcp, blue is bcc and non-indexed regions are white.*

4.10 The refined microstructure

Figure 4.35 shows a sample deformed at 550°C, recrystallised at 850°C for 15 minutes, aged at 580°C for 3 hours and dehydrogenated at 675°C for 2 hours. The SEM images show equiaxed beta (light phase) in a darker alpha matrix. The grain sizes of the refined microstructure are defined by a minimum misorientation angle of 15 degrees. The histogram in **Figure 4.35 c)** was plotted using data from the high magnification images in **Figures 4.34 b), d), f)**. In **Figure 4.35 c)**, the grain diameters range from 0.1 µm to 3 µm. Within this range, a greatest percentage of the grains are between 0.1µm–1µm in diameter.

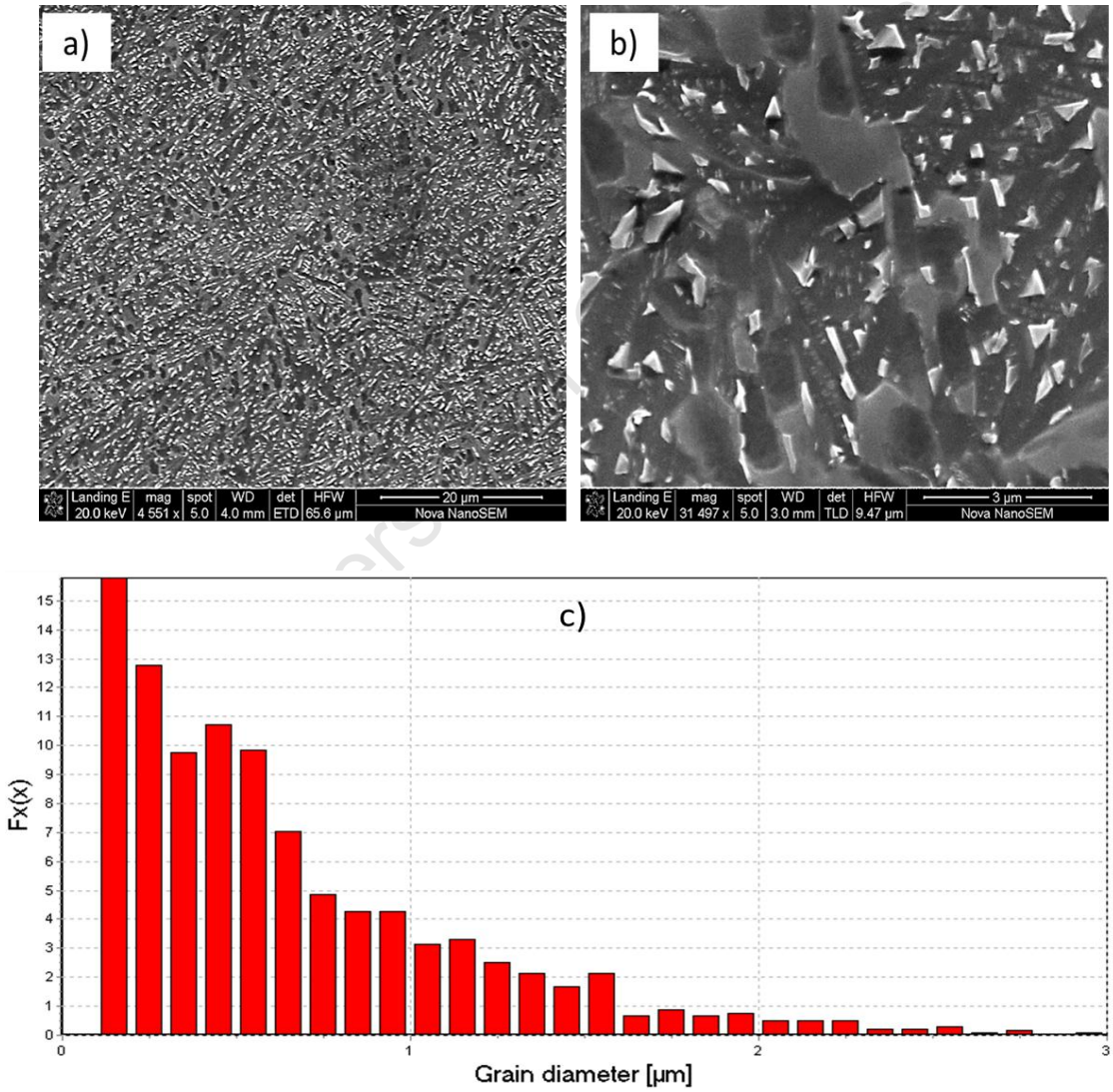

Figure 4.35: *The refined microstructure`s a)-b) SEM micrographs and c) grain size distribution histogram at a class width of 0.1 µm.*

4.11 Summary of findings

Two methods of refinement (method A and method B) were explored in this study as shown in **Figure 4.36**. Method A and B both have a hydrogenation step, they differ in that after hydrogenation method A has a solution treatment and phase decomposition step. Method B on the other hand has deformation and post deformation annealing steps after hydrogenation.

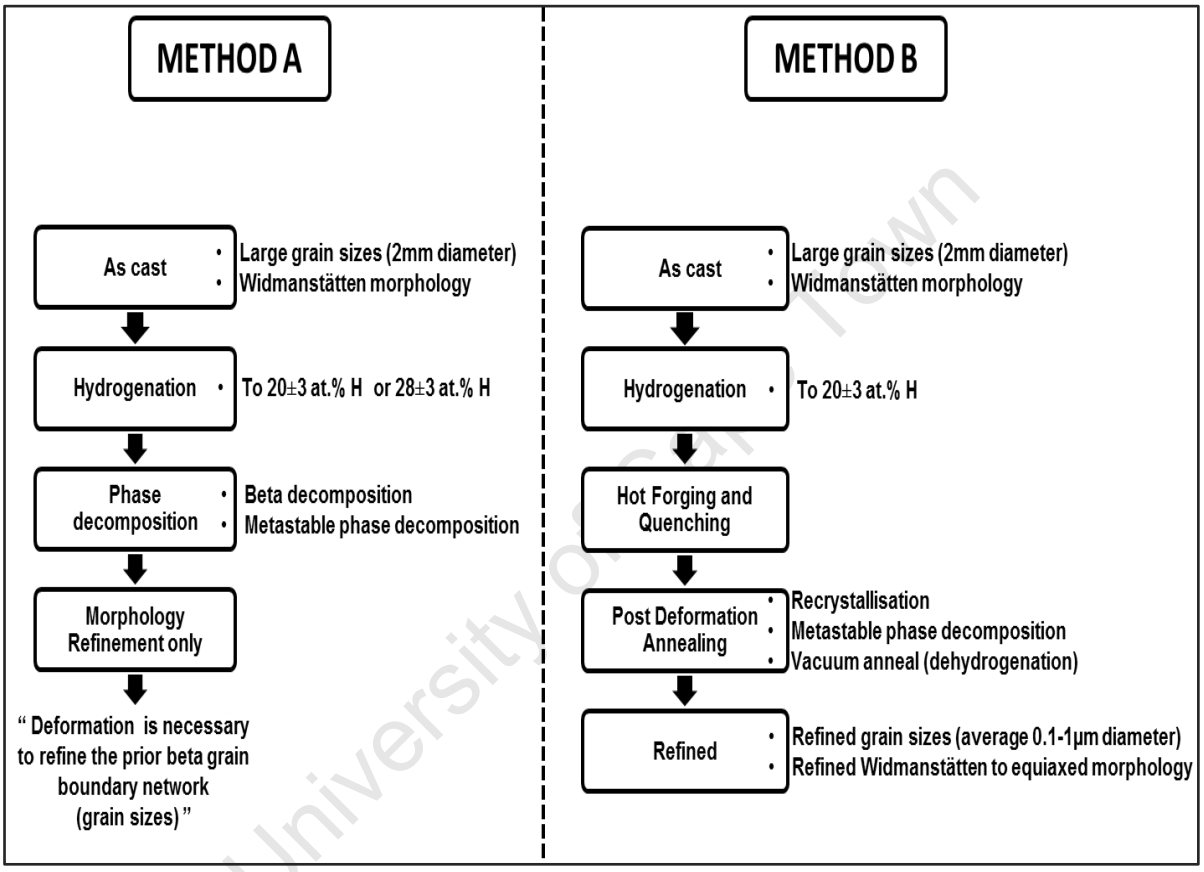

Figure 4. 36: *A summary of findings obtained from exploring two methods of refinement, one excluding deformation (method A) and the other including deformation (method B).*

It was found that method A refined the morphology only whilst method B refined both the morphology and the prior beta grain boundary network. The next two pages highlight a summary of the findings of each processing step in methods A and B.

Method A and B: As cast Ti6Al4V (Section 4.2)

The starting material (as cast Ti6Al4V) has large prior beta grain sizes that are about 2mm in diameter. It also has a predominant Widmanstätten alpha morphology.

Method A and B: Hydrogenation (Section 4.3)

A larger amount of hydrogen is absorbed at lower hydrogenation temperatures. This is further highlighted by the hydride related cracking of that occurs at hydrogenation temperature 550°C. Lesser hydrogen is absorbed at higher hydrogenation temperatures and this can be attributed to increased oxide activity at these temperatures which hinders hydrogen absorption. XRD peak overlaps cause difficulties in identifying individual phases that form after hydrogenating Ti6Al4V. However, XRD peak broadening and reduction of peak intensities confirm that hydrogen is dissolved in solid solution and hydrides form. There is no significant relationship between hydrogenation temperature and hardness. However, minor hardness peaks occur at lower hydrogenation temperatures; these indicate the high amount of harder hydride phase that forms at these temperatures.

Method A: Beta decomposition (Section 4.4)

In hydrogenated Ti6Al4V, saturated beta decomposes to alpha and hydride. The hydride formation results to an increase in hardness. Beta decomposition to alpha and hydride is most prominent at lower isothermal anneal temperatures. If hydrogenated Ti6Al4V is solution treated and isothermally decomposed at 700°C, 600°C or 500°C, more hydrides will form at the 500°C condition. Therefore, the 500°C condition will have the largest hardness increase when compared to the 600°C or 700°C conditions. This is because beta is more stable at higher temperatures (700°C and 600°C), therefore less beta decomposition occurs at these temperatures when compared to 500°C.

Method A: Metastable phase decomposition (Section 4.5)

Solution treating and quenching Ti6Al4V hydrogenated to 20±3 at.% H forms hexagonal martensite and retained metastable beta. Hydrogen stabilises some of the high temperature beta phase as retained metastable beta phase. Upon aging, the metastable beta decomposes to form saturated alpha and hydrides and this increases the hardness.

Method A: Comments on refinement (Section 4.6)

After hydrogenating, solution treating and beta or metastable phase decomposition the morphology is refined but the prior beta grain boundary network is not refined. Deformation and recrystallisation is required to refine prior beta grain boundary network.

Method B: Deformation and quenching (Sections 4.7-4.8)

Hydrogen improves the deformability by reducing the lowest temperature at which Ti6Al4V can be successfully deformed without cracking specimens. This is because hydrogen stabilises the softer and more deformable beta phase at lower temperatures. This is manifested in the reduction of the hot compression flow stresses at these lower temperatures (800°C and 900°C). At higher temperatures (1000°C) where more beta phase is present, the effect of hydrogen on the flow stress becomes less significant. Low temperature deformation increases the stored deformation energy.

Method B: Post Deformation annealing (Section 4.9)

A larger amount of stored deformation energy enables for low temperature recrystallisation. Recrystallising at lower temperatures results in finer prior beta grain sizes because the grain growth exponents are lower at these temperatures. Upon quenching, beta transforms to martensite and hydrogen stabilises some of the beta phase at room temperature as retained metastable beta. This further decomposes during aging to form alpha and hydrides. When hydrogen is finally removed during vacuum annealing, the hydrides decompose to form equilibrium alpha and beta phases. The nucleation and growth associated with the decomposition of the hydrogen induced phases causes refinement and it results to an ultrafine equiaxed microstructure.

5. CONCLUSIONS

i. The grain size and the morphology of as cast Ti6Al4V can be successfully refined by combining thermohydrogen processing and hot forging.
   - The grain size was successfully refined from an average diameter of 2 mm (2000μm) to the diameter range of 0.0001 mm to 0.003 mm (0.1 μm-3 μm).
   - The morphology was successfully refined from Widmanstätten to equiaxed.

ii. Hydrogen alloying improved the hot deformability of Ti6Al4V. As cast Ti6Al4V can be successfully deformed at temperatures of 900°C and above. Alloying with 20±3 at.% H reduced this deformation limit from 900°C to 550°C.

iii. The alloyed 20±3 at.% H caused a 35% reduction in peak flow stress at 800°C, 25% reduction at 900°C and no reduction at 1000°C. Hydrogen softening decreased with increasing deformation temperature. There was no hydrogen softening at 1000°C where a single phase beta region existed.

iv. Deforming at lower temperatures (550°C) reduced the minimum temperature required to recrystallise grains from 1100°C to 800°C. Deforming and recrystallising at lower temperatures resulted in finer grain sizes.

v. Hydrogenation forms hydrides. A greater amount of hydrogen is absorbed at lower hydrogenation temperatures (650°C). There is no significant relationship between hydrogenation temperature and hardness. However hardness peaked at the temperature at which a greater amount of hydrogen was absorbed.

vi. Beta decomposition and metastable phase decomposition refines the microstructure morphology. Deformation is required to eliminate the prior beta grain boundary network.

vii. Quenching Ti6Al4V hydrogenated to 20±3 at.% H from temperatures 850°C and 900°C formed a needle hcp martensite structure in a retained metastable beta matrix. In addition, hydrogen stabilised more high temperature bcc phase at room temperature as a metastable bcc phase upon quenching. Beta and hexagonal martensite are softer than the equilibrium alpha phase. Therefore aging hydrogenated and quenched samples decomposed the metastable beta and 'softer' martensite phases to form the `harder` equilibrium alpha phase. In doing so, the hardness increased during martensite decomposition.

viii. Dehydrogenation removed hydrogen and decomposed hydrides. Hydrides decompose to form ultrafine equiaxed alpha and beta phases.

ix. The microstructure evolved from Widmanstätten morphology, to martensitic needle morphology after recrystallisation and aging. The hexagonal martensite decomposed to form equiaxed equilibrium alpha and beta after dehydrogenation. This resulted in a new equiaxed morphology that successfully eliminated the prior beta grain boundary network.

6. FUTURE WORK

Despite the amount of experimental data that is available, the mechanisms of grain refinement are still not understood by researchers. There is no generally accepted mechanism of refinement of hydrogenated and deformed Ti6Al4V. Therefore this remains a puzzle for researches to solve. The following recommendations are made to improve the understanding of the microstructure refining mechanisms in hydrogenated and deformed Ti6Al4V:

- TEM and FIB-SEM studies must be done to accurately characterise the microstructure refining phase transformations and the mechanisms of refinement throughout the microstructure refining process.
- Light element analysis must be used to support the mass measurements in measuring the amount of absorbed hydrogen.

Industrial Processing Recommendation:

- In industry, ultrafine grain sizes of 1μm are obtained through superplastic deformation which utilizes very high true strains in the range of 4 to 8. Similar grain sizes are obtainable through the use of hydrogen as a temporal alloying element at comparatively lower true strains of 1.6.

7. REFERENCES

1. M. J. Donachie: 'Castings', in 'Titanium: A Technical Guide', 2nd edn, 39-46; 2000, Materials Park, OH, ASM International. (e-book, available at [http://books.google.co.za/books?id=HgzukknbNGAC&pg=PA43&lpg=PA43&dq=Castings%27,+in+%27Titanium:+A+Technical+Guide&source=bl&ots=K_31gi7C_K&sig=OTYr94gq6aOEAlOVAps1rbFl_tw&hl=en&sa=X&ei=M8cHUdL-BY-FhQeD-oD4Dg&ved=0CEoQ6AEwBA])

2. C. Leyens and M. Peters: 'Titanium and titanium alloys: fundamentals and applications'; 2003, Weinheim, Germany, Wiley-VCH.

3. G. Raghuveer: 'Effect of boron and hydrogen on microstructure and mechanical properties of cast Ti-6Al-4V', Licentiate thesis, Lulea University of Technology, Lulea, 2011.

4. I. Katzarov, S. Malinov, and W. Sha: 'Finite Element Modeling of the Morphology of β to α Phase Transformation in Ti-6Al-4V Alloy', *Metall. Mater. Trans. A*, 2002, **33A**, 1027-1040.

5. F. J. Gil, M. P. Ginebra, J. M. Manero, and J. A. Planell: 'Formation of α-Widmanstätten structure: effects of grain size and cooling rate on the Widmanstätten morphologies and on the mechanical properties in Ti6Al4V alloy', *J. Alloys Compd.*, 2001, **329**(1-2), 142-152.

6. S. L. Semiatin: 'Introduction to Bulk-Forming Processes', in 'ASM International', Vol. 14A, 'Metalworking: bulk forming', (ed. ASM International); 2005, Materials Park, OH, ASM International. (e-book, available at [http://www.asminternational.org/content/ASM/StoreFiles/6957_01A_WEB2a.pdf])

7. V. Goltsov: 'Hydrogen treatment (processing) of materials: current status and prospects', *J. Alloys Compd.*, 1999, **293**, 844-857.

8. D. G. Lee, S. Kim, S. Lee, and C. S. Lee: 'Effects of microstructural morphology on quasi-static and dynamic deformation behavior of Ti-6Al-4V alloy', *Metall. Mater. Trans. A*, 2001, **32**(2), 315-324.

9. M. Benedetti and V. Fontanari: 'The effect of Bi-modal and lamellar microstructures of the Ti6Al4V behaviour of fatigue cracks emanating from edge-notches', *Fatigue and fracture engineering of materials and structures*, 2004, **27**(11), 1073-1089.

10. A. Guitar, G. Vigna, and M. I. Luppo: 'Microstructure and tensile properties after thermohydrogen processing of Ti-6Al-4V', *J. Mech. Behav. Biomed. Mater.*, 2009, **2**(2), 156-163.

11. R. Ding, Z. X. Guo, and A. Wilson: 'Microstructural evolution of a Ti-6Al-4V alloy during thermomechanical processing', *Mater. Sci. Eng., A*, 2002, **327**(2), 233-245.

12. S. Tamirisakandala, R. Bhat, and B. Vedam: 'Recent advances in the deformation processing of titanium alloys', *J. Mater. Eng. Perform.*, 2003, **12**(6), 661-673.

13. X. Li, S. Q. Lu, M. W. Fu, K. L. Wang, and X. J. Dong: 'The optimal determination of forging process parameters for Ti-6.5Al-3.5Mo-1.5Zr-0.3Si alloy with thick lamellar microstructure in two phase field based on P-map', *J. Mater. Process. Technol.*, 2010, **210**(2), 370-377.

14. R. D. Doherty, D. A. Hughes, F. J. Humphreys, J. J. Jonas, D. J. Jensen, M. E. Kassner, W. E. King, T. R. McNelley, H. J. McQueen, and A. D. Rollett: 'Current issues in recrystallization: a review', *Mater. Sci. Eng., A*, 1997, **238**(2), 219-274.

15. S. Semiatin, R. Goetz, V. Seetharaman, E. Shell, and A. Ghosh: 'Cavitation and failure during hot forging of Ti-6Al-4V', *Metall. Mater. Trans. A*, 1999, **30**(5), 1411-1424.

16. X. Li, S. Q. Lu, M. W. Fu, K. L. Wang, and X. J. Dong: 'The optimal determination of forging process parameters for Ti-6.5Al-3.5Mo-1.5Zr-0.3Si alloy with thick lamellar microstructure in two phase field based on P-map', *Journal of Materials Processing Technology*, **210**(2), 370-377.

17. A. Momeni and S. M. Abbasi: 'Effect of hot working on flow behavior of Ti-6Al-4V alloy in single phase and two phase regions', *Mater. Des.*, 2010, **31**(8), 3599-3604.

18. J. Luo, M. Li, W. Yu, and H. Li: 'Effect of the strain on processing maps of titanium alloys in isothermal compression', *Mater. Sci. Eng., A*, 2009, **504**(1-2), 90-98.

19. J. Yeom*, J. H. Kim, J. Hong, N. Park, and C. S. Lee: 'Influence of initial microstructure on the hot workability of Ti6Al4V alloy', *Int. J. Mod Phys B*, 2009, **23**(6-7), 808-813.

20. T. Seshacharyulu, S. C. Medeiros, W. G. Frazier, and Y. V. Prasad: 'Hot working of commercial Ti-6Al-4V with an equiaxed α + β microstructure: materials modeling considerations', *Mater. Sci. Eng., A*, 2000, **284**(1-2), 184-194.

21. T. Seshacharyulu, S. C. Medeiros, W. G. Frazier, and Y. V. Prasad: 'Microstructural mechanisms during hot working of commercial grade Ti-6Al-4V with lamellar starting structure', *Mater. Sci. Eng., A*, 2002, **325**(1-2), 112-125.

22. M. Li and W. Zhang: 'Effect of hydrogenation content on high temperature deformation behavior of Ti-6Al-4V alloy in isothermal compression', *Int. J. Hydrogen Energy*, 2008, **33**(11), 2714-2720.

23. N. Park, J. Yeom, and Y. Na: 'Characterization of deformation stability in hot forging of conventional Ti-6Al-4V using processing maps', *J. Mater. Process. Technol.*, 2002, **130-131**, 540-545.

24. H. J. Front and M. E. Ashby: 'Deformation Mechanisms and Deformation-Mechanism Maps', in 'Deformation-Mechanism Maps: the plasticity and creep of metals and ceramics', 1 edn, 1982, New York, Pergamon Press.

25. R. Raj: 'Development of a Processing Map for Use in Warm-Forming and Hot-Forming Processes', *Metall. Mater. Trans. A*, 1981, **12**(6), 1089-1097.

26. V. K. Nosov, A. V. Ovchinnikov, and Y. Y. Shchugorev: 'Applications of hydrogen plasticizing of titanium alloys', *Met. Sci. Heat Treat.*, 2008, **50**(7-8), 378-382.

27. J. C. Oguh: 'Investigations of the micro structural evolution in Ti6Al4V alloy during cyclic hydrogenation and dehydrogenation heat treatment', MSc thesis, University of Cape Town, Cape Town, 2008.

28. F. H. Froes, O. N. Senkov, and J. I. Qazi: 'Hydrogen as a temporary alloying element in titanium alloys: thermohydrogen processing', *Int. Mater. Rev.*, 2004, **49**(3-4), 227-245(219).

29. J. Zhao, H. Ding, W. Zhao, X. Tian, H. Hou, and Y. Wang: 'Influence of hydrogenation on microstructures and microhardness of Ti6Al4V alloy', *Trans. Nonferrous Met. Soc. China*, 2008, **18**(3), 506-511.

30. R. J. Wasilewski and G. L. Kehl: 'Diffusion of Hydrogen in Titanium', *Metallurgica*, 1954, **50**, 225-230.

31. A. Lopez-Suarez, J. Rickards, and R. Trejo-Luna: 'Analysis of hydrogen absorption by Ti and Ti-6Al-4V using the ERDA technique', *Int. J. Hydrogen Energy*, 2003, **28**(10), 1107-1113.

32. L. Matthews and R. D. Knutsen: 'Embrittlement of the Ti-6Al-4V alloy by hydrogen dosing at elevated temperatures', *SAIMM*, 2010, **111**, 155-158.

33. W. R. Kerr: 'The effect of hydrogen as a temporary alloying element on the microstructure and tensile properties of Ti-6Al-4V', *Metall. Mater. Trans. A*, 1985, **16**(6), 1077-1087.

34. A. A. Ilynn, B. A. Kolachev, and A. M. Mamonov: 'Phase and structure transformations in titanium alloys under thermohydrogenous treatment', *Titanium '92: Sci. Technol., Proc. Symp.*, 1992, **1**, 941-947.

35. J. Qazi, J. Rahim, F. Froes, O. Senkov, and A. Genc: 'Phase transformations in Ti-6Al-4V-x H alloys', *Metall. Mater. Trans. A*, 2001, **32**(10), 2453-2463.

36. M. Niinomi, B. Gong, T. Kobayashi, Y. Ohyabu, and O. Toriyama: 'Fracture characteristics of Ti-6Al-4V and Ti-5Al-2.5Fe with refined microstructure using hydrogen', *Metall. Mater. Trans. A*, 1995, **26**(5), 1141-1151.

37. T. Fang and W. Wang: 'Microstructural features of thermochemical processing in a Ti-6Al-4V alloy', *Mater. Chem. Phys.*, 1998, **56**(1), 35-47.

38. J. Zhao, H. Ding, Y. Zhong, and C. S. Lee: 'Effect of thermo hydrogen treatment on lattice defects and microstructure refinement of Ti6Al4V alloy ', *Int. J. Hydrogen Energy*, 2010, **35**(12), 6448-6454.

39. L. Luo, Y. Su, J. Guo, and H. Fu: 'Formation of titanium hydride in Ti-6Al-4V alloy', *J. Alloys Compd.*, 2006, **425**(1-2), 140-144.

40. D. B. Shan, Y. Y. Zong, Y. Lv, and B. Guo: 'The effect of hydrogen on the strengthening and softening of Ti-6Al-4V alloy', *Scripta Mater.*, 2008, **58**(6), 449-452.

41. D. B. Shan, Y. Y. Zong, T. F. Lu, and Y. Lv: 'Microstructural evolution and formation mechanism of FCC titanium hydride in Ti-6Al-4V-xH alloys', *J. Alloys Compd.*, 2007, **427**(1-2), 229-234.

42. C. C. Shen, C. Y. Yu, and T. P. Perng: 'Variation of structure and mechanical properties of Ti-6Al-4V with isothermal hydrogenation treatment', *Acta Mater.*, 2009, **57**(3), 868-874.

43. C. T. Liu, T. I. Wu, and J. K. Wu: 'Formation of nanocrystalline structure of Ti-6Al-4V alloy by cyclic hydrogenation-dehydrogenation treatment', *Mater. Chem. Phys.*, 2008, **110**(2-3), 440-444.

44. J. I. Qazi, O. N. Senkov, J. Rahim, and F. H. Froes: 'Kinetics of martensite decomposition in Ti-6Al-4V-xH alloys', *Mater. Sci. Eng., A*, 2003, **359**(1-2), 137-149.

45. J. Qazi, J. Rahim, O. Senkov, and F. Froes: 'Phase transformations in the Ti-6Al-4V-H system', *J. Mater.*, 2002, **54**(2), 68-71.

46. J. Lu, J. Qin, W. Lu, Y. Chen, D. Zhang, and H. Hou: 'Hot deformation behavior and microstructure evaluation of hydrogenated Ti-6Al-4V matrix composite', *Int. J. Hydrogen Energy*, 2009, **34**(22), 9266-9273.

47. L. Matthews: 'Optimisation of the oxygen diffusion process for surface hardening of the Ti6Al4V alloy', MSc thesis, University of Cape Town, Cape Town, 2008.

48. N. Abbas: 'Analysis of phase transformations in hydrogenated titanium metals by non-isothermal dilatometry', MSc thesis, University of Cape Town, Cape Town, 2011.

49. K. Sato, H. Matsumoto, A. Chiba, and T. J. Konno: ' Microstructure evolution and age-hardening of hexagonal α' martensite in Ti-12mass%V-2mass%Al alloys on annealing', *The 15th European Microscopy Congress*, Manchester Central, United Kingdom, September 2012.

50. R. Davis, H. Flower, and D. West: 'The decomposition of Ti-Mo alloy martensites by nucleation and growth and spinodal mechanisms', *Acta Metall.*, 1979, **27**(6), 1041-1052.

51. Y. Zhang and S. Q. Zhang: 'Hydrogenation characteristics of Ti6Al4V cast alloy and its microstructural modification by hydrogen treatment', *Int. J. Hydrogen Energy*, 1997, **22**(2), 161-168.

52. H. Fujii: 'Strengthening of α+β titanium alloys by thermomechanical processing', *Mater. Sci. Eng., A*, 1998, **243**(1-2), 103-108.

53. H. Yoshimura and J. Nakahigashi: 'Ultra-fine-grain refinement and superplasticity of titanium alloys obtained through protium treatment', *Int. J. Hydrogen Energy*, 2002, **27**(7-8), 769-774.

54. Y. Y. Zong, D. B. Shan, Y. Lü, and B. Guo: 'Effect of 0.3 wt.%H addition on the high temperature deformation behaviors of Ti6Al4V alloy', *Int. J. Hydrogen Energy*, 2007, **32**(16), 3936-3940.

55. Y. Niu, M. Li, H. Hou, Y. Wang, and Y. Lin: 'High temperature deformation behavior of Ti6Al4V alloy without and with hydrogen content of 0.27 wt.%', *J. Mater. Eng. Perform.*, 2010, **19**(1), 59-63.

56. W. D. Callister and D. G. Rethwisch: 'Fundamentals of materials science and engineering: an integrated approach', 2011, Weinheim, Germany, Wiley-VCH.

57. K. Sato, H. Matsumoto, K. Kodaira, T. J. Konno, and A. Chiba: 'Phase transformation and age-hardening of hexagonal α′ martensite in Ti-12mass% V-2mass% Al alloys studied by transmission electron microscopy', *J. Alloys Compd.*, 2010, **506**(2), 607-614.

58. M. A. Murzinova, G. A. Salishchev, and D. D. Afonichev: 'Formation of nanocrystalline structure in two-phase titanium alloy by combination of thermohydrogen processing with hot working', *Int. J. Hydrogen Energy*, 2002, **27**(7-8), 775-782.

8. APPENDIX

A: Formula used in calculating atomic percent absorbed hydrogen from mass gain

Hydrogenated sample mass(g) (m_1)	0.99
(-) Initial sample mass(g) (m_0)	0.98
Mass gain(g) (mass of absorbed hydrogen)(m_H)	0.01

Composition (90% Ti- 6%Al- 4%V-xH)	**Units**	**0.9 Ti**	**0.06 Al**	**0.04 V**	**xH**	$\sum$ ***of rows***
Molecular mass (mr)	g/mol	47.86	26.98	50.94	1.00	-
Calculation of mass of elements in Ti6Al4VxH	g	0.90 x m_0	0.06 x m_0	0.04 x m_0	m_H	-
Row A = mass of elements in Ti6Al4VxH	g	0.88	0.06	0.04	0.01	0.99
Row B = ((row A/ $\sum of\ row\ A$) x 100)	wt.%	89.09	5.94	3.96	1.01	100.00
Row C = (row B/mr)	-	1.86	0.22	0.08	1.00	3.16
Row D =((row C)/($\sum of\ row\ C$)) x 100	at.%	58.88	6.96	2.46	31.70	100.00

B: GSL Code used for deformation, recrystallisation and quenching

```
// Setup:
// Jaw tempco set to 0.0000um/C, specimen tempco set to 60.0000nm/mm/C
//
set rampterm to 24000pct
set ramiterm to 0pct
set ramdterm to 120pct
// Heating...
// Hydrawedge Auto-load

// stress/strain setup...
set strainmode to 1
set strainsrc to Jaw.index
set strainX0 to 12.00mm
set strVolume to 10.00mm*10.00mm*0.7853975*12.00mm
// end of stress/strain setup.

acquire Jaw PTemp Strain Stress Stroke TC1 Wedge

set TC1 to 0C
set tempmode to TC1.control
set h0 to 15.0000mm
set stroke to 0cm
set wedge to 0cm
zero stroke
zero wedge
set pump to on
set heat to on
delay 500msec
set mechanical to on
delay 500msec
set setuprun to on
set hypress to on
delay 15sec

// Zero out stroke under full load...
ramp stroke to -7cm in 5sec
delay 1sec
zero stroke
delay 100msec
set airtc to on
set airram to on
while force>-100kgf
    set wedgezero to wedgezero+0.0299999993294477mm
    delay 100msec
end

ramp stroke to 9.5772mm+1.5418mm+0.0000mm in 1sec  //
9.5772mm+1.5418mm+0.0000mm
ramp wedge to -0.75mm in 1sec   // -0.75mm

// energize load solenoid and grab specimen
set specload to on
delay 500msec
set specload to off

// Move into position for first deformation
ramp wedge to 2.4228mm-12.0000mm-0.0000mm in 1sec  // 2.4228mm-12.0000mm-
0.0000mm
zero Jaw
```

```
set thermal to on

// Pre-deformation:
set lastruntime to systime
sample at 100.0000Hz

ramp wedge to -8.7084mm in 1500.0000sec & // TX=0.8688mm
ramp TC1 to 6000.0000C in 1500.0000sec &
delay 250.0000sec
set airram to off
delay 1250.0000sec
set airram to off
delay 300.0000sec


zero Jaw
delay 0.1sec

// Deformations...
// Begin hit

// Hit 1:
// e:1.6000, e':10.0000/sec, dw: 1.0000msec, adj:0.0000mm/sec, com:
0.0000mm,
// tt:600C, tt':4.0000C/sec, soak:0.0000sec, exit:900C

// back up= bud + compliance + deltaH
ramp stroke to 1.5418mm+0.0000mm+9.5772mm in 12msec

delay 12msec   // 12

// finalH=2.4228mm (-) h0=12.0000mm (+) TX=0.8688mm (-) compliance=0.0000mm
{specH=2.4228mm, T=6000C}
ramp wedge to 2.4228mm-12.0000mm+0.8688mm-0.0000mm in 12msec  // 12

sample at 100.0000Hz

// Hit heating here
set airram to on   // specimen is cooling
// thermal compensation
ramp wedge to 2.4228mm-12.0000mm+0.0839mm-0.0000mm in 1350.0000sec &  //
TX=0.0839mm
ramp TC1 to 600C in 1350.0000sec

// Thermal soak
set airram to on
delay 0.0000sec

// final strain zero
zero Jaw
delay 0.1sec

delay 50.0000msec
set TC1 to 0C
sample at 10000.0Hz
delay 50.0000msec

ramp stroke to 9.5772mm in 0.0128sec


// True strain mode
```

```
ramp stroke to 8.6546mm in 8.0000msec &
ramp stroke to 7.8030mm in 8.0000msec &
ramp stroke to 7.0168mm in 8.0000msec &
ramp stroke to 6.2910mm in 8.0000msec &
ramp stroke to 5.6211mm in 8.0000msec &
ramp stroke to 5.0026mm in 8.0000msec &
ramp stroke to 4.4318mm in 8.0000msec &
ramp stroke to 3.9048mm in 8.0000msec &
ramp stroke to 3.4183mm in 8.0000msec &
ramp stroke to 2.9692mm in 8.0000msec &
ramp stroke to 2.5546mm in 8.0000msec &
ramp stroke to 2.1720mm in 8.0000msec &
ramp stroke to 1.8187mm in 8.0000msec &
ramp stroke to 1.4926mm in 8.0000msec &
ramp stroke to 1.1916mm in 8.0000msec &
ramp stroke to 0.9137mm in 8.0000msec &
ramp stroke to 0.6572mm in 8.0000msec &
ramp stroke to 0.4204mm in 8.0000msec &
ramp stroke to 0.2018mm in 8.0000msec &
ramp stroke to 0.0mm in 8.0000msec &
// End segment
ramp stroke to -0.1211mm in 5.0000msec  // 5

set TC1 to 900C
delay 1800sec
// End hit

// Post-deformation:
ramp stroke to 12.0000mm+3mm in 100msec  // 12.0000mm+3mm
ramp wedge to 2.4228mm-12.0000mm-2mm in 300msec  // 2.4228mm-12.0000mm-2mm
sample at 100.0000Hz

// Cooling...
set TC1 to 0C
set quench1 to on
set quench2 to on
delay 30.0000sec
set quench1 to off
set quench2 to off
// End cooling...
```